# Characterisation of Fresnel Interactions in a Novel Full-Stokes Spectropolarimeter Design

Master of Science Thesis

Andrei Dumitrescu

Delft University of Technology

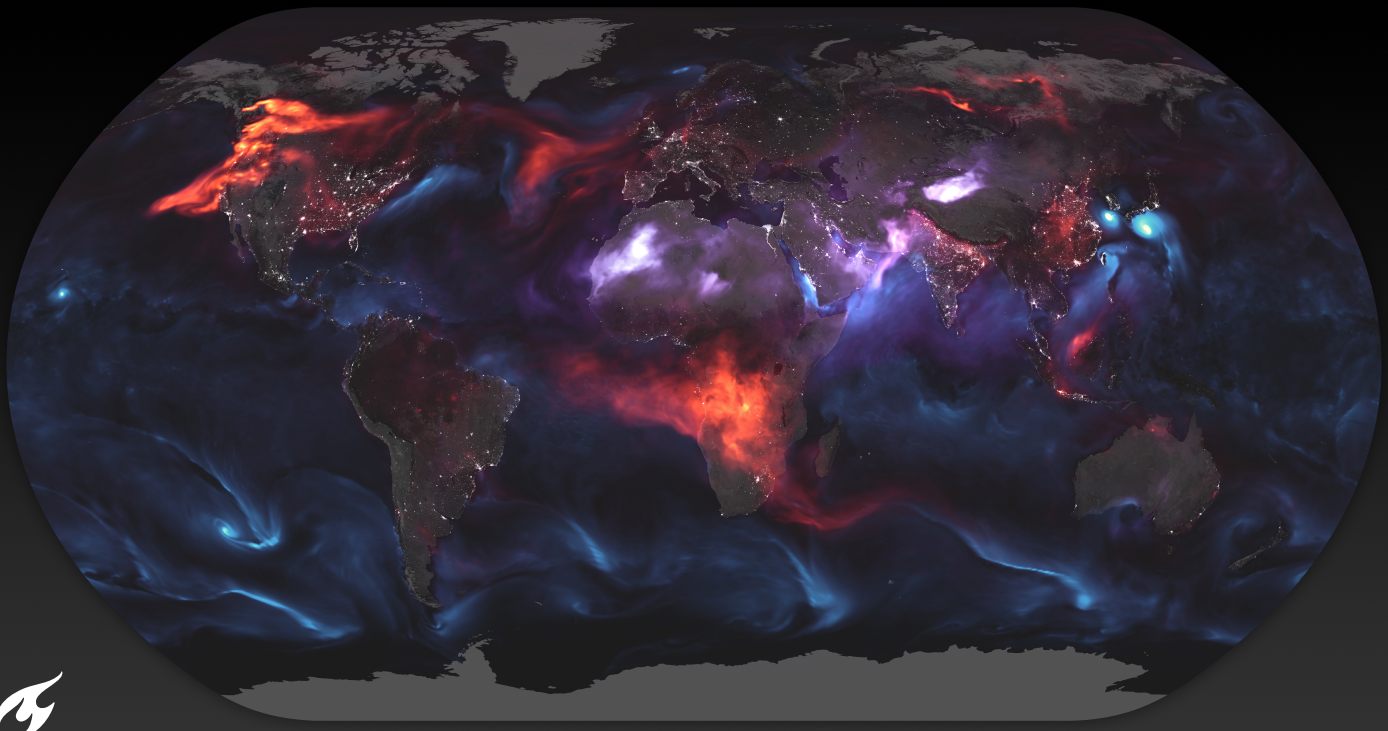

TU Delft

DELFT UNIVERSITY OF TECHNOLOGY
FACULTY OF AEROSPACE ENGINEERING

# Characterisation of Fresnel Interactions in a Novel Full-Stokes Spectropolarimeter Design

MASTER OF SCIENCE THESIS

Author: **Andrei Dumitrescu**
Student number: **4822684**

Thesis Supervisor:
**Dr. Pierre Piron**

Thursday 19th June, 2025

Cover : Just Another Day on Aerosol Earth by Joshua Stevens, NASA
https://visibleearth.nasa.gov/images/92654/just-another-day-on-aerosol-earth/92656w

TU Delft
Delft University of Technology

# Contents

# List of Figures

# List of Tables

# Abstract

Polarimetry in space is an increasingly prominent field in space research. Polarimetry, especially spectropolarimetry, have the potential to provide a substantial amount of information about the Earth as well as distant interstellar objects. In this field, full-Stokes spectropolarimetry is ideal for providing comprehensive polarimetric information. An instrument capable of making such measurements is often too large or complex for satellite use. A method which can theoretically perform full-Stokes spectropolarimetry while avoiding these drawbacks is currently being researched by Dr. Bogdan Vasilescu in collaboration with TU Delft. This new method makes use of a modulator formed out of 3 birefringent prisms, and a linear polariser, which together produces fluctuations in intensity. These fluctuations can be used to obtain information about any incident light.

The aim of this study was to investigate unexpected intensity fluctuations which occur even without the linear polariser, and determine the extent to which these can be explained by Fresnel behaviour at the boundaries of the prisms. To achieve this, Jones and Stokes models were produced in Python, simulations were performed in ZEMAX, and experimental measurements were taken to validate the results. For each of these methods, only the modulator first and third prisms were used as the second is designed as a structural component rather than an active element. From the models, simulations and experimental results, it was found that including Fresnel behaviour to models and simulations does result in output intensity fluctuations. Furthermore, it was determined that the periodicity of the fluctuations is very closely linked to Fresnel phenomena. The Python models and ZEMAX simulations especially returned results which appeared consistent, with easily explainable differences. On the other hand, further study is required to explain the differences in the amplitudes and average transmission of the intensity patterns between the different models, especially compared to the experimental results. The developed models and simulations can therefore demonstrate that Fresnel behaviour does explain the presence of the fluctuations but also suggests that the methods used in this thesis do not achieve a full representation of the phenomena, or that there are additional factors which must still be investigated.

# Acknowledgements

With the thesis now complete, I believe it is also important to take a moment to reflect also on all the people who have helped and have contributed to the project both directly and indirectly.

First of all, I would like to thank my supervisor, Dr. Pierre Piron, not only for providing me with the opportunity to do this thesis, but also for his consistent support throughout the project. I greatly appreciate the time he spent assisting me and guiding me in every step of the process. The time he dedicated to our meetings was extremely valuable to me and to the progress I achieved in this thesis. I would also like to thank Johannes Algera for supporting me as an additional supervisor, and for all of his assistance both during regular meetings, but also when I required additional advice. This thesis would not have been possible without either of them and their help.

I am thankful also to Dr. Bogdan Vasilescu, who designed the method and modulator on which the thesis is based, for lending me his knowledge and experience, and for taking the time to assist me during the experimental work performed for the thesis.

I would also like to offer my deepest gratitude to everyone from TNO, especially Ir. Eugenio Di Iorio and Ir. Rob Vink, who contributed significantly with the advice and information which they provided when the thesis project encountered difficulties. Their willingness to help, and their presence whenever their input was needed, were exceedingly beneficial to the report and project as a whole.

I am also grateful to Dr. Jérôme Loicq for making the thesis possible through both taking the role of Chairman and his contributions towards the earlier stages of the thesis. Thank you also to Dr. Jurgen Vanhamel, who has made time to join me at the final stages as a member of my thesis committee.

Finally, I want to offer my heartfelt appreciation to my family for their patience and dedication throughout the many years of study at TU Delft which have led to this moment. I would not have been able to achieve the successes or have risen above my difficulties without their unconditional love and support.

*Andrei Dumitrescu*
*Faculty of Aerospace Engineering*
*TU Delft*
*Delft, 2025*

# 1

# Introduction

When it comes to space exploration and the understanding of the Earth and the universe beyond, there are many tools which can be used for gaining knowledge. Of these many tools, one of particular note is spectropolarimetry. Spectropolarimetry is a study of the polarisation of light which has interacted with various media that are under investigation. Polarimeters are optical instruments that work by measuring the polarisation of light directly from a target, being scattered by a target or reflecting off a target [NASA, 2024]. This method can be used to get the angle of polarisation and degree of polarisation of the light to deduce details about the target itself based on knowledge of the light before and after the reflection occurred.

Polarimeters can be used to study the composition of the Earth's atmosphere and other distant space objects. One such application is the study of the atmospheres of Earth and other planets in order to gain an understanding of the processes taking place. Polarimetry can also complement other measurement techniques such as imagery and spectroscopic analyses of the sources of radiation in space. The combination of the different techniques can allow for a complete and in depth comprehension of the object of interest [Trippe, 2014]. Combined with these other methods, it can be used to reveal the magnetic fields, internal conditions, particle densities, and more of astronomical objects [Trippe, 2014].

Polarimetric measurement of space phenomena was first started in the nineteenth century using ground based instrumentation [Clarke, 2009]. This makes maintaining and improving the equipment simple, but at the cost of being limited by the atmosphere for certain applications [Iglesias et al., 2016] and the inability to move the polarimeter to the necessary location or celestial body as needed. Because of this, polarimeters have since evolved into being used on satellites as well [Dubovik et al., 2019]. This, in turn, poses new problems. As the instrument and its components are now not accessible, maintenance is impossible. This results in reliability becoming a critical limitation on the complexity of the instrument and the applications for which it can be used. Moving parts also affect the achievable sensitivities of the instrument [Sparks et al., 2012] as they introduce sources of noise and can affect the stability of the instrument resulting in loss of precision.

Additionally, the more advanced instruments are often bulky[1], making them less suitable for space use [Vasilescu et al., 2023].

A large part of this is due to the need for multiple moving parts and many optical elements such as mirrors, half-waveplates and linear polarisers, needed to be able to study the entire polarisation state of the light [Sparks et al., 2012][Vasilescu et al., 2020b]. New methods must therefore be found to mitigate or remove these issues in order to allow for smaller and better suited designs for space missions. The need for a more compact instrument is further reinforced by the increasing number of CubeSat designs which cannot hold any of the larger payloads but can provide cheaper and easier access to space.

## 1.1. Problem Statement

The current Master thesis project will be on furthering research and development on a new spectropolarimetry method, created to allow for full Stokes snapshot polarimetry while also having fewer components and no moving parts. This new method is primarily focussed on a new design of modulator. This modulator is comprised of 3 birefringent prisms which modulate the light across the vertical axis of the modulator [Vasilescu

[1] URL: https://www.sciencedirect.com/science/article/pii/S0030401820301954, last accessed 14-06-2025

et al., 2020b]. When combined with a static linear polariser, this modulator design can turn any incident light into an intensity pattern that can be used to obtain the original incident polarisation state [Vasilescu et al., 2020b]. Normally, polarimeters which perform the same function require either many additional components or moving parts to be able to create the same effect, however, in the case of the new design none of the components need active movement and can therefore be left untouched. Thus, once the setup is validated, the modulator design alleviates the primary problems with current polarimeter designs for space use. With only the modulator and a single linear polariser being required, this method is both compact and reliable with no moving parts.

During testing efforts conducted by the research team working on the modulator, experimental results did not coincide with the theoretical outputs of the modulator. It was observed that intensity fluctuations would occur even without the presence of the linear polariser after the modulator. Based on the existing mathematical models of the modulator, such behaviour should not occur. The contribution of this thesis will be to investigate whether the differences between models and experimental data are caused by internal Fresnel transmission and reflection behaviour.

## 1.2. Research Questions and Objectives

Based on the findings of the research group prior to the beginning of the thesis, it was hypothesised that the cause of the unexpected fluctuations may be at least partly due to Fresnel phenomena at the prism boundaries. In order to investigate this claim, this thesis was conducted with the goal of answering the following research question:

***To what extent can the fluctuations in intensity caused by the modulator be explained through Fresnel transmission and reflection behaviour?***

The research objective which follows from this research question is:

***To explain the fluctuations observed in the preliminary experiments by modelling the instrument with Fresnel reflections in Python models and ZEMAX simulations which will be validated experimentally.***

To answer the research question as well as accomplish the research objectives, a set of sub-questions are proposed starting with fundamental questions and building up to more specific questions related to the thesis process.

1. **"How can the setup and the Fresnel behaviour be combined to model the modulator in Python?"**
2. **"How can the modulator be simulated effectively in ZEMAX"**
3. **"Is the addition of Fresnel behaviour to the models and simulations sufficient to represent the fluctuations observed experimentally?"**
4. **"Can the experimental results be recreated in another experiment?"**
5. **"Do new experimental measurements portray the same fluctuations?"**
6. **"Can new experimental measurements be used to validate the models and simulations?"**

Given these main sub-questions, it is possible to define the sub-goals which provide the overarching progression of the thesis and help answer each of the sub-questions.

The first sub-goal was to gather knowledge on all of the fundamental concepts tied into the function of the modulator. This sub-goal was achieved in an extensive literature study in which polarisation as a concept was investigated. What it is and its applications in science were researched to place the thesis into the larger context of space-borne polarisation.

During this literature study, another goal was to study how polarisation is measured and how it can be represented. The mathematical formalisms, primarily 'Jones' and 'Mueller-Stokes' formalisms, were studied in detail. Additionally, optical components and birefringent materials were researched to understand how they work and how they can be represented mathematically. As the modulator prisms are birefringent, understanding this concept is crucial to being able to model the prisms in Python or ZEMAX.

In addition to this, Fresnel phenomena and how they affect the polarisation state and intensity of light were looked into, along with how it can be integrated into the mathematical representations. Gaining insight into the formulas describing Fresnel phenomena was critical in being able to later apply Fresnel to the 'Jones' and 'Mueller-Stokes' formalisms when attempting to model the modulator behaviour. It was especially important to research the current 'state of the art' in relation to Fresnel behaviour implementation for birefringent prisms, as the literature study revealed a 'gap' in the general scientific knowledge. This was most prominent with regards to a more complex birefringent interaction such as in the case of the modulator used in the thesis. This

sub-goal was necessary to allow for the acquisition of different Fresnel - birefringent boundary interaction mathematical representations which could then carefully be adapted to the purpose of modelling the modulator.

After the literature study, the next sub-goal was to build the foundation of how the modulator can be modelled in Python. At this stage the mathematical formalisms discovered in the literature study where applied in modelling the basic modulator elements without considerations of Fresnel. It was imperative, for this sub-goal, to model different optical components and build up to a model of the entire modulator. This sub-goal would serve not only to create a model of the modulator which matched with the current theoretical function of the modulator, but also to have enough understanding of how the components work together so that further modifications can be performed with confidence. Two different versions of this model would be created, each following a different polarisation mathematical formalism. These can be compared to give clear indications as to whether the base model functions as intended prior to Fresnel phenomena being included.

Because the literature study revealed that the modulator uses birefringent materials in a seemingly unconventional way, the next sub-goal was to adapt the knowledge and methods which were compiled, into the Python model. As there are no previous model results to compare to which also include Fresnel phenomena, the two different formalisms will both be used to perform rudimentary verification prior to the ZEMAX or experimental methods being attempted. This would serve to give an indication as to whether the investigation into the Fresnel phenomena and the intensity fluctuations is progressing on the right track.

Once the Python model is completed, the subsequent sub-goal was to develop the ZEMAX simulation. Studying how to use the software and how to process the data are both crucial elements of this sub-goal. Deciding how to create the simulation using the inbuilt settings and simulation types would have a significant impact on the outcome of this step. The decision between 'sequential' and 'non-sequential' simulation modes and how the prisms can be created in the simulation environment both presented important stages in the completion of this sub-goal. The results of the ZEMAX simulations were then intended to be used to verify the Python model results.

Following the Python and ZEMAX models, and the verification of their results through comparison, the next sub-goal was to decide how to perform another experiment which could be used to validate the results. For this sub-goal, the laboratory setup and components were studied, and the experiment was planned and performed to acquire data on the fluctuations caused by the modulator. This data was to be analysed and then compared to both the Python model and the ZEMAX simulations to observe the extent to which the models are able to represent the experimentally observed intensity variations.

## 1.3. Outline of the Report

The purpose of this report is to document and compile the findings of the thesis project. To achieve this, the report will be structured as follows. First, the background information regarding polarimetry and Fresnel phenomena is provided in chapter 2. After this, the specific polarimetry modulator that is being studied in the thesis is discussed in more detail in chapter 3. Once the background and context have been established, the mathematical forms and representations used in this thesis are presented in chapter 4. The Python models created, using the mathematical forms, are shown in chapter 5 along with their results, followed by the ZEMAX simulation equivalents in chapter 6. The experimental testing used to compare and validate the models and simulations is presented in chapter 7. The chapter following this, chapter 8, shows the final comparisons between the 3 methods performed during the thesis research, and recommendations on how the research could be continued or improved. Finally, conclusions are given in chapter 9.

# 2

# Background

The purpose of this chapter is to provide the background to the thesis. To do this, first and foremost it must be made clear why polarimetry is an interesting subject in the domain of space research. To clarify why polarimetry is so extensively researched, first the many applications of polarimetry are presented in section 2.1. After this, a general introduction to polarisation is provided in section 2.2, followed by an overview of how polarisation can be measured in section 2.3. With polarisation and polarimetry both explained, some examples of previous missions are also provided in section 2.4.

## 2.1. Why is Polarimetry relevant to Space Research?

Polarimetry, being the measurement and analysis of the polarisation of light, has already had many applications found in the domain of astrodynamics. Often, the instruments are ground based polarimeters which look upwards into space to infer information about celestial objects. Understanding the reasons why polarimetry is extensively researched for space research, and specifically why there is now a greater interest in putting polarimeters on satellites, is a key first step in understanding why the research into the new modulator design is both necessary and interesting.

To begin with, why is the polarisation state of light important in space missions? According to Hough [2006], having knowledge of the polarisation state of radiation is far more useful than having only the intensity, as you obtain far more astrophysical information.

The origin of polarised light in the space environment can be due to a number of different processes caused by the surfaces, materials and media which the light has passed through or interacted with. Among the common causes of polarisation are absorption, refraction, reflection and scattering[1].

As the medium which the light has interacted with defines how the light changes as it passes through or bounces off, the polarisation state of the light is directly correlated to the medium itself. This means that by measuring the polarisation state of the light after the interaction has taken place, valuable information can be obtained relating to what the medium was. One of the most prominent media which the light inherently interacts with, is the Earth atmosphere. The Earth atmosphere induces scattering of the light, which in turn changes the polarisation state. This interaction between the atmosphere and the light means that polarimetry can be used to study the atmosphere and its composition. However, it also makes it difficult to obtain the astrophysical information of celestial objects of interest from Earth-based measurements. An evident solution to this issue is to move the polarimeter into space. The application of polarimetry in space on board a satellite also opens up the possibility to take measurements of the Earth itself.

In terms of the benefits of polarimetry compared to a pure intensity measurement, polarimetry can be used to, for example, study the nature of planetary surfaces and atmospheres [Hough, 2006]. Another possible study direction which has been explored in the past using polarimetry is the study of interstellar dust [2]. As this dust induces a polarisation state on light passing through it, this can be measured and researched by polarimetry. Hough [2006] also references the use of polarimetry to map the direction of magnetic fields of objects in space,

[1] URL: `https://www.microscopyu.com/techniques/polarized-light/introduction-to-polarized-light`, last accessed 14-06-2025

[2] URL: `https://www.eso.org/public/teles-instr/technology/polarimetry/`, last accessed 14-06-2025

including dusty molecular clouds where stars are forming. Because the magnetic field is believed to play an important role in the formation of stars in this example, being able to map them with polarimetry is extremely useful. Polarimetry can also be adapted to specific spatial objects by choosing which wavelengths to measure. Different wavelength bands allow the measurement to be performed for many interstellar objects as needed based on their characteristics.

Moving on from magnetic fields and interstellar dust, the polarisation effect produced by material around a star can also be measured. The light coming from the star is scattered by any material in either a protoplanetary disk, debris disk and other possible clouds of dust circling the star. From the polarisation state recorded, the inclination of the disk, the current size of the disk, and the formation of new planets can all be studied using polarimetry [Hough, 2006]. Even without the presence of a disk of material, it is possible to use polarisation measurements to observe planets around distant stars [3]. In theory, the polarisation of light reflecting off the atmospheres of other planets would also provide information about the atmosphere and planet too, although Hough [2006] states that such measurements have not yet been done successfully.

In some observations, circular polarisation of light has been linked to the observation of biomarkers [Hough, 2006]. The analysis of biomarkers can be used to possibly find life or signs of life on other planets. Furthermore, polarimetry in Earth observation can be useful in tracking aerosols to improve the characterisation of which aerosols are in the atmosphere [Hough, 2006]. Understanding the composition of the atmosphere can help in explaining climate change, as well as finding solutions to counteract it. From Dubovik et al. [2019] it can be seen that space-borne polarimetry is critical for this purpose, hence the need for space polarisation equipment.

Given the many uses of polarimetry which are discussed above, the benefits of advancing current space polarimetry technology are evident. This is why this thesis focusses on a new method of achieving versatile, reliable, and efficient spectropolarimetry, which has the potential to facilitate future advancements in this field.

## 2.2. What is Polarisation

In section 2.1, the general reasons as to why space polarimetry is a subject of interest have already been provided. The following step to understanding the thesis background is properly defining polarisation itself. While mentions have already been made as to what it can be used for, the concept has not yet been defined concretely within this paper. This will be done in this section.

Polarisation is a property of light which is directly linked to the internal geometry of a source. Polarisation stems from the equations denoting electromagnetic waves in a vacuum. To start with, it is possible to define the electric field **E** of an electromagnetic wave travelling in the 'z' direction at speed of light 'c' as a vector with components in x and in y axis directions.

The electric field is represented as a vector with components in both the x and y directions; $\mathbf{E} = \begin{pmatrix} E_x \\ E_y \end{pmatrix}$

The general formula for each component at a specified location along the 'z' axis at a certain time 't' is given by

$$E_x(z,t) = E_x(0,0)\cos(\omega t - kz - \phi_1) \tag{2.1}$$

$$E_y(z,t) = E_y(0,0)\cos(\omega t - kz - \phi_2) \tag{2.2}$$

where $\omega$ is the angular frequency, t is the time, $k = \omega/c$ ( or, alternatively, $k = 2\pi/\lambda$ with $\lambda$ being the wavelength) is the absolute value of the wave vector and $\phi_{1,2}$ represent the phase of the wave on that specific axis [Trippe, 2014]. From here, to obtain a clear polarisation state of the light at a specific point, these formulas can be specified for a given location 'z'. The $E(0,0)$ terms in Equation 2.1 and Equation 2.2 simply represent the electric field value at the origin where the distance travelled in the 'z' direction is 0, and the time is also 0. The components of the wave in the x-y plane after the z-location is no longer arbitrary are shown in Equation 2.3 and Equation 2.4 with z = 0 chosen for simplicity [Trippe, 2014].

$$E_x(t) = E_x(0)\cos(\omega t - \phi_1) \tag{2.3}$$

$$E_y(t) = E_y(0)\cos(\omega t - \phi_2) \tag{2.4}$$

[3] See footnote 2.

The polarisation state of the electromagnetic wave is dictated by the relative values of $E_x(0)$, $E_y(0)$, $\phi_1$ and $\phi_2$ [Trippe, 2014].

Polarisation in its general form is elliptical, with all polarisation states able to be described by the parameters of the 'ellipse' which the tip of the electric field vector follows. By defining a value '$\psi$' as the angle between the ellipse semi-major axis and the x-axis, and a ratio between semi-major and minor axes, it is possible to fully describe any polarisation ellipse. In the figure below, Figure 2.1, an arbitrary example is given with $\psi = 30°$ and an overall light intensity of 1.

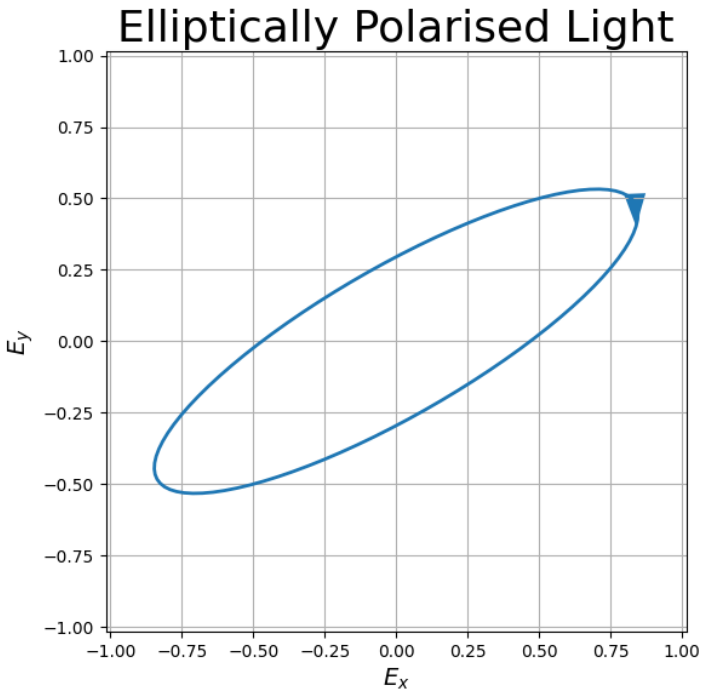


**Figure 2.1:** Elliptically polarised light example, with $\psi = 30°$ and an intensity of 1.

The special cases of polarisation which often come up in polarisation research are linear polarisation and circular polarisation. These cases occur when the ellipse degenerates into a line or a circle, respectively.

Linear polarisation is the special case when $\Delta\phi = n\pi$, with $n = 0, 1, 2....$ In this case, the orientation of the electric field is given by the magnitudes of $E_x(0)$ and $E_y(0)$ along with the angle $\psi$ which is equivalent to $\arctan(E_y/E_x$ in this case. Circular polarisation is the special case when $\Delta\phi = \pm n(\pi/2)$, with $n = 1, 2, 3....$ In this case, the tip of the electric field vector moves circularly in the xy plane with angular frequency $\omega$ [Trippe, 2014]. The direction of rotation is given by the sign. In this project the convention with which the thesis was started follows the 'thumb rule' where the thumb is pointed in the direction of propagation, and the direction is defined as right-hand polarised if the rotation follows the direction of the fingers on the right-hand. Similarly, if the rotation follows the left hand, it is 'left-hand polarised'. This is counter to the convention given by Trippe [2014], and therefore extra care must be taken when working with circular polarisation.

It is also possible for the light to be in one of 2 alternative polarisation states. The first of these is when it is entirely unpolarised. Unpolarised light refers to light with a random polarisation state which varies in time. What this essentially means is that at any time $t$ when the light polarisation state is observed, it will be different to the polarisation state of the same light at a time $t + \delta t$ as the polarisation state itself varies from one moment to the next. In the case of unpolarised light, $\delta t$ is too small for a detector to measure the polarisation state of light before it changes once again [Shevchenko et al., 2017]. This makes it extremely difficult to measure any specific polarisation state of the light with current technology.

When the light is not able to be solely described by elliptical polarisation in its entirety and is also not completely unpolarised, it is referred to as partially polarised. In this case there is a combination of unpolarised and fully polarised light within the same light ray. As the ellipse can only represent fully polarised light, an additional variable referred to as the 'degree' of polarisation is needed to describe cases in which this occurs.

## 2.3. Polarisation Measurement

Having now discussed the fundamentals of what polarisation is in section 2.2, it is also worth discussing how the polarisation state of light can be measured and how the polarisation state of light changes when exposed to different optical materials or components.

### 2.3.1. Polarisation Material Interactions

To explain how the polarisation tools work and why different prism designs are considered, Partial reflection and birefringence must be introduced.

**Fresnel Phenomena**

Partial reflection is the effect which occurs when the wave hits a boundary between two media with different refractive indices. Partial reflection at the boundary of a medium is often referred to as 'Fresnel reflection'. As the term 'Fresnel reflection' neglects the fact that there is also a transmitted element of the light, this thesis will instead refer to it as Fresnel phenomena or Fresnel behaviour. This behaviour is one of the main areas of study in this thesis and must therefore be explained in order to provide context as to why this phenomenon is important to account for in polarimetry. When the electromagnetic wave passes through from a material with a refractive index $n_1$, into a material with a refractive index $n_2$, the light wave ends up being partially refracted and partially reflected [Chaumette, 2021] as shown in the simplified visual aid in Figure 2.2. The relation between the refracted wave and the reflected wave is based on the plane of incidence along with the angle of incidence and the materials. It also depends on the polarisation state of the light and the wavelength. These factors result in the light being altered as it passes through boundaries between media. Hence, when the medium which the light passes through changes, the properties of the light also do.

The effect which such a boundary has on the polarisation state of the light is the same on any incident polarisation. As such the changes which occur can be predicted. By altering the angle of incidence and the ratios between the refractive indices of the materials, it is possible to manipulate the polarisation state of light of both the reflected and transmitted beams [Newport, 2024] to produce a desired effect. One situation where the Fresnel phenomena on a boundary can change based on the polarisation state of the incident light is when use is made of birefringent materials. These will be discussed next.

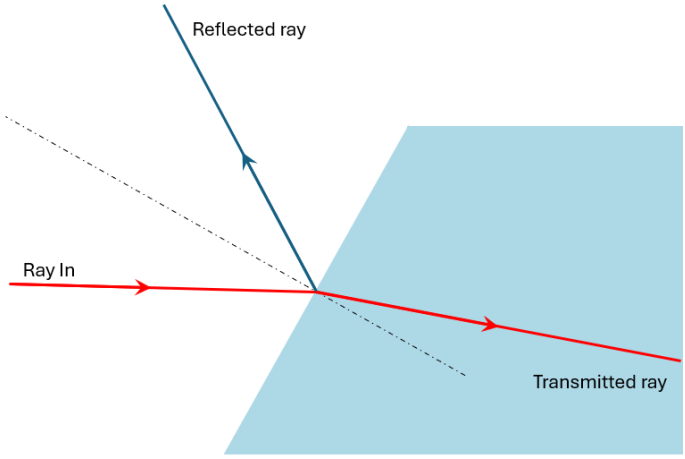


**Figure 2.2:** Simple diagram demonstrating Fresnel transmission and reflection behaviour. The incident ray can be seen both transmitting and reflecting off a boundary between to media.

**Birefringence**

Birefringence is an effect that occurs when the medium through which the wave is passing has different refractive indices based on the direction of the electric field. This is caused by the difference in permittivities in each axis direction.

With the permittivities indicated as $\{\epsilon_x, \epsilon_y, \epsilon_z\}$, 3 main cases can be observed in materials. The first is for isotropic crystals. These are cases where all permittivities are equal. In uniaxial crystals, on the other hand, $\epsilon_x = \epsilon_y \neq \epsilon_z$. For biaxial crystals, none of the permittivities are equal.

As the permittivity in 2 or more axes is different in uniaxial and biaxial crystals, the linear polarisation components of the incoming light experience different refractive indices. This allows for the manipulation of the phase velocity difference between each linear component and makes it possible to alter the orientation and the form of polarisation similarly to half or quarter-waveplates. This technique is used in the crystals and prisms referenced for linear polarisers in order to allow for the linear polarisation components of unpolarised or partially polarised light to be separated and measured individually.

For uniaxial birefringent materials, which are similar to the modulator material for the thesis project, the definition of each refractive index is determined by the 'fast' axis and 'slow' axis. The fast-axis represents the axis of the material along which the light experiences the least slowing down. The slow-axis, as implied by the uniaxial crystal, is perpendicular to the fast-axis and is the axis where the light is most slowed down. The orientation of the fast-axis dictates the effect which a birefringent material will have on the incident light.

If a light ray is considered which is entering into a birefringent material, and we consider the birefringent material to have a fast-axis in the x direction, and slow-axis in the y direction, the effect on the ray of light is essentially that it interacts with a different 'material' based on whether you look at the x or the y components. Because of this interaction, the single incident ray separates into two rays which each have a different angle of refraction corresponding to the refractive index experienced. The two rays which result from this interaction are known as the 'ordinary' and 'extraordinary' rays [4]. Similarly, the refractive indices corresponding to each ray will be referred to as $n_o$ for the 'ordinary' refractive index which will be the fast-axis refractive index, and $n_e$ for the 'extraordinary' refractive index which will be the refractive index of the slow-axis.

At normal incidence, still assuming a fast-axis along x and slow-axis along y, the light still interacts with both $n_o$ and $n_e$, however now the rays both follow the same path. Despite the rays not refracting due to the normal incidence at the boundary, the x and the y components of the light electric field still interact with different refractive indices. The resulting effect on the light is that the component along the slow-axis will propagate slower than the component along the fast-axis. This induces a change in the relative phase between the two components. Based on the difference in the refractive indices and the distance the time which the light spends within the birefringent medium, the relative phase at the exit boundary can be changed.

In Figure 2.3 a simple representation of how the phase changes after the light passes through a birefringent material at normal incidence is shown. In this specific example the phase shift is arbitrary and the diagram only serves to demonstrate the effect of birefringence on the electric field components of the incident light. There are also special cases which specifically produce a $\pi$ or $\pi/2$ phase difference. These cases will be discussed more in subsection 2.3.2.

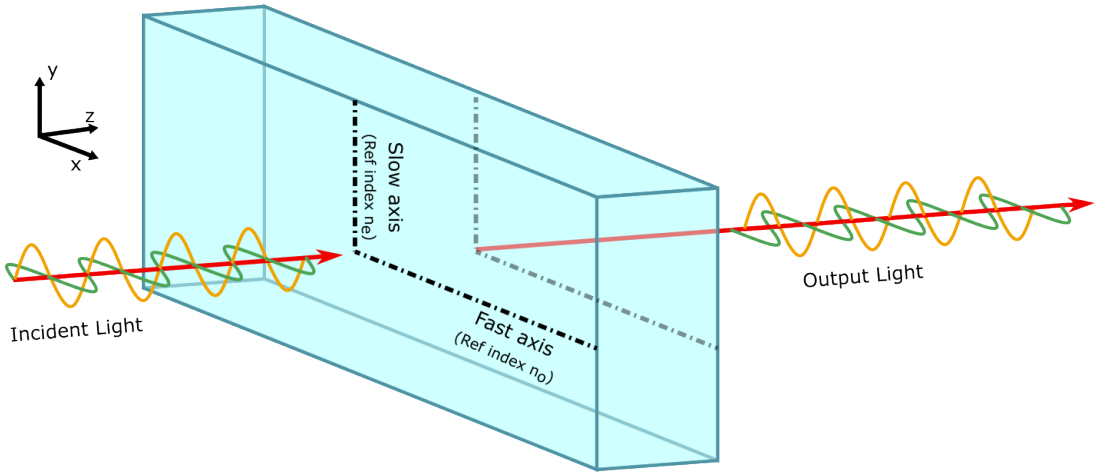


**Figure 2.3:** In this simplified diagram, an arbitrary case is shown where the electric field components in x (green) and y (yellow) interact with a birefringent material at normal incidence. While the components are both in phase on entry into the material, this is no longer the case at the output. The cause of this effect is the difference in refractive index which each component interacts with.

Combining Fresnel phenomena with birefringence gives a great level of control over how the light polarisation changes at boundaries between media. At a birefringent boundary, beams become linearly polarised in

[4] URL: https://www.microscopyu.com/techniques/polarized-light/principles-of-birefringence, last accessed 14-06-2025

orthogonal polarisation directions to each other. However, if the incident light is circularly polarised, the light remains circular. Changing the angle of incidence and the material properties can be used to produce specific effects and output specific polarisation states.

Due to the nature of birefringent materials, the Fresnel behaviour occurs differently when the incident light changes polarisation state. This is due to the polarisation state of the light aligning with a different 'refractive index' and experiencing different material properties. As the Fresnel phenomena are influenced by the refractive index, this also means that how much of the ray transmits or reflects is equally affected by the correlation between the incident polarisation orientation, and the birefringent fast-axis.

### 2.3.2. Polarisation Components and Tools

When it comes to manipulating the polarisation state of incoming light, there are various options depending on the intended purpose. Some of the components which can be used are linear polarisers, half-waveplates and quarter-waveplates.

Linear polarisers are polarising components which transform any input light into a linearly polarised output by blocking all light along the undesired polarisation component/direction. Because of this, only the component which is desired is passed through, resulting in a linear polarisation state of the output. Combining multiple linear polarisers in a row at different angles can further change the linear polarisation orientation as long as there is a component of the light which can pass along the new direction. It is also possible to linearly polarise light using crystals or prisms which can separate the light into its linear polarisation components using partial reflection. The most common types of polarisers are polarising beam splitters, Nicol prisms, and Glan-Thompson prisms [Trippe, 2014] as well as wire grid film polarisers.

Half-waveplates are often used for the purpose of rotating the orientation of linear polarisation of light. The input linear polarisation orientation is changed to a new output orientation without losses which occur when accomplishing this with multiple linear polarisers. It is also possible to use half-waveplates to change left hand circular polarisation to exactly right hand circular polarisation and the inverse as well. This is done by using birefringence which induces a phase shift of $\pi$ between the fast and the slow axes. When the light is elliptically polarised, the half-waveplate can be used to reorient the polarisation ellipse without affecting the ratio between the major and minor axes.

Quarter-waveplates also use birefringence in order to manipulate incoming polarised light. By inducing a phase difference of $\frac{\pi}{2}$ between the fast and slow axes, a quarter-waveplate can be used to transform the polarisation state. The reason why quarter-waveplates are particularly noteworthy is that they are capable of turning linear polarisation into circular polarised light and circular polarised light into linear without losses in intensity. For a linear to circular transformation, the effect is achieved if the incident polarised light is linear and oriented at 45° compared to the fast-axis. In Figure 2.4 a diagram is used to show how the phase shift caused by a quarter waveplate results in a circular polarisation state from a 45° incident linear polarisation.

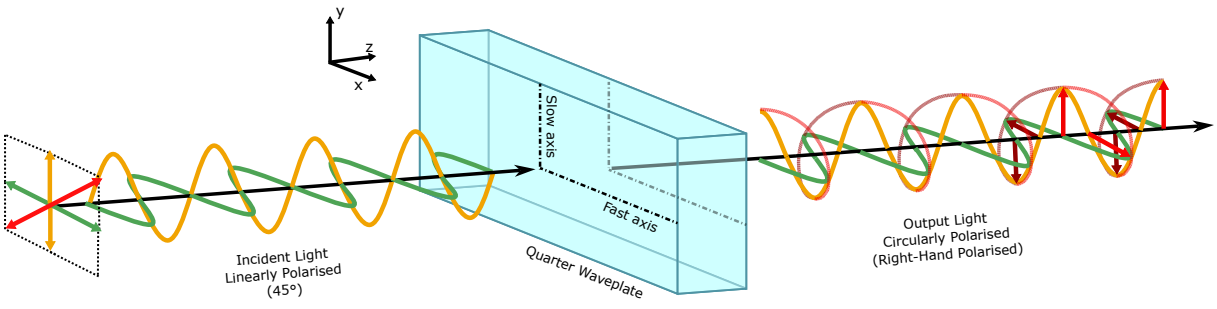


**Figure 2.4:** In this simplified diagram, the effect of a quarter waveplate is shown on an incident beam at 45° linear polarisation. Due to the quarter waveplate causing a $\pi/2$ phase shift to occur, and given the orientation of the fast-axis, the output light state is right hand circularly polarised.

It is also valuable to briefly understand the use and purpose of a modulator in a polarimeter. In general, polarisation measuring instruments follow the same key base designs. There are a few principal ways in which a polarimeter can be created. One such method is using a modulator and an analyser. Another would be to use beam splitters in order to measure the different polarisation directions simultaneously by separating the light into all of its individual polarisation components. It is also possible to use rotating birefringent elements

or linear polarisers in order to measure individual components of the polarisation state as the element rotates and changes the light which passes through.

The primary design which relates to the thesis is that of a modulator followed by an analyser. The modulator and analyser transform each polarisation component into intensities which can be used to obtain the overall polarisation state of the light [Hough, 2006].

With the right design of the modulator and analyser, it is possible to measure the different polarisation components as needed. As not every mission requires every polarisation component to be observed, there are many possible designs which can accomplish just the required measurements. These designs also are based on the intended wavelengths to be measured, whether there is a need for multi-angle polarimetry, limitations in space onboard the satellites and which viewing angles are required.

## 2.4. Previous Missions

Up until this point, the basic elements of polarisation and polarimetry have been introduced. The reasons why polarimetry is a topic of interest to space research have been discussed and the general polarisation definitions along with tools have been presented. In order to link the interest in polarimetry with how the tools can be used to measure polarisation, some of the already existing space polarimetry missions will be looked at.

Dubovik et al. [2019] has compiled a list of many of the missions which were planned or had been already completed in around 2019. Not all of these will be discussed in this section, but some of them will be given as examples and talked about. The majority of these missions are designed for Aerosol measurements and are Earth observation satellite instruments.

The first missions to be discussed are the POLDER missions 1 to 3. These were launched in 1996, 2002 and 2004 respectively, with POLDER 3 finally ending its mission in 2013. POLDER stood for Polarisation and Directionality of the Earth's Reflectance. These instruments, shown in Figure 2.5, used a rotating filter wheel to enable measurements in 9 spectral channels between 20 and 40 mm bandwidths [Dubovik et al., 2019]. The rotating filter wheel was designed to select both the spectral bands and polarisation state, allowing the polarisation of the light to be determined through the use of 3 successive measurements performed at 3 positions of the wheel [Deuzé et al., 1993]. A polariser is fixed to each filter, and the angle between the 3 polarisers is set to 60° [Deuzé et al., 1993]. The measurements can be combined and compared to obtain the total and polarised reflectances. The POLDER missions, having spanned 10 years, represent the longest lasting multi-angle polarimetric observations [Dubovik et al., 2019].

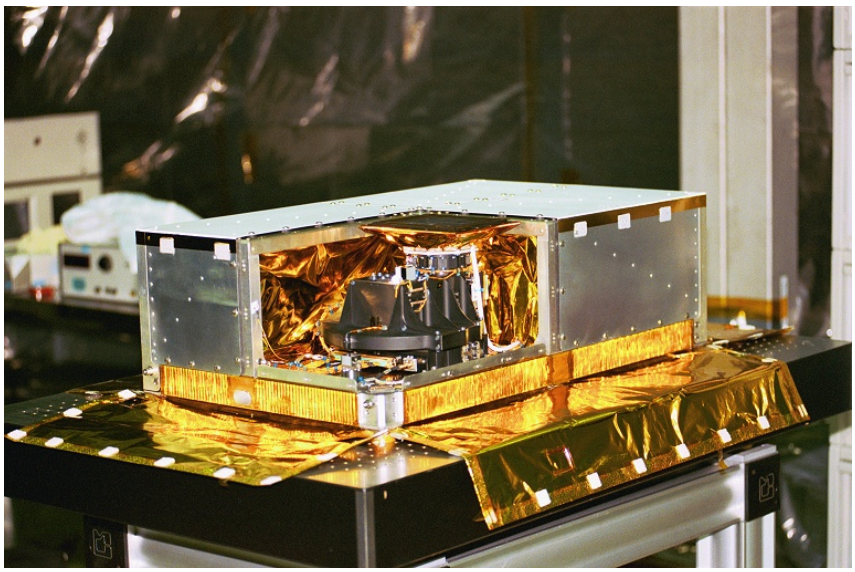

**Figure 2.5:** The POLDER instrument[5].

Next are the GOME missions, GOME 1 and GOME 2. The Global Ozone Monitoring Experiment (GOME) missions were on the ERS-2 and MetOp-A/B/C missions. These were launched in 1995, 2006, 2012 and 2018.

[5]URL:`https://regards.cnes.fr/polder/html/Polder/polder_SH.html`, last accessed 15-06-2025

These instruments were designed to measure trace gases, primarily Ozone through spectrometry [Dubovik et al., 2019]. The GOME-2 scanning spectrometer can be seen in Figure 2.6. Although the GOME missions were not primarily polarimeters, polarisation of the light scattering off aerosols and other atmospheric particles affected the measurements. In order to measure the polarisation state of light to correct the effect, broad-band polarisation sensors were carried to measure the linear polarisation components of the light along the 45° and -45° axes. For GOME-2 the linear polarisation of Earth's radiance was directly measured in both perpendicular directions using linear diode arrays which are referred to as Polarisation Measurement Devices (PMD's) containing the same type of diode arrays as the primary instrument spectrometer [Munro et al., 2006]. These measure the intensity and relative electric field of the light along the horizontal and vertical axes. The method by which this is performed is not described in detail across any of the sources found, but, as the polarisation state of the light is something to be corrected for, it is suggested that the PMD channels are used to correct the main channels through direct comparison [Krijger et al., 2005]. This comparison also appears to, in turn, obtain the polarisation state itself if desired [Krijger et al., 2005]. Circular polarisation was not included as it is negligible when it comes to Earth observation [Krijger et al., 2005].

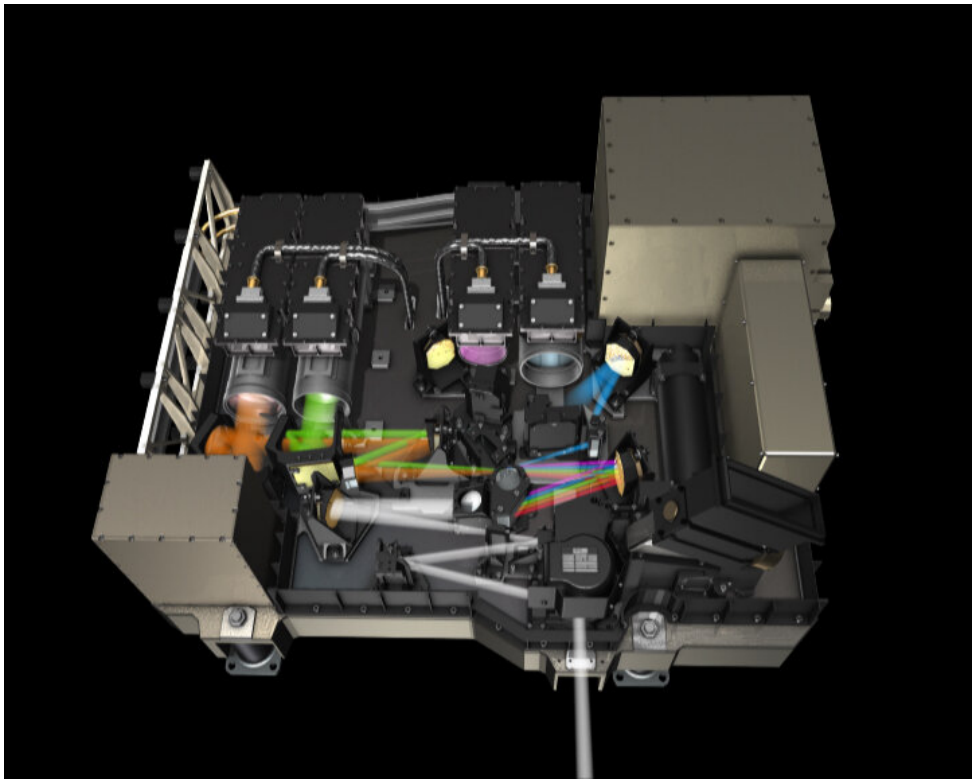

**Figure 2.6:** The GOME-2 spectrometer[6].

Another mission, the Second Generation Global Imager (SGLI) flew on the Global Change Observation Mission-Climate satellite (GCOM-C) in 2017. The overall instrument is designed to measure the Earth's reflectance. The imager is composed of different sensors. One is the push-broom VNIR (Visible and Near-Infrared) radiometer, shown in Figure 2.7, and the others are whisk-broom infrared infrared scanners. Polarisation optical equipment is included in the VNIR [Dubovik et al., 2019] and can measure the intensity, and can determine the precise polarisation state of light except for circular polarisation. The technology used is based on the POLDER instrument, however, unlike POLDER, the SGLI VNIR polarisation equipment, according to Dubovik et al. [2019], is not designed for multi-angle measurements and can only do polarisation measurements for a single viewing angle.

[6]URL:https://www.esa.int/Applications/Observing_the_Earth/Meteorological_missions/MetOp/About_GOME-2, last accessed 15-06-2025

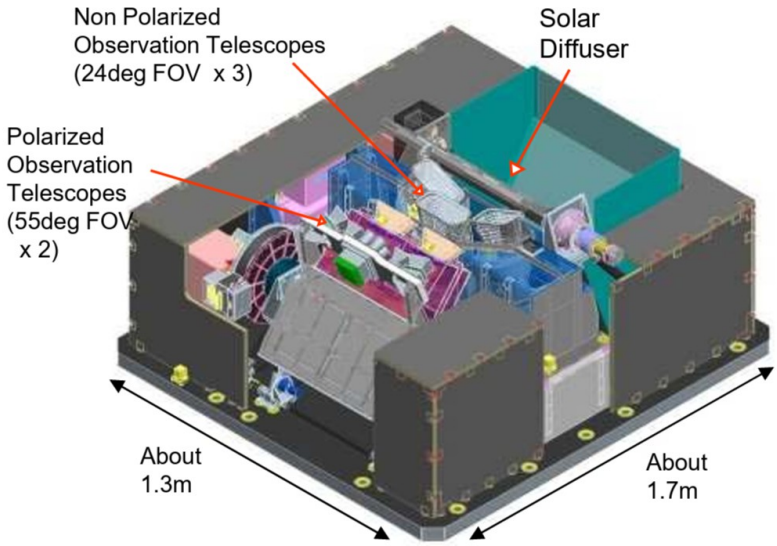


**Figure 2.7:** The VNIR radiometer from the SGLI mission[7].

The HARP (Hyper-Angular Rainbow Polarimeter) instruments are another set of polarimeters which can be briefly discussed. These Hyper-Angular Rainbow Polarimeters focus on hyper-angular polarimetric measurements in UV, VNIR and SWIR spectral ranges. The instruments can see the Earth from multiple viewing angles at the same time at 4 wavelengths and 3 polarisation angles. The HARP polarimeter does not have any moving parts and is based on a Philips prism design for simultaneous measurements of linear polarisation at 3 orientation angles [Dubovik et al., 2019]. The instrument is also fully programmable to allow spatial resolutions, wavelengths and viewing angles to be chosen as needed. This also allows multiple views of the same target to gain additional information and ease in "the quantitative retrieval of atmospheric and surface properties such as the aerosol particle amount, aerosol particle size, shape, and complex refractive index, as well as cloud droplet sizes, and specific characteristics of the Earth's surface" [UMBC, 2020].The first HARP-CubeSat was launched in 2019 [Dubovik et al., 2019]. HARP2, shown in Figure 2.8, planned for the NASA PACE mission which launched recently in 2024 is an improved version of the previous instrument.

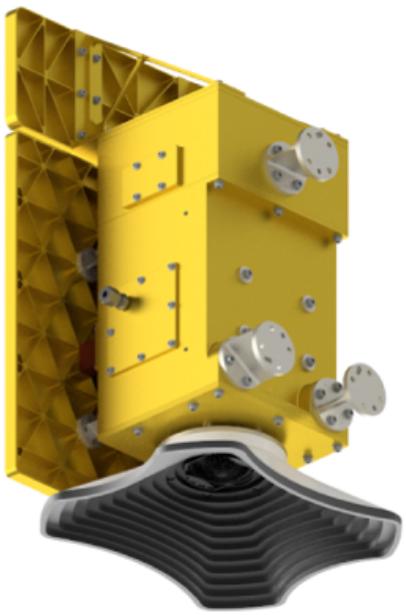

**Figure 2.8:** The HARP2 polarimeter.[8].

[7]URL: `https://suzaku.eorc.jaxa.jp/GCOM_C/resources/files/FR3.R4.4_Okamura_SGLI_IGARSS2019.pdf`, last accessed 15-06-2025

3MI, or the 'Multi-View Multi-Channel Multi-Polarisation Imaging' mission, is a mission planned for launch sometime in the mid-2020's on the EUMETSAT Polar System Second Generation platform. It is designed for aerosol and cloud characterisation for climate and atmospheric composition monitoring [Dubovik et al., 2019]. The mission will allow the research of aerosol load in the atmosphere and its impact on the radiative forcing of the atmosphere. The instrument provides multi-spectral multi-polarisation and multi-angular images of the outgoing radiation from the top of the atmosphere [Dubovik et al., 2019]. The 3MI uses a system of filter wheels for the purposes of measuring the polarisation within a wheel rotation speed of 5.5 seconds [Dubovik et al., 2019]. The opto-mechanical unit of the 3MI mission, including the filter wheels, is shown in Figure 2.9. The instrument has POLDER heritage and works in a similar fashion with polarisers at -60°, 0° and 60° which are used to obtain the polarisation state as the filter wheel passes the light through different filters.

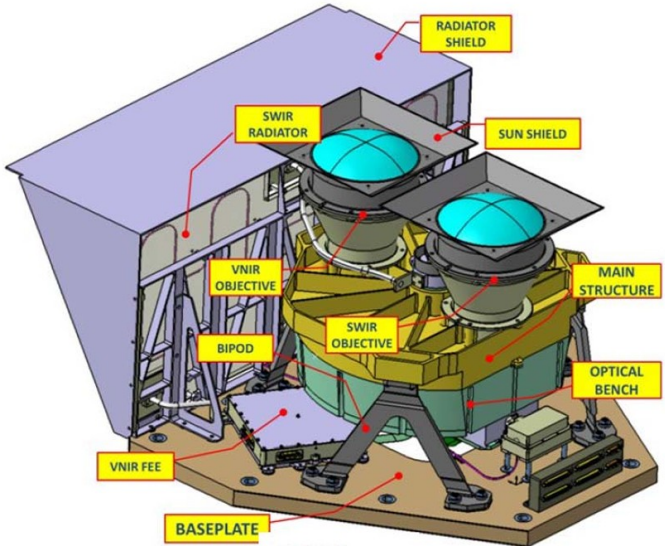


**Figure 2.9:** The opto-mechanical unit of the 3MI mission[Biron et al., 2013].

Another instrument which has been created for polarisation measurements is the Multi-Angle Imager for Aerosols (MAIA). This instrument is based on a spectropolarimetric camera using a polarimetric retardance modulation technique. Polarisation is measured by having the retardance modulator in the optical path and wiregrid polarisers in the focal plane spectral filter assembly [Dubovik et al., 2019]. The modulator consists of 2 photoelastic modulators and a pair of achromatic quarter waveplates, shown in Figure 2.10. The intensity and any polarisation other than circular polarisation can be measured with this technique. The instrument was meant to launch on the OTB-2 satellites in 2022 [Dubovik et al., 2019], however, no evidence can be found of the launch having taken place yet, hence it is likely delayed. Much like the previous mission examples from Dubovik et al. [2019]'s summary, the instrument is made for aerosol measurements and cloud science.

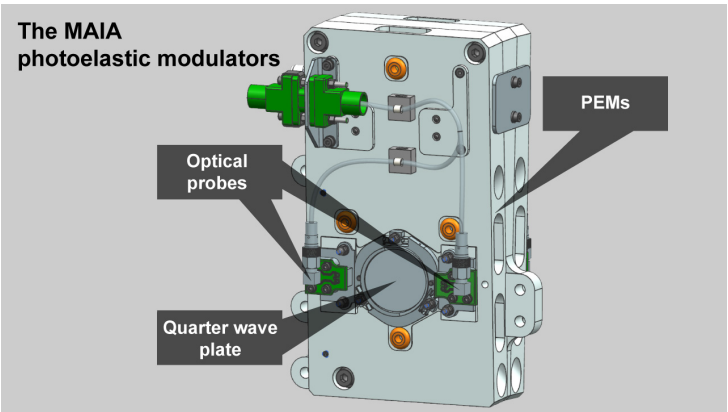


**Figure 2.10:** The MAIA photoelastic modulators and quarter waveplate[9].

[8]URL: https://pace.oceansciences.org/harp2.htm, last accessed 15-06-2025
[9]URL: https://maia.jpl.nasa.gov/mission/, last accessed 15-06-2025

The SPEX series of instruments are a series of polarimetry instruments which are of particular relevance to the thesis topic. SPEX stands for Spectro-Polarimetric Experiment instruments, and the main instrument, SpexOne, was designed for the NASA PACE mission [Dubovik et al., 2019]. The SpexOne instrument, shown in Figure 2.11, is designed to "provide a very high polarimetric accuracy, measurements in the near-UV (down to 385 nm), high spatial sampling, and many measurements per individual ground pixel" [Dubovik et al., 2019]. What makes SpexOne more relevant to the thesis in particular, is the use of passive optical components resulting in the ability to characterise the full linear polarisation state of a scene instantaneously [Campo et al., 2018]. The SpexOne is a multi-angle spectro-polarimeter which encodes the polarisation state of the incident light to a sinusoidal modulation which can be used to determine the precise linear polarisation state [Campo et al., 2018]. The instrument is based on Tropomi heritage and, although PACE is not a cubesat, it is designed to be compatible with 12U cubesats while still being able to accomplish full linear polarisation modulation [Dubovik et al., 2019].

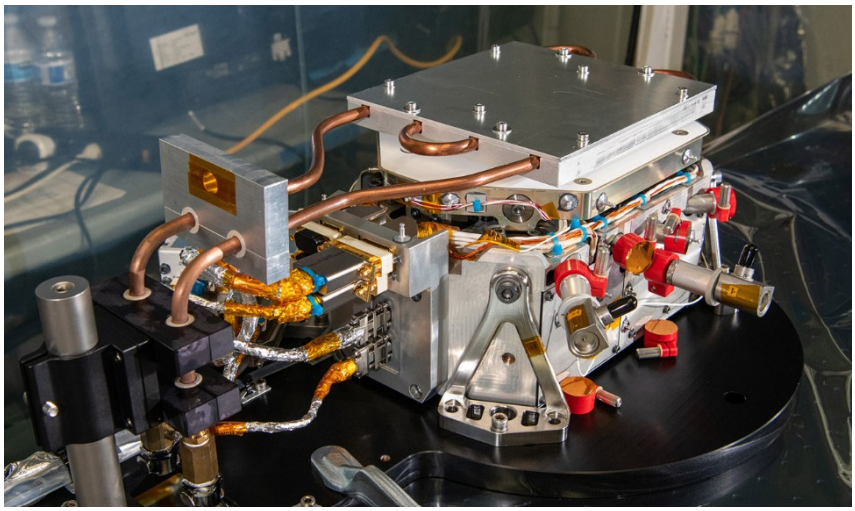

**Figure 2.11:** The SPEXone during testing[10].

This short summary of various currently existing or planned missions serves to that polarimetry in space is an active and developing space research direction. It also demonstrates some of the limitations of space polarimetry at this time. Throughout all of the examples, none are inherently designed to measure circular polarisation. Furthermore, the designs of the instruments, such as for example POLDER, 3MI or MAIA, require the use of either successive measurements, rotating filter wheels or multiple modulators and waveplates which add both complexity and volume to the instrument. Despite the sacrifices which had to be made with regards to not being able to measure circular polarisation, the instruments still require many different parts in order to calculate the polarisation state. As these examples also aim to perform spectropolarimetry, multiple wavelengths must also be treated which results in requirements such as the rotating filter wheel in the case of the POLDER instrument. The HARP mission and POLDER, despite performing measurements on multiple wavelengths, still have to establish which wavelengths can have measurements performed resulting in either 4 or 9 available wavelengths respectively.

These limitations of the previous missions open a gap in research of spectropolarimetry which can also perform a full measurement of the entire polarisation state. The spectropolarimetry method which this thesis is based on, aims to fill this gap and produce an instrument capable of not only achieving spectropolarimetry of light at any polarisation state, but also doing so without the need to include the multiple rotating elements, or use more than one modulator and waveplate. Instead, this method aims to achieve a more complete spectropolarimetric measurement in a single snapshot while only using a single stationary modulator, a single unmoving linear polariser and a dispersive element. How this is achieved, and the fundamentals of specifically the modulator design which makes this possible are introduced next in chapter 3.

[10] URL: `https://pace.oceansciences.org/spexone.htm`, last accessed 15-06-2025

# 3

# The Birefringent Modulator

In subsection 2.3.2, a brief mention of modulators was made in the context of polarisation components. Here this will be elaborated on primarily regarding the specific instrument which the thesis is based on.

In general, the modulator is a key component in polarimeter design. The modulator is used in order to create a controlled modulation of the light which in turn is transformed into intensities which can be measured on a detector. In modulators which work on similar principles to the one used in the thesis, the modulation of the light allows the distinguishing of different polarisation states in such a way that, when used alongside an analyser, a pattern of intensities can be measured at the detector. To obtain the polarisation from the measurements, the difference of intensities between two different predefined states of the modulator can be divided by the total intensity [Hough, 2006]. The difference in intensities can be translated to a mathematical form, after which a numerical model can be used to obtain the polarisation state of the light entering the system.

The analyser itself is often a linear polariser, Wollaston prism or other form of dual-beam polarising prism [Hough, 2006], and is used to make the differently modulated light visible as an intensity difference.

In the modulator being discussed in this thesis specifically, rather than having multiple predefined states of the modulator, the modulator works alongside a linear polariser (as an analyser) to create a pattern of intensity which is used to obtain the difference in intensities from a single measurement. A dispersive element following the linear polariser makes the design capable of spectropolarimetry, and thus the analysis of multiple wavelengths.

For this thesis project, only the modulator is essential to investigating and answering the research question. The analyser or dispersive element are not required because the Fresnel phenomena which are being looked into occur within the modulator, and create fluctuations in the intensity patterns even without the presence of an analyser. Despite this, understanding how the modulator is embedded into the full instrument is still useful for comprehending why the design of the modulator is important and why the question was posed in the first place.

In the rest of this chapter, the modulator design which is the central focal point of the thesis is presented in more detail. First of all, the principle of the modulator is presented in section 3.1. After this, the experimental results which resulted in the creation of this thesis research topic are discussed in section 3.2.

## 3.1. Principle of the Modulator

The modulator which is being researched and which will be the main element of the polarimeter instrument is an already existing design being researched by Dr. Bogdan Vasilescu.

In the research paper related to the original development of the space spectropolarimeter for full-Stokes parameter retrieval, Vasilescu et al. [2020a] describes how the design of this specific modulator may provide a tool with a high potential for space application.

The modulator is based on birefringent prisms, with key design points being the lack of rotating elements, compact design, and ability to cover the entire Stokes vector across a wide range of wavelengths. Additionally, [Vasilescu et al., 2020b] expresses the design's high polarimetric efficiency, which adds to the benefits the modulator can bring when compared to currently existing designs. Polarimetric efficiency refers to the robustness

of the method, and is used to compare different designs in terms of their efficacy.

In general, polarisation modulators are used to transform the polarisation states of the beam in more complex ways than a regular half or quarter-waveplate could. Based on how the modulator is designed, the light can be manipulated through a change of phase at different points in the modulator prism, or by having a waveplate rotate and measuring the result through time. The resulting transmitted light can be measured with the help of an analyser [Vasilescu et al., 2023] to establish information about the incident rays into the modulator. In the case of the modulator being researched for this thesis, the light is modulated into an output which can be used to fully determine the incident polarisation state through a changing thickness of the prisms. This changes the phase of the light at each position on the vertical axis to give a set of outputs which can be used together for the intended goal.

The function of the modulator can be achieved with other forms of modulator as well, but this specific modulator design used for this research is created to focus on the issues of size and complexity. Normally, to be able to perform polarimetry, especially full Stokes snapshot spectropolarimetry, large, complex and costly components are needed. Instead, the new modulator will use only birefringent prisms with no moving or large scale parts to attempt continuous modulation of the signal in the vertical direction [Vasilescu et al., 2020a].

In order to achieve this, some key requirements had to be taken into account which led to the choice of material, the shape, and the layout of the prisms. For the material choice, for example, the wavelength dependence of birefringent materials is important.

Meeting the requirements resulted in a final design consisting of 3 birefringent uniaxial prisms made out of $MgF_2$. The prisms are attached to one another to create a full 'block' which is the modulator as a whole. The modulator is depicted in Figure 3.1 which uses a detector intensity profile from Vasilescu [2025]'s paper.

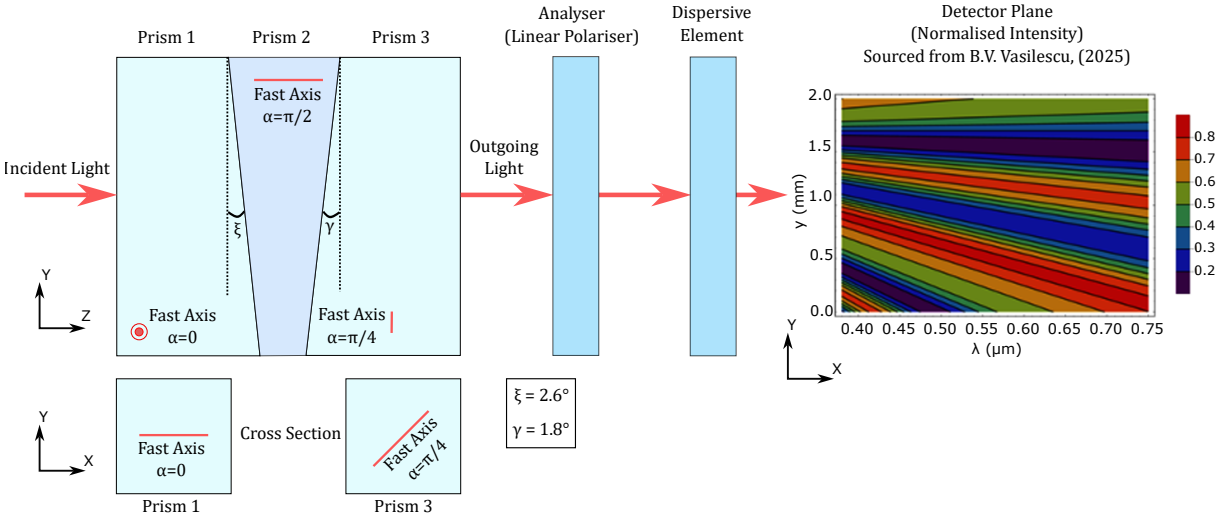


**Figure 3.1:** Modulator design and output when combined with an analyser and dispersive element. Shape of the modulator is exaggerated for clarity. The detector plane results are an example results figure for a smaller area of the modulator taken from Vasilescu [2025].

In the figure, the apex angles and fast-axis directions are clearly depicted. This is because the design relies on the shapes of the prisms and the fast-axis directions to create the continuous modulation of the output light in the vertical direction. To achieve this effect, the first wedge is designed with an apex angle $\xi = 2.6°$ and a fast-axis orientation along the x-axis. This induces a continuous phase variation along the vertical [Vasilescu et al., 2020a].

The second prism has a fast-axis oriented along the z-axis and is placed as a structural support. This element is assumed not to affect the beam in any significant way, but rather serves to ensure the robustness of the design [Vasilescu et al., 2020a]. For the sake of this thesis, this assumption is maintained as a simplification of the modulator. Determining the true effect of the second element is beyond the scope of the thesis.

The third prism once again performs an active role in the modulator. Here, the apex angle is $\gamma = 1.8°$ and the fast-axis is directed at 45° with respect to the x-axis in the x-y plane. This element adds an additional phase

difference between the components of the beam along the vertical axis. With this second phase difference, a modulation of the light is produced which can then be analysed in the analyser.

A summary of all of the specifications of the modulator is provided in Figure 3.2.

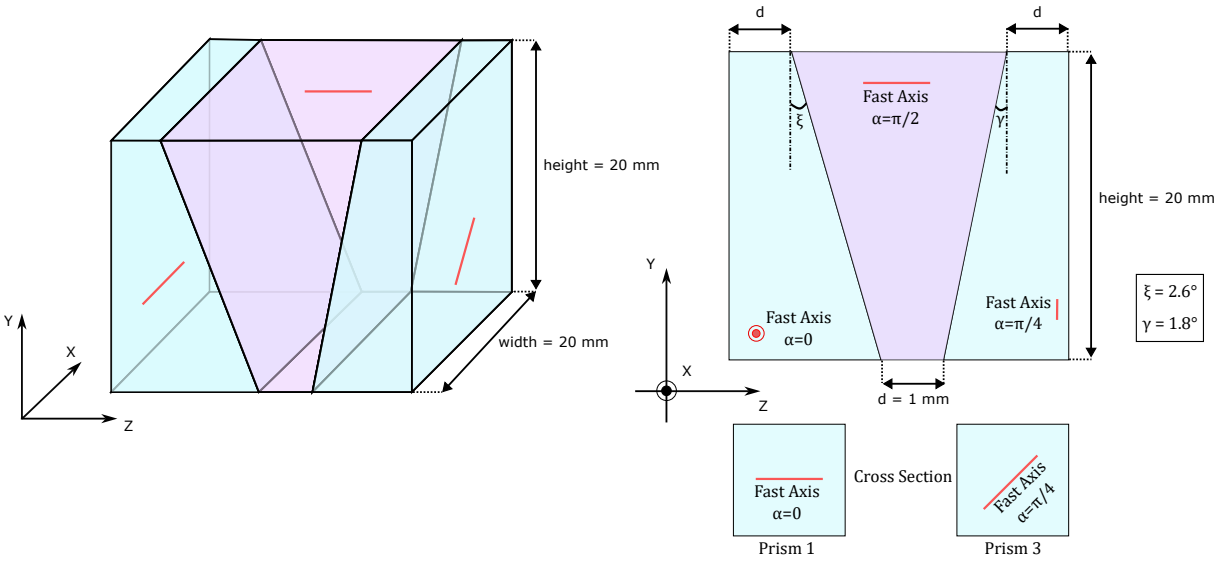


**Figure 3.2:** Specification of the modulator as given to the manufacturer.

The active prisms each function as waveplates, but rather than half or quarter waveplates, the prisms have a varying phase shift depending on the height at which the ray passes through them. The thickness variation of the prisms changes the duration of time in which the ray is passing through the birefringent material. The phase of the light is altered by exposure to the birefringent medium, resulting in the phase changing differently based on the thickness. This means that at every height, the modulator active prisms work as a waveplate with the corresponding phase shift achieved with the corresponding thickness.

The analyser, depicted in Figure 3.1, is a linear polariser and is set to a certain predefined angle. This only allows a certain polarisation of light through. The result of having the linear polariser here is a sinusoidal pattern on the detector. The dispersive element is used to allow for multiple wavelengths to be studied simultaneously, thus making the method capable of spectropolarimetric measurements. Comparison between different parts of the pattern and the corresponding modulation for that specific region results in a complete derivation of the incident polarisation state. Because of the modulator design, it is also possible to determine whether the light is unpolarised or circularly polarised, as well as all partial polarisation states in between through the fact that the phase of the light is altered differently across the entire y axis of the modulator. In Vasilescu et al. [2020b] it is proven that this modulator leads to unique results for any given wavelength.

For this thesis, the modulator was simplified with respect to the original design through the removal of the second prism. It has already been stated that this prism, in theory, does not serve an active scientific purpose. Rather, as a structural material, for all intents and purposes it does not provide any added value when investigating the modulator intensity fluctuations. The difference between the modulator with, and without, the second prism is simply the refractive index the light interacts with when travelling from the exit of prism 1 to prism 3. Therefore, from this instance onward, the modulator will be considered as just prism 1 and prism 3 with air surrounding them. Any reference to 'the second prism' instead refers to the second of the active prisms, hence prism 3. For the purposes of testing the assumption that the second prism does not change the function of the modulator, there already exist two versions of the physical modulator which can be used for lab work. One of these is the modulator in its intended form, with all 3 prisms glued together. The other has the second prism removed and can therefore be used in experimental testing for this thesis. This means that using this assumption does not hinder any validation experiments.

## 3.2. Current Research Level

In section 3.1, the fundamentals of how the modulator works have been discussed. It is now necessary to link this into the current state of the research into the spectropolarimetry method, and specifically into what led to the conception of this thesis in the first place.

The method for performing spectropolarimetry using the modulator design presented in this chapter is based on interpreting the intensity pattern which is observed after the analyser. One of the fundamental expectations based on the theoretical calculations and models used when first showcasing the potential of the method, is that the spectropolarimeter functions as a combination of 2 active waveplate elements (the prisms) followed by a simple linear polariser. As the polarisation state of the light exiting the modulator varies along the height, as caused by the changing thicknesses of the birefringent prisms, it is expected that an intensity pattern will form after the analyser. Waveplates, however, do not affect the overall intensity of the light passing through them, meaning that there is no expectation of a fluctuation to have occurred prior to the linear polariser. Despite the changing polarisation state of the light, the intensity of the rays is usually the same at the output of a waveplate.

As of the beginning of the thesis, the modulator design had already been finalised and manufactured. Models and simulations of the modulator had also already been used to verify the theory behind the modulator design. According to all of the models and theoretical calculations, it was demonstrated that the modulator is capable of producing intensity fluctuations after the linear polariser which correspond to a specific initial incident polarisation state. Furthermore, in all of the models and simulations, the intensity of the light did not change throughout the entire setup prior to encountering the analyser. The reason this is relevant is because, once the research moved on to the validation of the modulator design, an unexpected intensity variation occurred even without the presence of the analyser. It was also observed that this pattern did not occur if only one of the prisms was used. It was necessary for both active prisms to be present for these variations to appear.

To initially investigate these fluctuation patterns, an experiment was performed using a lab setup as shown in Figure 3.3.

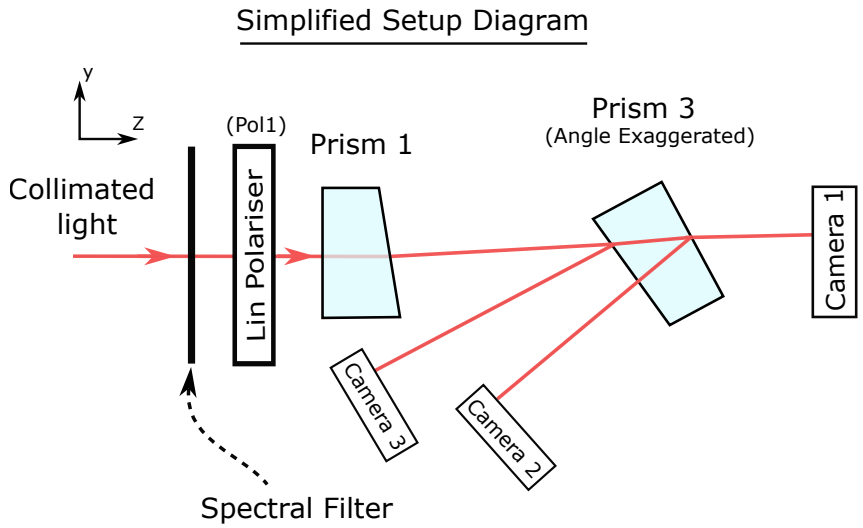


**Figure 3.3:** Simplified setup diagram of the experiment performed to showcase the fluctuations.

In this experiment, prism 2 is completely neglected and the two active prisms, prism 1 and prism 3 are placed such that the variation of intensity can be measured from the different reflections and transmissions of the surfaces of the second prism. This could serve to indicate at what stage the variations begin to appear as it was already confirmed that it does not happen if only a single prism is used. To experiment with angles of incidence and the effect which the positioning of prism 3 has on the intensity variation, the angle at which the third prism is placed with respect to the y axis is changed.

Some of the results of this experiment are shown in Figure 3.4 where the transmission was measured at camera 1. The pol1 angle refers to the orientation of the linear polariser which then dictates the incident polarisation state of the light into the prisms. On the other axis, Pr3 angle refers to the specific angle of prism 3 with respect to its vertical position.

At this stage, the original hypothesis that Fresnel behaviour at the boundaries caused the variation was proposed. In the case of the modulator under investigation, there are 4 boundaries present. If only the active prisms are taken, these amount to boundaries between the air and the entry surfaces of each prism, as well as the exit surfaces of each prism with the air. Each boundary adds another layer of uncertainty in how the results

are affected as none of the models or simulations take the Fresnel reflection and transmission behaviour into account.

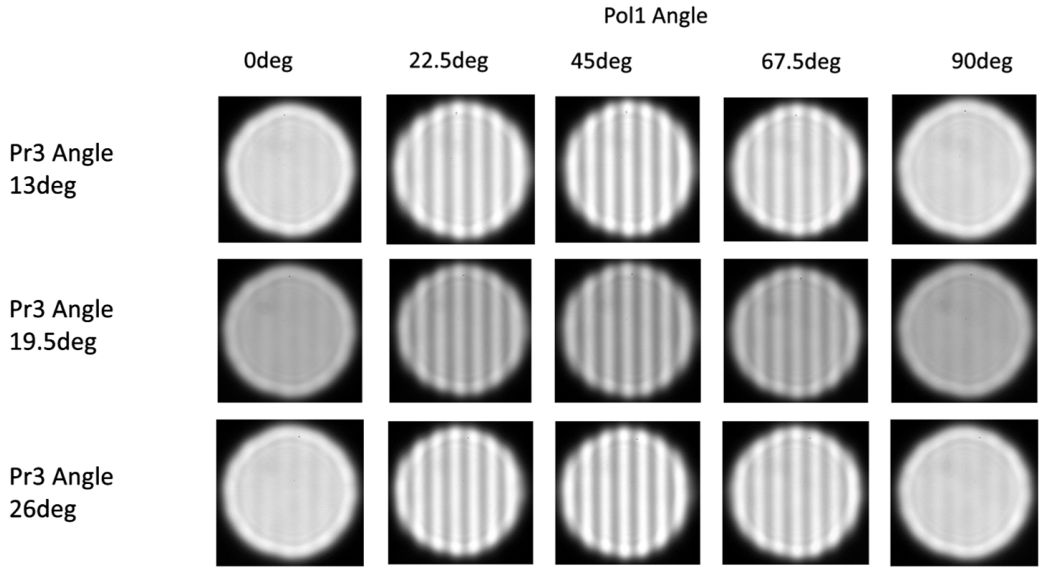


**Figure 3.4:** Experimental Results showing fluctuations in the modulator at varying incident polarizations and angles of the third prism. It was expected no fluctuations should be present. Fluctuations are greatest at 45° irrespective of angle of incidence, and are also visible with the modulator in the ideal configuration. The images shown are taken prior to the thesis by the TU Delft members working on the spectropolarimetry setup.

# 4

# Mathematical Formulation

Up until this point, the background information on polarisation and the modulator have been provided. Now, in this chapter, the mathematical formulations will be provided. The main mathematical formalisms used to represent polarisation are presented in section 4.1. After this, section 4.2 presents Fresnel phenomena and how they are represented in the same formalisms. Finally, the mathematical representation of the whole modulator is shown in section 4.3.

## 4.1. Mathematical Formalisms of Polarisation

When it comes to the mathematical formulation of polarisation, there are multiple methods which can be applied based on which aspect of polarisation is most relevant to the project. Choosing the correct method is important as it can drastically increase or decrease the effort required for modelling the polariser modulator. There are two main formalisms, Mueller-Stokes formalism and Jones formalism, which are considered for this thesis and both of these will be presented here.

### **4.1.1.** Mueller-Stokes Formalism

From the previous work done on the instrument, and from research into the topic, the most common and useful formalism for this research is the Mueller-Stokes formalism. This has been used in previous papers on both the modulator being worked on, and in polarimetry papers in general. This makes it versatile and well documented for the main use-case which is being investigated. Mueller-Stokes is also a good fit for the project as it allows the use of both polarised and unpolarised light as an input to calculate the output electromagnetic wave from a system.

The Mueller-Stokes formalism is a combination of Stokes parametrisation of the polarisation state, with Mueller matrices used to alter the parameters and simulate the light passing through optical elements.

**Stokes Parameters**
Stokes defines the polarisation state in a vector consisting of 4 parameters as shown in Equation 4.1 below [Collett, 2005]:

$$\mathbf{S} = \begin{bmatrix} S_0 \\ S_1 \\ S_2 \\ S_3 \end{bmatrix} = \begin{bmatrix} \langle E_x^2 \rangle + \langle E_y^2 \rangle \\ \langle E_x^2 \rangle - \langle E_y^2 \rangle \\ 2\langle E_x E_y \cos[\phi_y(t) - \phi_x(t)] \rangle \\ 2\langle E_x E_y \sin[\phi_y(t) - \phi_x(t)] \rangle \end{bmatrix} = \begin{bmatrix} \langle I_{0^\circ} \rangle + \langle I_{90^\circ} \rangle \\ \langle I_{0^\circ} \rangle - \langle I_{90^\circ} \rangle \\ \langle I_{45^\circ} \rangle - \langle I_{135^\circ} \rangle \\ \langle I_{LC} \rangle - \langle I_{RC} \rangle \end{bmatrix} \tag{4.1}$$

These parameters are sometimes referred to as I, Q, U and V instead of $S_0$, $S_1$, $S_2$ and $S_3$, but for this thesis the latter representation will be maintained.

The parameters are, in essence, representing different aspects of the polarisation state in order to define the polarisation ellipse. As shown by Collett [2005], the parameters are related through Equation 4.2 in the case of fully polarised light, and Equation 4.3 in the case of partially polarised light.

$$S_0^2 = S_1^2 + S_2^2 + S_3^2 \tag{4.2}$$

$$S_0^2 > S_1^2 + S_2^2 + S_3^2 \tag{4.3}$$

$S_0$ describes the total intensity of the beam, $S_1$ describes whether the beam is horizontally or vertically polarised by the difference between the horizontal and vertical polarised light intensities, $S_2$ describes the polarisation of light at 45° by the difference between polarisation at +45° and −45°, and finally $S_3$ describes the circular polarisation of the beam through the difference between left and right circular polarisation [Schmidt, 2022].

In this way, it is possible to describe the light fully, even when elliptically polarised or completely unpolarised, using measurable values. To represent partially polarised light, an additional term has to be included. This term is the degree of polarisation[Collett, 2005].

The degree of polarisation can be obtained with Equation 4.4.

$$P = \frac{\sqrt{S_1^2 + S_2^2 + S_3^2}}{S_0^2} \tag{4.4}$$

Here, $P$ can only be between 0 and 1 as light can only range from unpolarised to fully polarised at 0 and 1, respectively. Values in between 0 and 1 correspond to varying degrees of partial polarisation.

As can be seen, Stokes gives a large amount of flexibility when describing the polarisation state.

To add to the context of the thesis, it can now be understood that when full-Stokes snapshot polarimetry is used to describe what an instrument can do, it is referring to the ability of the instrument to measure every parameter in the Stokes vector in a single 'snapshot' image.

**Mueller Matrices**

The Stokes notation alone is useful for polarisation state description. To get a model of how the state changes when the beam passes through optical elements, Mueller matrices are needed. Mueller matrices are 4 x 4 matrices which are multiplied sequentially with the Stokes input vector, to obtain the output Stokes vector. Each Mueller matrix represents an optical element which the beam is passing through. For a multi-element system, the computation is done as:

$$\mathbf{S}_{out} = M_{device2}\,(M_{device1}\,\mathbf{S}_{in})$$

Some examples and general forms of Mueller matrices for the different optical instruments are given below [Collett, 2005], [Kliger et al., 1990]:

- Horizontal Linear Polariser

$$M = \frac{1}{2}\begin{bmatrix} 1 & 1 & 0 & 0 \\ 1 & 1 & 0 & 0 \\ 0 & 0 & 0 & 0 \\ 0 & 0 & 0 & 0 \end{bmatrix} \tag{4.5}$$

- Vertical Linear Polariser

$$M = \frac{1}{2}\begin{bmatrix} 1 & -1 & 0 & 0 \\ -1 & 1 & 0 & 0 \\ 0 & 0 & 0 & 0 \\ 0 & 0 & 0 & 0 \end{bmatrix} \tag{4.6}$$

- Waveplate with a $\Delta\phi$ phaseshift, where $\Delta\phi = \frac{2\pi}{\lambda}(n_o - n_e)d$. Here, $n_o$ and $n_e$ are the refractive indices of the waveplate, where $n_o$ is the fast-axis refractive index, and $n_e$ is the slow-axis refractive index. The d stands for the thickness of the waveplate (or distance travelled by the light through the waveplate). The fast-axis is horizontal. [Collett, 2005]

$$M = \frac{1}{2}\begin{bmatrix} 1 & 0 & 0 & 0 \\ 0 & 1 & 0 & 0 \\ 0 & 0 & \cos\Delta\phi & -\sin\Delta\phi \\ 0 & 0 & \sin\Delta\phi & \cos\Delta\phi \end{bmatrix} \tag{4.7}$$

Each of these examples has a specific orientation, but it is also required that the matrices can be adapted to the actual orientations of the components even when they don't align perfectly with one of the standardised orientations. To do this, it is possible to use rotation matrices.

The rotation matrices are applied when the coordinate system needs to be shifted for the Mueller matrix and are used in pairs. One rotation matrix aligns the coordinate system of the Stokes vector to the coordinate system of the component (angle $\theta$), then, another rotation matrix inverts it back to the original coordinate system (angle $-\theta$). These rotation matrices look as follows [Collett, 2005]:

$$M = \begin{bmatrix} 1 & 0 & 0 & 0 \\ 0 & \cos 2\theta & \sin 2\theta & 0 \\ 0 & -\sin 2\theta & \cos 2\theta & 0 \\ 0 & 0 & 0 & 1 \end{bmatrix} \tag{4.8}$$

Rotation matrices can easily be integrated into the matrices for the components given above to create 'rotatable' versions. Some examples are given below:

- Rotatable Linear Polariser, where $\theta$ is the angle of the polariser [Collett, 2005]

$$M = \frac{1}{2}\begin{bmatrix} 1 & \cos 2\theta & \sin 2\theta & 0 \\ \cos 2\theta & \cos^2 2\theta & \sin 2\theta\cos 2\theta & 0 \\ \sin 2\theta & \sin 2\theta\cos 2\theta & \sin^2 2\theta & 0 \\ 0 & 0 & 0 & 0 \end{bmatrix} \tag{4.9}$$

- Rotatable waveplate, where $\theta$ is the orientation of the waveplate and $\Delta\phi$ is the phaseshift [Collett, 2005].

$$M = \begin{bmatrix} 1 & 0 & 0 & 0 \\ 0 & \cos^2 2\theta + \cos\Delta\phi\sin^2 2\theta & (1-\cos\Delta\phi)\sin 2\theta\cos 2\theta & \sin\Delta\phi\sin 2\theta \\ 0 & (1-\cos\Delta\phi)\sin 2\theta\cos 2\theta & \sin^2 2\theta + \cos\Delta\phi\cos^2 2\theta & -\sin\Delta\phi\cos 2\theta \\ 0 & -\sin\Delta\phi\sin 2\theta & \sin\Delta\phi\cos 2\theta & \cos\Delta\phi \end{bmatrix} \tag{4.10}$$

### 4.1.2. Jones Formalism

In order to be able to investigate the sources of error which have been observed more completely, and due to difficulties encountered with Fresnel behaviour and birefringence in Mueller-Stokes, another widely popular formalism was also looked into. The Jones matrix formalism is generally comparable with Stokes and can model birefringence more easily. This is because Jones primarily represents polarisation in terms of the x and y components of the electric field. Because of this, it improves the ease with which certain calculations can be done with respect to the coordinate system and how the polarisation state changes in each direction. Jones, however, has the disadvantage that it cannot be performed on unpolarised or partially polarised sources [Collett, 2005].

The Jones form for the polarisation state is simply a vector with 2 elements which represent the electric field components. The Jones formulation for the polarisation state is given by Equation 4.11.

$$\mathbf{E} = \begin{bmatrix} E_x \\ E_y \end{bmatrix} = \begin{bmatrix} E_{0x}e^{i\phi_x} \\ E_{0y}e^{i\phi_y} \end{bmatrix} \tag{4.11}$$

Here $i = \sqrt{-1}$. From this vector notation, the intensity can be calculated with Equation 4.12.

$$I = \begin{bmatrix} E_x^* & E_y^* \end{bmatrix}\begin{bmatrix} E_x \\ E_y \end{bmatrix} = E_x {E_x}^* + E_y E_y^* \tag{4.12}$$

Rather than using Mueller matrices, Jones formalism has its own version of optical element matrices. These are 2 x 2 matrices which function in the same way as Mueller matrices in terms of the calculation when combined with Jones vectors. Examples for different elements are seen here:

Some examples and general forms of Jones matrices for different optical instruments are given below:

- Horizontal Linear Polariser

$$M_J = \begin{bmatrix} 1 & 0 \\ 0 & 0 \end{bmatrix} \tag{4.13}$$

- Vertical Linear Polariser

$$M_J = \begin{bmatrix} 0 & 0 \\ 0 & 1 \end{bmatrix} \tag{4.14}$$

- Waveplate with a $\Delta\phi$ phaseshift, where $\Delta\phi = \frac{2\pi}{\lambda}(n_o - n_e)d$. Here, again, $n_o$ and $n_e$ are the refractive indices of the waveplate, where $n_o$ is the fast-axis refractive index, and $n_e$ is the slow-axis refractive index. The d, much like for Mueller-Stokes, stands for the thickness of the waveplate (or distance travelled by the light through the waveplate). The fast-axis is horizontal [Collett, 2005].

$$M_J = \begin{bmatrix} e^{i(\Delta\phi/2)} & 0 \\ 0 & e^{-i(\Delta\phi/2)} \end{bmatrix} \tag{4.15}$$

Much like in the Mueller-Stokes case, rotation matrices also exist for Jones formalism. They are applied in the same way as for the Mueller-Stokes versions. In Jones, they look as shown in Equation 4.16.

$$M_J = \begin{bmatrix} \cos\theta & \sin\theta \\ -\sin\theta & \cos\theta \end{bmatrix} \tag{4.16}$$

The rotatable versions of the Jones matrices can be found here:

- Rotatable Linear Polariser, where $\theta$ is the angle of the polariser

$$M_J = \begin{bmatrix} \cos^2\theta & \cos\theta\sin\theta \\ \cos\theta\sin\theta & \sin^2\theta \end{bmatrix} \tag{4.17}$$

- Rotatable waveplate, where $\theta$ is the orientation of the waveplate and $\Delta\phi$ is the phaseshift [Collett, 2005].

$$M_J = \begin{bmatrix} \cos\frac{\Delta\phi}{2} + i\sin\frac{\Delta\phi}{2}\cos 2\theta & i\sin\frac{\Delta\phi}{2}\sin 2\theta \\ i\sin\frac{\Delta\phi}{2}\sin 2\theta & \cos\frac{\Delta\phi}{2} - i\sin\frac{\Delta\phi}{2}\cos 2\theta \end{bmatrix} \tag{4.18}$$

## 4.2. Fresnel Behaviour Mathematical Formalism

Fresnel behaviour has already been briefly discussed in subsection 2.3.1 in terms of what it represents. Now it is also necessary to define it properly mathematically. Fresnel phenomena can be described using Fresnel coefficients which can calculate the amount of light reflected relative to the amount which is transmitted [Weidlich and Wilkie, 2008]. Mathematically, the Fresnel coefficients are defined in the parallel and perpendicular directions with respect to the plane of incidence. These directions are commonly noted as $p$ and $s$ [Chaumette, 2021] where p is parallel and s is perpendicular to the plane of incidence. Because of the nature of polarised light, both directions are affected differently and, therefore, have their own coefficients.

### 4.2.1. Mueller-Stokes Formalism

As Stokes formalism is based on 4 parameters all related to the polarisation state of the light at various angles, representing Fresnel reflections in Stokes form presents a challenge. Fresnel coefficients are in parallel and perpendicular directions and do not inherently tie into the Mueller-Stokes system. From Collett [2005], it is possible to note down the equations for the Fresnel coefficients. The coefficients for reflection in both parallel and perpendicular directions are shown in Equation 4.19 and Equation 4.20, while the coefficients for transmission are found in Equation 4.21 and Equation 4.22.

$$\rho_s = \left(\frac{R_s}{E_s}\right)^2 = \left(\frac{\sin\alpha_-}{\sin\alpha_+}\right)^2 \tag{4.19}$$

$$\rho_p = \left(\frac{R_p}{E_p}\right)^2 = \left(\frac{\tan\alpha_-}{\tan\alpha_+}\right)^2 \tag{4.20}$$

$$\tau_s = \frac{n\cos\sigma_r}{\cos\sigma_i}\left(\frac{T_s}{E_s}\right)^2 = \frac{\sin 2\sigma_i \sin 2\sigma_r}{\sin^2\alpha_+} \tag{4.21}$$

$$\tau_p = \frac{n\cos\sigma_r}{\cos\sigma_i}\left(\frac{T_p}{E_p}\right)^2 = \frac{\sin 2\sigma_i \sin 2\sigma_r}{\sin^2\alpha_+ \cos^2\alpha_-} \tag{4.22}$$

In these formulas, taken from Collett [2005], $\sigma_i$ is the incidence angle, $\sigma_r$ is the refraction angle, $n$ is the refractive index of the material being entered into, and $\alpha_\pm$ is given by $\sigma_i \pm \sigma_r$. $R$ and $T$ represent the reflected and the transmitted field, respectively.

For these coefficients, $\rho_s + \tau_s = 1$ and similarly, $\rho_p + \tau_p = 1$ with the value of the coefficients being between 0 and 1.

Based on Collett [1971] and Collett [2005], it appears possible to portray Fresnel reflections as an additional Mueller matrix as though it were an additional component each time a material boundary is passed, and therefore as a Mueller matrix. The Mueller matrices are given separately for reflection and transmission as shown in Equation 4.23 and Equation 4.24.

$$M_\rho = \frac{1}{2}\begin{bmatrix} \rho_s+\rho_p & \rho_s-\rho_p & 0 & 0 \\ \rho_s-\rho_p & \rho_s+\rho_p & 0 & 0 \\ 0 & 0 & 2\sqrt{\rho_s\rho_p} & 0 \\ 0 & 0 & 0 & 2\sqrt{\rho_s\rho_p} \end{bmatrix} \tag{4.23}$$

$$M_\tau = \frac{1}{2}\begin{bmatrix} \tau_s+\tau_p & \tau_s-\tau_p & 0 & 0 \\ \tau_s-\tau_p & \tau_s+\tau_p & 0 & 0 \\ 0 & 0 & 2\sqrt{\tau_s\tau_p} & 0 \\ 0 & 0 & 0 & 2\sqrt{\tau_s\tau_p} \end{bmatrix} \tag{4.24}$$

In cases where the angle of incidence is 0°, the coefficients are no longer defined correctly. Therefore, based on Collett [2005], the mueller matrix takes on a simplified form for both transmission and reflection as seen in Equation 4.25 and Equation 4.26.

$$M_\rho = \left(\frac{n-1}{n+1}\right)^2 \begin{bmatrix} 1 & 0 & 0 & 0 \\ 0 & 1 & 0 & 0 \\ 0 & 0 & -1 & 0 \\ 0 & 0 & 0 & -1 \end{bmatrix} \tag{4.25}$$

$$M_\tau = \frac{4n}{(n+1)^2} \begin{bmatrix} 1 & 0 & 0 & 0 \\ 0 & 1 & 0 & 0 \\ 0 & 0 & 1 & 0 \\ 0 & 0 & 0 & 1 \end{bmatrix} \tag{4.26}$$

### 4.2.2. Jones Formalism

For Jones formalism, the Fresnel coefficients are far more compatible, as the Jones form is based on the parallel and perpendicular directions much like the Fresnel coefficients. This should allow the Fresnel coefficients to be applied to the parameters of a Jones vector much more simply than for Stokes.

Similarly to Mueller-Stokes, Jones formalism also has matrices for Fresnel boundary behaviour. In the case of a birefringent material, Jones is also far simpler as each axis can be treated independently, but it also requires a new definition for the Fresnel coefficients. These are given in Equation 4.27 to Equation 4.30.

$$r_s = \frac{n_1\cos\sigma_i - n_s\cos\sigma_{r_s}}{n_1\cos\sigma_i + n_s\cos\sigma_{r_s}} \tag{4.27}$$

$$r_p = \frac{n_p\cos\sigma_i - n_1\cos\sigma_{r_p}}{n_p\cos\sigma_i + n_1\cos\sigma_{r_p}} \tag{4.28}$$

$$t_s = \frac{2n_1 \cos\sigma_i}{n_1 \cos\sigma_i + n_s \cos\sigma_{r_s}} \tag{4.29}$$

$$t_p = \frac{2n_1 \cos\sigma_i}{n_p \cos\sigma_i + n_1 \cos\sigma_{r_p}} \tag{4.30}$$

Here, $n_1$ represents the refractive index of air but can also be used for whichever material is outside of the prism being entered. Furthermore, $\sigma_r$ is always the refraction angle in these equations.

In Jones formalism, the Fresnel matrices are of the forms shown in Equation 4.31 and Equation 4.32 [Peatross and Ware, 2015].

$$M_{J_r} = \begin{bmatrix} -r_p & 0 \\ 0 & r_s \end{bmatrix} \tag{4.31}$$

$$M_{J_t} = \begin{bmatrix} t_p & 0 \\ 0 & t_s \end{bmatrix} \tag{4.32}$$

## 4.3. Mathematical Representation of the Modulator

The theory of how to mathematically represent polarisation and Fresnel behaviour is essential to being able to represent the modulator in the same mathematical forms. Having obtained the matrices describing the main components, now the modulator has to be represented too, both in Mueller-Stokes and in Jones formalisms.

### 4.3.1. Mueller-Stokes Formalism

To mathematically describe the modulator, it must be split into parts. To begin with, the first prism can be defined. The active prisms of the modulator function as variable waveplates, meaning that the waveplate Mueller matrix expressed in subsection 4.1.1 can also be used to represent the prism. Vasilescu et al. [2020b] shows that this prism has a linearly varying phase difference along the vertical which follows from Equation 4.33.

$$\Delta\phi_1 = \frac{2\pi}{\lambda}\Delta n(\lambda) \cdot t_1 \tag{4.33}$$

Here, $\lambda$ is the wavelength of the incoming light and $\Delta n = |n_0(\lambda) - n_e(\lambda)|$ is the absolute value of the difference between the ordinary and extraordinary refractive indices. Additionally, $t$ represents the thickness of the prism at the height being considered. The thickness is calculated using $t_1 = d + (h-y)\cdot\tan(\xi)$ with d being the thinnest side length of the prism (the top), h being the height of the prism and y the location along the height. Finally, $\xi$ is the apex angle [Vasilescu et al., 2020b]. This formula is established from the geometry of the prism.

With the phase difference defined, it is possible to apply the general Mueller matrix of a rotated waveplate as it has been established that the prism functions like one. The matrix is given by Equation 4.34 as was also seen in subsection 4.1.1.

$$M = \begin{bmatrix} 1 & 0 & 0 & 0 \\ 0 & c^2 + s^2\cos\Delta\phi & (1-\cos\Delta\phi)cs & s\sin\Delta\phi \\ 0 & (1-\cos\Delta\phi)cs & s^2 + c^2\cos\Delta\phi & -c\sin\phi \\ 0 & -s\sin\Delta\phi & c\sin\Delta\phi & \cos\Delta\phi \end{bmatrix} \tag{4.34}$$

where $c = \cos 2\alpha$, $s = \sin 2\alpha$ and $\alpha$ is now the fast-axis angle with respect to the x-axis [Vasilescu et al., 2020b].

Finally, for the second active prism, a similar process is applied as for prism 1. The phase difference given that the fast-axis is now at $\alpha = \pi/4$, is given by Equation 4.35 which can then be applied into Equation 4.8 again. Here, $t_3 = d + (h-y)\cdot tan\gamma$ as the angle is different compared to prism 1.

$$\Delta\phi_3 = \frac{2\pi}{\lambda}\Delta n(\lambda) \cdot t_3 \tag{4.35}$$

With all Mueller matrices obtained for the entire modulator, the outgoing Stokes vector can be obtained easily for each respective y position and selected wavelength. In order to do this, the method which would have to be applied is a simple multiplication of the Stokes vector for the incident light with the Mueller-Matrices for each prism at each height. The Mueller-Matrix used for each prism is the same as Equation 4.8, but with the

$\Delta\phi$ value corresponding to the prism and height being looked at. Because the phase difference is dependent on the thickness of the prism, and the prism thickness increases as you go down the prism, the matrices for an arbitrary height 'y' for each prism, respectively, are as follows:

$$Prism_1 = \begin{bmatrix} 1 & 0 & 0 & 0 \\ 0 & c_1^2 + s_1^2 \cos\Delta\phi_1(y) & (1-\cos\Delta\phi_1(y))c_1 s_1 & s_1 \sin\Delta\phi_1(y) \\ 0 & (1-\cos\Delta\phi_1(y))c_1 s_1 & s_1^2 + c_1^2 \cos\Delta\phi_1(y) & -c_1 \sin\Delta\phi_1(y) \\ 0 & -s_1 \sin\Delta\phi_1(y) & c_1 \sin\Delta\phi_1(y) & \cos\Delta\phi_1(y) \end{bmatrix} \tag{4.36}$$

$$Prism_3 = \begin{bmatrix} 1 & 0 & 0 & 0 \\ 0 & c_3^2 + s_3^2 \cos\Delta\phi_3(y) & (1-\cos\Delta\phi_3(y))c_3 s_3 & s_3 \sin\Delta\phi_3(y) \\ 0 & (1-\cos\Delta\phi_3(y))c_3 s_3 & s_3^2 + c_3^2 \cos\Delta\phi_3(y) & -c_3 \sin\Delta\phi_3(y) \\ 0 & -s_3 \sin\Delta\phi_3(y) & c_3 \sin\Delta\phi_3(y) & \cos\Delta\phi_3(y) \end{bmatrix} \tag{4.37}$$

A certain degree of error is caused by these matrices due to the assumption that the light ray remains at the same height and continues propagating in the same direction throughout the modulator, but this method is deemed sufficient for an initial investigation given the small angles of incidence on each prism boundary.

With the Fresnel Mueller matrices defined in subsection 4.2.1, and given knowledge of the angles of incidence and refraction angle for the p and the s axes, it is possible to include the matrix into the regular Mueller-Stokes computation for the modulator. The difference between the regular computation and the computation with Fresnel included is simply the multiplication with the respective Mueller matrix representing each Fresnel boundary. The matrix multiplication should, once completed for the entire modulator, result in a form as follows:

$$\mathbf{S} = F_{P_{3_{B_2}}} \cdot Prism_3 \cdot F_{P_{3_{B_1}}} \cdot F_{P_{1_{B_2}}} \cdot Prism_1 \cdot F_{P_{1_{B_1}}} \cdot \mathbf{S_{In}} \tag{4.38}$$

In this equation, $F$ represents the Fresnel matrix, $Prism_{1,2}$ represent the prisms (only the first and third are taken into account in this case, as the second does not have an active role), and $B$ represents the boundary of the prism with 1 meaning the incident, and 2 being the exit boundary. The multiplication is done very simply once the matrices have been defined with all variables. However,there is one additional feature to take into account. The third prism is rotated in terms of fast-axis angle. This means that the matrices are on a different coordinate system when it comes to this prism. To keep the entire equation on the same coordinate system, and therefore get the correct Stokes vector, rotation matrices have to be added to the calculations for the third prism. This results in the following change to the equation as shown in Equation 4.39:

$$\mathbf{S} = R_M(-\theta) \cdot F_{P_{3_{B_2}}} \cdot R_M(\theta) \cdot Prism_3 \cdot R_M(-\theta) \cdot F_{P_{3_{B_1}}} \cdot R_M(\theta) \cdot F_{P_{1_{B_2}}} \cdot Prism_1 \cdot F_{P_{1_{B_1}}} \cdot \mathbf{S_{In}} \tag{4.39}$$

The rotation matrices and prism waveplate matrices are both given in subsection 4.1.1. No rotation matrices are added to $Prism_3$ as the waveplate matrix used already includes them.

### 4.3.2. Jones Formalism

The same method can also be applied for Jones formalism using Jones matrices for the prisms. This method uses Jones matrices of the form

$$M_J = \begin{bmatrix} e^{-i\frac{\Delta\phi}{2}} \cos^2\alpha + e^{i\Delta\phi} \sin^2\alpha & e^{-i\frac{\Delta\phi}{2}} (1 - e^{i\Delta\phi}) \cos^2\alpha \sin^2\alpha \\ e^{-i\frac{\Delta\phi}{2}} (1 - e^{i\Delta\phi}) \cos^2\alpha \sin^2\alpha & e^{-i\frac{\Delta\phi}{2}} \sin^2\alpha + e^{i\Delta\phi} \cos^2\alpha \end{bmatrix} \tag{4.40}$$

where the terms mean the same thing as for Stokes. The effective computation is the same between Stokes and Jones in terms of both obtaining incident and outgoing polarisation states of the light at each height point on the modulator. A certain degree of error is caused by these matrices due to the assumption that the light ray remains at the same height and continues propagating in the same direction throughout the modulator, but this method is deemed sufficient for an initial investigation given the small angles of incidence on each prism boundary. The same limitation caused by the assumption the ray does not change height is also present in the Jones matrices as in the Mueller matrices.

Similarly to the Mueller-Stokes method, applying the Fresnel matrices which have been defined in subsection 4.2.2, the Jones matrices for the modulator are combined in a chain of matrix multiplications as seen in Equation 4.41 but where each matrix is now the Jones variant.

$$\mathbf{J} = R_J(-\theta) \cdot F_{P_{3_{B_2}}} \cdot R_J(\theta) \cdot Prism_3 \cdot R_J(-\theta) \cdot F_{P_{3_{B_1}}} \cdot R_J(\theta) \cdot F_{P_{1_{B_2}}} \cdot Prism_1 \cdot F_{P_{1_{B_1}}} \cdot \mathbf{J_{In}} \tag{4.41}$$

Once again, rotation matrices have to be included as the coordinate system changes when applying the matrices for prism 3. The use of rotation matrices around the Fresnel matrices in this way is based on similar use in other sources such as del Toro Iniesta and Collados [2000]. The rotation matrices are found in subsection 4.1.2.

# 5

# Modelling

In this chapter, the process of modelling the modulator and the Fresnel behaviour is presented. Here, the methods by which the mathematical formulations of chapter 4 are implemented into Python to obtain models in both Jones and Mueller-Stokes forms are discussed, along with the advantages and limitations of each model which was produced. In section 5.1, the general planning for how the models were to be produced is shown. After this, in section 5.2 the Jones form models are presented in more detail, followed by the Stokes equivalents in section 5.3. Finally, the use of a small birefringent approximation is explained as another verification step for the modelling process in section 5.4.

## 5.1. Model Plan

To properly model the modulator in order to observe if fluctuations in the intensity occur even without an analyser, the steps must first be clearly laid out. First of all, the coding language chosen for the modelling would be Python. This is mainly due to the significantly greater experience with the language than other alternatives and the greater availability of support if required. After the language was selected, the preliminary stage of modelling is learning how to model basic components in the Jones and the Mueller-Stokes mathematical forms. After these components are modelled, Fresnel transmission and reflection behaviour has to be modelled as well. Once this has been achieved, it is possible to identify the combination of modelled behaviour which would create the model for each modulator prism in both Jones and Mueller-Stokes. A first iteration of the modulator model can then be created in a 1-dimensional situation followed by a 2-dimensional model to show the behaviour of light at each position in height of the modulator prisms. A flow chart for the steps taken in the process of modelling is shown below in Figure 5.3

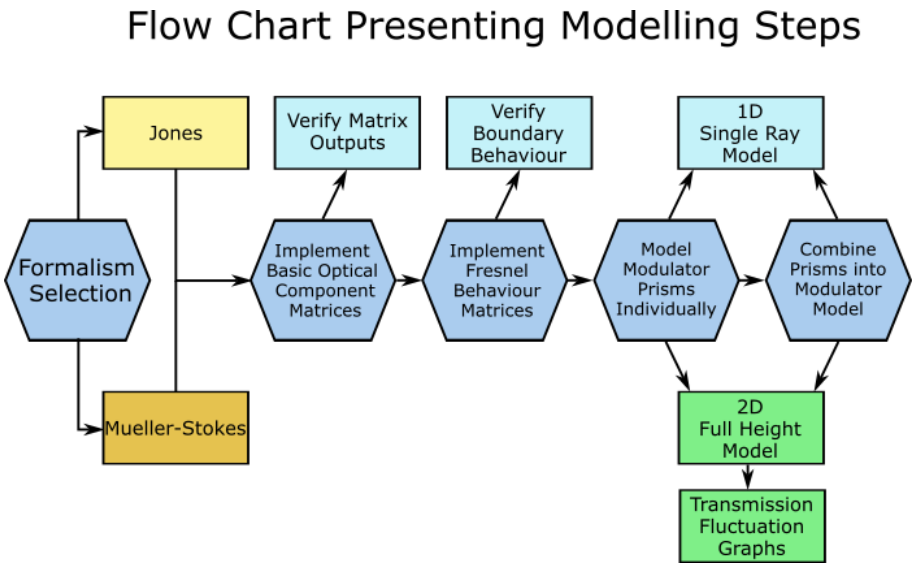


**Figure 5.1:** Flow Chart showcasing the main steps in creating a Python model in either Jones or Mueller-Stokes formalisms.

In Figure 5.3 the flow chart showcases how the general steps are identical no matter which mathematical formalism is selected. The end goal is to reach the green boxes where the model is capable of producing the output transmission across the full height of the modulator.

For learning the basics of modelling in Jones and Mueller-Stokes, all the base polarimetry components were modelled using both forms, starting with linear polarisers and building up to half-waveplates, quarter waveplates and finally general waveplate matrices. For each component modelled, testing was performed using various incident polarisation orientations and observing if the output polarisation states are as expected. After this, combinations of multiple matrices are tested as well to ensure that the combinations also function as anticipated. In the case that the polarisers or waveplates needed to be rotated as well, rotation matrices were modelled in addition to the base components. For maximum flexibility, each element was coded with rotation matrices included to be able to produce the specific Jones or Mueller matrix requested based on an input of required orientation and/or phase angle as needed. This also means that the coordinate system is rotated and then unrotated after each matrix even if two components of the same orientation are placed one after the other. Despite this slight inefficiency in this specific case, the benefit of this method was that the functions to model each component could be used with minimal additional input in any combination and order.

With the commonly used components modelled, the Fresnel matrices are necessary as well before the modulator model can be approached. For this stage, the matrices were coded in Jones and Mueller-Stokes using a combination of Fresnel coefficients and previous Fresnel matrix forms from other sources which could be adapted for use in this project as well. Initially, a preliminary function was created based on the other sources versions of the Fresnel matrices. This preliminary version was used to test simple boundaries where both materials on either side of the boundary were isotropic. Once the reflection and transmission outputs for this simple case were checked, the model was adapted to work for birefringent materials as well. In this next version of the function, a user is able to input the material properties of a birefringent material and an isotropic material, choose whether the ray of light is entering or exiting the birefringent material, and whether the user desires the reflection or the transmission coming from the boundary. In this way, it was possible to test that the model works correctly for birefringent boundaries by comparing the percentage transmission and reflection to the known values from databases. Additionally, this function can have a specified orientation of the boundary specific coordinate system and of the ray angle of incidence at the boundary. For the angle of incidence, it is also possible to have different incidence angles for the fast and slow-axis rays, which is useful due to birefringent materials resulting in a separation of a single ray into two..

With the functions established for both the base components and Fresnel phenomena at birefringent boundaries, the modulator can be identified to be comprised of 2 prisms which, in turn, are essentially two Fresnel boundaries with a waveplate in between. It is also important to note that the second active prism has a fast-axis orientation at 45° while the first has the orientation at 0°, which is why rotation matrices were introduced into each function. Given that no additional functions are required at this point, it now becomes possible to code a simple one-dimensional version of each prism.

Finally, with the prisms modelled, the prisms can be combined to produce the modulator model. The code is then adapted to work in a two-dimensional case. This model can produce the output polarisation state of the light once it has passed through the modulator based on any incident polarisation state specified by the user. From here, the code is then adapted to also compute the intensity of the light output compared to the input and plot the variation of intensity along the entire height of the modulator.

## 5.2. Jones Model

In the previous section, section 5.1, the general steps taken in the Jones model are already introduced. Here, instead, the specific details of how the model actually works are given. The model and tests performed are explained starting with the structure of the code and how the different functions are combined. After this, the method by which the polarisation output is transformed into an intensity are also discussed, and the variations of the model are shown with their respective advantages and disadvantages.

### **5.2.1.** Model Structure and Components

When it comes to the overarching structure of the Jones models, there are 2 main code files which are used to produce the final version of the model. The first of the files is the list of base optical components as functions, each represented in Jones matrix form. Within the list are the matrices for linear polarisers, general waveplate matrices and Fresnel matrices. The second file is where these matrices are brought together to form the modulator and produce the results with which to analyse the performance of the modulator against the experimental results, both previously obtained, and to be obtained later in the thesis.

**Optical Component Functions and Testing**
Based on the theory from subsection 4.1.2, the functions were created for each component using the same matrices presented there. Each component was modelled using the rotatable form of the Jones matrix by including Jones rotation matrices within the function to both rotate and de-rotate the coordinate system when these were used.

For the linear polarisers, the function is designed to take the desired orientation as the input. The function then uses the standard horizontal linear polariser matrix and combines it with a rotation and de-rotation matrix on either side to produce the output of a 'rotatable' linear polariser matrix. This function was then tested by simply observing the polarisation output provided when different input linear polarisation Jones vectors were combined with the Jones matrix.

For the general waveplate function, two different methods are applied to ensure easy verification. The first method was performed in the same way as the linear polariser. Here, the matrix for an arbitrary waveplate is used with a horizontal orientation. The same rotation matrices are added to allow for the orientation to then be modified at will. As inputs to the function, the phase angle and the desired orientation can be specified to give a final Jones matrix for the component. The second method uses the same inputs, but hard-codes the complete matrix for a rotatable waveplate instead. This was done to ensure the matrix multiplications within the functions work as intended by comparing them to the manually calculated matrix.

The functions were tested using simple and easily verifiable cases such as implementing a known incident Jones vector and observing the output Jones vector for various combinations of the components. Obvious things to test included linear polarised light entering a parallel, perpendicular or a 45° oriented linear polariser, testing quarter and half-waveplates, and then checking if combinations of linear polarisers and waveplates would result in an expected output Jones vector and intensity.

**Simple Modulator**
Given the implementation of the functions for linear polarisers and waveplates, it is now possible to recreate a simple model of the modulator which is being investigated in Jones formalism. For this model, the only parts of the modulator being considered are the 2 active prisms which in the complete modulator design would be prisms 1 and 3. The central structural prism will be neglected as it neither affects the light polarisation itself, nor the pattern of the intensity output in any significant way.

The first part of the model is the definition of all the unchanging specifications of the system. Here, the incident light polarisation state is manually chosen by giving an angle in degrees for the 'light polarisation angle' variable. This variable is then used to create a Jones vector of the desired linear polarisation. If circular polarisation is desired instead, an alternative vector is included which can be used instead and modified easily for right hand and left hand circular light. The wavelength of the light entering the system is also defined here. As a further simplification, only one single wavelength would be considered at a time to focus the investigation.

After the incident light has been defined, basic information regarding the prism shapes is included. These are taken from Figure 3.2, in which the prisms' shape specifications are given. The overall height of the prisms is set to 'h = 20mm' and the thickness of the 'rectangular' part is set to 'd = 1mm'. Additionally, the apex angles are also included as variables defined as 'apex_p1' and 'apex_p3' each set to 2.6° and 1.8° respectively. Finally, the fast-axis angle of each prism is also included as variables, with prims 1 oriented at 0° and prism 3 oriented at 45°.

Once the preliminary variables have been established, along with the input Jones vector, the next stage is defining the material property of the Magnesium Fluoride. This is performed using Equation 5.1 and Equation 5.2 taken from the refractive index database[1].

$$n_o = \sqrt{\left(\frac{0.48761\lambda^2}{\lambda^2 - 0.043384^2} + \frac{0.39857\lambda^2}{\lambda^2 - 0.094614^2} + \frac{2.3120\lambda^2}{\lambda^2 - 23.794^2} + 1\right)} \tag{5.1}$$

$$n_e = \sqrt{\left(\frac{0.41343\lambda^2}{\lambda^2 - 0.036843^2} + \frac{0.50545\lambda^2}{\lambda^2 - 0.090762^2} + \frac{2.4905\lambda^2}{\lambda^2 - 23.772^2} + 1\right)} \tag{5.2}$$

[1] URL: `https://refractiveindex.info/?shelf=main&book=MgF2&page=Zheng-o-21C`, options for both $n_o$ and $n_e$ were used, last accessed 05-02-2025

This results in the refractive indices of the fast and slow axes of the prisms being set to approximately 1.379 and 1.391 respectively depending on the wavelength selected, with $n_p = n_o$ and $n_s = n_e$. For the 'material' the ray is in before and after each prism, air is used, hence a refractive index of 'n_air = 1'.

For the 2 prisms being considered, which are prism 1 and 3 in the complete modulator, each can be considered as a waveplate with phase shift dictated by the thickness of the prisms at the chosen height and the material properties of the prism itself. To compute the phase shift for each prism at a specified height, Equation 4.33 and Equation 4.35 are used. These formulas are again stated below in Equation 5.3 and Equation 5.4 for clarity.

$$\Delta\phi_1 = \frac{2\pi}{\lambda}\Delta n(\lambda) \cdot t_1 \tag{5.3}$$

$$\Delta\phi_3 = \frac{2\pi}{\lambda}\Delta n(\lambda) \cdot t_3 \tag{5.4}$$

With the refractive indices already calculated, the total thickness at the specified height must still be calculated for each prism. To do this, the prism can be split into a rectangular part and a right-angled triangle part. The rectangular thickness is already known as 1mm, and the thickness remaining can be easily calculated given the height and the apex angle being known for the right angled triangle formed when the rectangular part is removed from the calculation.

The next stage of the model is obtaining the prism waveplate Jones matrices. Here, the functions from the previously discussed 'base optical components' file are reintroduced. The rotatable waveplate function is used which produces the matrix form for each prism. As input parameters to the function, the specific orientation of the prism fast-axis is used along with the phase shift obtained by the respective equation for the prism.

Finally, the multiplication of the waveplates and the input Jones vector is performed to give the output Jones vector at the other end of the modulator. This is done by taking the dot product of the Jones vector with the first prism matrix and then the third prism matrix in the form:

$$\mathbf{J_{out}} = Prism_3 \cdot Prism_1 \cdot \mathbf{J_{In}}$$

As an additional step towards the automation of the process, the entire code after the definition of the main variables was then integrated into a for loop which transforms the model from a one-dimensional model to a two-dimensional model by looping the calculations across all different heights in steps of 0.01 mm. From here the Jones vector outputs can be obtained for all heights easily for this simple case.

**Modulator with Fresnel**

When it comes to modelling the boundaries for Fresnel behaviour, the functions required take on a new level of complexity. For Fresnel behaviour to be integrated into the Python code the simple modulator code has to be overhauled to calculate all of the necessary input parameters for the Fresnel matrix functions. Some elements can be maintained and kept the same as in the previous iteration of the model, meaning the overall layout and order of operations is similar; however, Fresnel adds numerous extra parameters. Fresnel relies not only on the refractive indices and thickness of the prisms, but also on the precise angles of incidence at each boundary. Furthermore, Fresnel introduces the additional issue of there being both reflections and transmissions at each boundary. This not only affects the affects the polarisation state of the light passing through the system, but also means that the model must be able to treat both the pure transmissions, as well as the various reflections which could occur at any one of the 4 boundaries.

In this version of the model, similarly to the simple modulator mode, the first stage is defining all of the base variables. The Jones input vector, the variables related to the prism shapes and orientations, the refractive indices and the phase shift calculations all remain the same as in the simple model. In addition to these variables, now the ray angles of incidence and refraction must be calculated as well.

To perform these calculations, the light is treated as 2 distinct rays, one which interacts with the fast-axis refractive index, and one which interacts with the slow-axis refractive index. This separation of the ray into its fast and slow-axis components is done for both prisms to obtain an average refraction angle. Treating the actual splitting of the beam was considered beyond the scope of the model as the purpose of the model was to demonstrate the intensity fluctuations and investigate them rather than to precisely model the exact beam paths through the material. Furthermore, the refractive indices were considered similar enough that the rays would not be separating from each other to a significant enough degree.

The process of calculating each angle of incidence is done by simply using Snell's law for each boundary. It is assumed that the angle of incidence at the first prism entry is 0° as this is the ideal position of the modulator. Despite this, the code is written to have flexibility and be relatively simple to alter if this is changed at any point.

Following the angles of incidence and refraction calculations, the Fresnel and waveplate functions are finally able to be used. To begin with, the Fresnel functions will be talked about in more detail. Unlike the waveplate functions, the Fresnel functions depend on not only the orientation of the fast-axis coordinate system, but also on the material properties of both the medium being entered and the medium being exited. The function also has to be able to account for whether the boundary is an entrance or exit boundary to the birefringent material, if the desired output is the transmitted or reflected ray, and if there is any angle of incidence.

The theory used in the creation of the Fresnel function and the Jones matrix associated to it is based on the Fresnel coefficients and Jones matrices introduced in subsection 4.2.2. For the application to birefringence, the coefficients are used with the simplification that the ray can be split into two independent axes and, therefore, the refractive indices can be chosen based on which axis interacts with said term in the matrix. This results in the matrices for transmission and reflection being formed with the following formulas for the case of a ray entering a birefringent material:

$$r_p = \frac{n_p \cdot \cos\sigma_{i_p} - n_1 \cdot \cos\sigma_{r_p}}{n_p \cdot \cos\sigma_{i_p} + n_1 \cdot \cos\sigma_{r_p}} \tag{5.5}$$

$$r_s = \frac{n_1 \cdot \cos\sigma_{i_s} - n_s \cdot \cos\sigma_{r_s}}{n_1 \cdot \cos\sigma_{i_s} + n_s \cdot \cos\sigma_{r_s}} \tag{5.6}$$

$$t_p = \frac{2 \cdot n_1 \cdot \cos\sigma_{i_p}}{n_p \cdot \cos\sigma_{i_p} + n_1 \cdot \cos\sigma_{r_p}} \tag{5.7}$$

$$t_s = \frac{2 \cdot n_1 \cdot \cos\sigma_{i_s}}{n_1 \cdot \cos\sigma_{i_s} + n_s \cdot \cos\sigma_{r_s}} \tag{5.8}$$

In the case that the ray is instead exiting the birefringent material, the locations of the refractive indices are inverted within each equation. In these formulas, $n_p$ and $n_s$ correspond to $n_o$ and $n_e$ respectively. The additional refractive index, $n_1$ is the refractive index of the isotropic material which forms the boundary with the prism. In the case of the specific prisms used in the thesis, this refractive index is equal to to refractive index of air and is therefore equal to 1.

From these formulas, a reflection matrix and a transmission matrix can be formed based on the theory from subsection 4.2.2 which are repeated in Equation 5.9 and again in Equation 5.10 below for clarity.

$$\mathbf{J_r} = \begin{bmatrix} -r_p & 0 \\ 0 & r_s \end{bmatrix} \tag{5.9}$$

$$\mathbf{J_t} = \begin{bmatrix} t_p & 0 \\ 0 & t_s \end{bmatrix} \tag{5.10}$$

In the parameters of the function, it can be specified both whether to use the formulas for entering or exiting the birefringent material and which of the two matrices are desired as well.

Testing the function to ensure they produced the correct results was done in two ways. The first was to test the function as if there is only one boundary and observe both the coefficient results and the resulting intensity in reflection and transmission. This test can easily be verified with the same database as was used for the refractive indices [2].

The second method was to combine 2 boundaries, giving both entry and exit Fresnel matrices, and to ensure that the sum of the transmission output percentage after both boundaries, with the reflection percentages of each individual boundary still gave the full 100% of all light in the input. As the light entering the second boundary is already reduced by the interaction with the first boundary, the code should be able to calculate the reflection and overall transmission while taking this into account. If the total reflected and transmitted gives the total input, then this calculation is likely performed correctly.

[2] See footnote 1.

Now that both the Fresnel matrices can be obtained for each boundary and the waveplate matrices are also available like previously in the simple modulator model, it would already be possible to have a final model for the entire modulator. Simply putting all the functions in together, however, can cause unnecessary confusion and may result in errors when trying to change between different ray paths (such as transmission through the first 3 boundaries and reflection off the 4th.

For the sake of clarity and simplicity when working with both reflections and transmission, new functions are defined. The new functions which are introduced combine the Jones matrix functions to compress them into functions for entire prisms instead. The new functions are given inputs in the form of all the inputs needed for the functions embedded within. Each of these new functions represents a possible ray path through a single prism which can be looked at individually.

The paths which were most important, and therefore were the ones created, are represented in Figure 5.2:

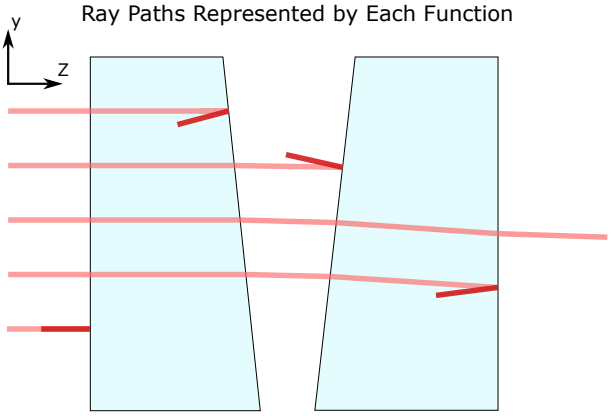


**Figure 5.2:** Ray paths which are represented by the different functions. Height location of the ray is only different for clarity, in the code all paths originate from the same incident ray.

All of the different paths were considered as they are important to the preliminary verification of the model where the sum of the overall transmitted light and all of these different reflections must add up to the original incident light. Furthermore, the creation of such functions can be used in future research to easily investigate the intensity fluctuations of the reflected rays, or the outputs from multiple internal reflections.

Additional internal reflections ended up being neglected for this study as the general percentage of light which reflects off any given boundary is between 2-3% often around 2.5% at the wavelengths which are investigated in this thesis. With just two reflections occurring, the remaining light is already so greatly reduced it was expected to have a very limited effect on the transmission pattern.

Once the functions for each prism exist, the output polarisation is calculated in the same 'for' loop across the height of the prism as was referred to in the simple modulator case. As the most interesting result is obtained when the light transmits through the entire modulator, this is the case which will be used as an example of how the final polarisation state is obtained.

To calculate the final polarisation state, the functions designed to represent transmission through prisms 1 and 3 are taken and the cross product is performed. In essence:

$$\mathbf{J_{out}} = Prism_3 \cdot Prism_1 \cdot \mathbf{J_{In}} \tag{5.11}$$

If the Prism 1 and Prism 3 calculations were to be separated to show the entire calculation in terms of each individual matrix being included, it would look as follows:

$$\mathbf{J_{out}} = R_J(-\theta) \cdot F_{P_{3_{B_2}}} \cdot R_J(\theta) \cdot R_J(-\theta) \cdot Prism_3 \cdot R_J(\theta) \cdot R_J(-\theta) \cdot F_{P_{3_{B_1}}} \cdot R_J(\theta) \cdot F_{P_{1_{B_2}}} \cdot Prism_1 \cdot F_{P_{1_{B_1}}} \cdot \mathbf{J_{In}} \tag{5.12}$$

where the R's represent rotation matrices, the F's represent the corresponding Fresnel matrices and $Prism_1$ along with $Prism_3$ represent the prism waveplate matrices. This calculation is performed for each height step to produce the Jones vector related to the ray transmitted at that height.

There existed an alternative version which was investigated where the Fresnel matrices did not include rotation matrices. This was observed in Gu and Yeh [1999]. As the paper had similar calculations to those performed in this thesis but with the distinct difference in how the rotation matrices were introduced, there was uncertainty on which version produced the more accurate results. The results of this alternative method did not produce fluctuations consistent with the expected results nor with the original observations from experiments. The specific results of this method are included briefly in subsection 5.2.4.

### 5.2.2. Obtaining Intensity

The models represented in subsection 5.2.1 so far are capable of obtaining the polarisation states of all the different points along the height of the modulator. To compare to experimental results such as those from section 3.2, it is now necessary to calculate the intensity of the light transmitted in order to plot the fluctuations produced by the model and, finally, demonstrate that the fluctuations are explainable mathematically with Fresnel phenomena.

**Calculating Intensity**

Computing intensity from a Jones vector is usually very simple. This is also true in the case of the simple modulator model which does not include any Fresnel phenomena. In subsection 4.1.2, the normal method of calculating the intensity is shown. This method is also applicable to the first model in the exact same way. At each height step, the absolute value of the terms in the Jones vector is squared and then summed to obtain the total intensity of the ray. Through the fact that the incident light is normalised in all of the models, this intensity is also equal to the transmission of the light. Of course, in the case of the simple model with no Fresnel phenomena, the intensity output is identical to the input intensity as there is no loss considered when the light passes through the prism.

The greater difficulty stems from when Fresnel behaviour is included into the model. In this case, calculating the intensity becomes a far more complicated issue. To explain why this is the case, it is first required that the additional steps to the calculation, which are required for the inclusion of Fresnel, are introduced. To begin with, plotting the intensity for the case of a single boundary still a relatively simple task. At each boundary, the energy must be conserved as the light passes from one material to the next. According to Hecht [2017]this results in the need to apply a 'correcting factor'. The source of this factor stems from two phenomena which affect the energy across the boundary. The first is the change in refractive indices. As the refractive indices change, the energy is transmitted at a different speed on either side of the boundary. The second effect is the change in the cross-sectional area of the incident and refracted beams. To maintain the conservation of energy on either side of the boundary, the total energy flowing into the boundary per unit of time must also be equal to the energy flowing out. Hence, the correction factor is material and angle of incidence dependent, with a different factor for each axis of a birefringent material. This factor also has to be applied regardless of whether the ray is being transmitted or reflected as energy must be conserved in both cases [Hecht, 2017].

From Hecht [2017], the general form of these correction factors is as given in Equation 5.13.

$$T = \left(\frac{n_2 \cos\sigma_r}{n_1 \cos\sigma_i}\right) t^2 \tag{5.13}$$

where T is the transmission percentage intensity, t is the Jones vector component, $\sigma_i$ is the angle of incidence, $\sigma_r$ is the angle of refraction and $n_1$ and $n_2$ are the refractive indices of the first material and second material on either side of the specific boundary respectively. Adapting this to a birefringent case results in each component having its own formula as the birefringent material means there are different refractive indices and refraction angles along each axis.

$$T_s = \left(\frac{n_{2_s} \cos\sigma_{r_s}}{n_{1_s} \cos\sigma_{i_s}}\right) t_s^2 \tag{5.14}$$

$$T_p = \left(\frac{n_{2_p} \cos\sigma_{r_p}}{n_{1_p} \cos\sigma_{i_p}}\right) t_p^2 \tag{5.15}$$

The same formula can also technically be applied for calculating the reflection percentage intensity using the reflection Jones vector, however, the terms all cancel out. The angle of 'refraction' is actually the angle of reflection and is the same as the angle of incidence as both are measured with respect to the normal. Additionally, the refractive index of the second material is the same as the first as no actual material change occurs.

Building up to a full prism adds an additional level to the calculation of the final intensity. Instead of just one boundary, now there are two which both require considerations to be made in the form of correction factors.

Once again, the correction factors must be added for each boundary ($B$) to account for the conservation of energy between the initial incident Jones vector and the output Jones vector. These correction factors are calculated for each component of the output Jones vector and multiplied with the respective term in the following calculations:

$$T_s = \left(\frac{n_{2_s}\cos\sigma_{r_{B1_s}}}{n_{1_s}\cos\sigma_{i_{B1_s}}}\right)\left(\frac{n_{1_s}\cos\sigma_{r_{B2_s}}}{n_{2_s}\cos\sigma_{i_{B2_s}}}\right)t_s^2 \tag{5.16}$$

$$T_p = \left(\frac{n_{2_p}\cos\sigma_{r_{B1_p}}}{n_{1_p}\cos\sigma_{i_{B1_p}}}\right)\left(\frac{n_{1_p}\cos\sigma_{r_{B2_p}}}{n_{2_p}\cos\sigma_{i_{B2_p}}}\right)t_p^2 \tag{5.17}$$

It can be seen that, because the material being entered and the material being exited are one and the same, the refractive index terms cancel when the ray enters and then also exits the birefringent material. The final version of the transmission calculation is then simplified to only require the angles of incidence and refraction at each boundary.

$$T_s = \left(\frac{\cos\sigma_{r_{B1_s}}}{\cos\sigma_{i_{B1_s}}}\right)\left(\frac{\cos\sigma_{r_{B2_s}}}{\cos\sigma_{i_{B2_s}}}\right)t_s^2 \tag{5.18}$$

$$T_p = \left(\frac{\cos\sigma_{r_{B1_p}}}{\cos\sigma_{i_{B1_p}}}\right)\left(\frac{\cos\sigma_{r_{B2_p}}}{\cos\sigma_{i_{B2_p}}}\right)t_p^2 \tag{5.19}$$

For reflection the calculation for the first boundary remains trivial. On the other hand, for the subsequent boundaries it has to be adapted slightly to take into consideration the transmission through the boundaries prior to the reflection taking place. The formulas for the reflection cases are shown in Appendix A.

This general method to obtaining the intensity can be applied exactly the same for any prism. This therefore does not yet explain the issue with the correction factors or why they cause problems with the model. This is because the main difficulty occurs when the two prisms are combined. If the simplified formula for the 4 boundaries was to be written out, it would look like shown in Equation 5.20 and Equation 5.21, which is an extension of Equation 5.18 and Equation 5.19 to account for the two added boundaries.

$$T_s = \left(\frac{\cos\sigma_{r_{B1_s}}}{\cos\sigma_{i_{B1_s}}}\right)\left(\frac{\cos\sigma_{r_{B2_s}}}{\cos\sigma_{i_{B2_s}}}\right)\left(\frac{\cos\sigma_{r_{B3_s}}}{\cos\sigma_{i_{B3_s}}}\right)\left(\frac{\cos\sigma_{r_{B4_s}}}{\cos\sigma_{i_{B4_s}}}\right)t_s^2 \tag{5.20}$$

$$T_p = \left(\frac{\cos\sigma_{r_{B1_p}}}{\cos\sigma_{i_{B1_p}}}\right)\left(\frac{\cos\sigma_{r_{B2_p}}}{\cos\sigma_{i_{B2_p}}}\right)\left(\frac{\cos\sigma_{r_{B3_p}}}{\cos\sigma_{i_{B3_p}}}\right)\left(\frac{\cos\sigma_{r_{B4_p}}}{\cos\sigma_{i_{B4_p}}}\right)t_p^2 \tag{5.21}$$

It is important to note again that all of the terms are still aligned along the same coordinate system as the Jones vector at this stage. In the case of the real modulator prisms, this suddenly causes a problem.

The prisms in the case of the actual modulator design have different coordinate systems in terms of their fast-axis orientation. So far, when dealing with this fact in the Jones formalism, rotation matrices easily changed the coordinate system to align to the prism, and then back to the desired coordinate system. When it comes to the correction factors, however, there are no rotation calculations which can be used to adapt them as needed. To further clarify the issue, an example Jones output vector will be considered that is aligned to the first prism, which will be referred to as the x-y coordinate system. The output Jones vector has to have correction factors applied on both its x component an y component based on what occurred to these specific components at each boundary the ray passed through. This means that the correction factors have to also be definable in those same axes. The first prism, being oriented in the same x-y coordinate system, is trivial as the refractive indices align precisely with the x and y axes. The third prism, however, is aligned along a 45° orientation. The refractive indices of prism 3 cannot be defined along the same x-y axes as there is no knowledge on how the material behaves on axes not aligned with the fast and slow axes.

To try to approximate the refractive indices along these undefined axes, a few initial attempts were made where an average refractive index was taken. It was assumed that the refractive indices on the fast and slow axes act in equal measure because the x axis is half way between them. This method, however, results in a complete negation of the birefringent nature of the prism. By taking the average of $n_p$ and $n_s$ to obtain $n_x$ and $n_y$, this results in a situation where $n_x = n_y$, thus resulting in the formulas behaving as if prism 3 is isotropic. As this simplification ends up completely neglecting the birefringence of prism 3, a different method of applying the correction factors must be devised.

When it came to devising such a method, three main requirements were considered in what the objective would be for the 'ideal' solution. These requirements are listed here:

1. The method must calculate the correct output polarisation state
2. The method must calculate the correct intensities for each reflection and transmission
3. The method must be able to produce a full Jones matrix for the entire modulator so that it can be transformed into a Stokes matrix

The first two requirements are necessary to be able to produce the results which are required to demonstrate Fresnel behaviour and the fluctuations which the phenomena cause. The third requirement, on the other hand, is desired as it would enable an initial Mueller-Stokes model to be created which future Mueller-Stokes models can be compared to. As the Jones method cannot treat unpolarised or partially polarised light, and the spectropolarimetry method is intended for full-Stokes spectropolarimetry, having this full Jones matrix for the modulator would be a valuable step towards ensuring a proper Stokes model can be produced later.

For the first and third requirements, the existing model is more than capable. When including the intensity, the model suddenly is no longer viable in its current state. Two additional possible alternatives were conceived after attempting various tests and experimental changes to see if the solutions could be approximated.

**Correction Factor Matrix Method**

The first of the new methods was to put the correction factors within the matrix calculation. Therefore, at the point when the coordinate system changes, the intensity corrections would already be implemented and they would be able to match with each new coordinate system specifically. In this situation, the correction factors are effectively implemented as their own matrices into the Jones formula to produce Equation 5.22.

$$\begin{aligned}\mathbf{J} = R_J(-\theta)\cdot\ C_{P_3}\cdot\ R_J(\theta)\cdot\ R_J(-\theta)\cdot\ F_{P_{3_{B_2}}}\ \cdot\ R_J(\theta)\cdot\ R_J(-\theta)\cdot\ Prism_3\cdot\ R_J(\theta)\cdot \\ R_J(-\theta)\cdot\ F_{P_{3_{B_1}}}\ \cdot\ R_J(\theta)\cdot\ C_{P_1}\cdot\ F_{P_{1_{B_2}}}\ \cdot\ Prism_1\cdot\ F_{P_{1_{B_1}}}\ \cdot\ \mathbf{J_{In}}\end{aligned} \tag{5.22}$$

The correction factor matrices were generated simply by creating a diagonal matrix with the square root of the correction factor for the x-axis in the top left, and the y-axis in the bottom right such that the Jones vector components are multiplied with their corresponding correction and not the other.

Therefore, in Equation 5.22, the matrices for $C_{P_1}$ and $C_{P_3}$ are as shown in Equation 5.23 and Equation 5.24.

$$C_{P_1} = \begin{bmatrix} \sqrt{\left(\frac{\cos\sigma_{r_{B1_p}}}{\cos\sigma_{i_{B1_p}}}\right)\left(\frac{\cos\sigma_{r_{B2_p}}}{\cos\sigma_{i_{B2_p}}}\right)} & 0 \\ 0 & \sqrt{\left(\frac{\cos\sigma_{r_{B1_s}}}{\cos\sigma_{i_{B1_s}}}\right)\left(\frac{\cos\sigma_{r_{B2_s}}}{\cos\sigma_{i_{B2_s}}}\right)} \end{bmatrix} \tag{5.23}$$

$$C_{P_3} = \begin{bmatrix} \sqrt{\left(\frac{\cos\sigma_{r_{B3_p}}}{\cos\sigma_{i_{B3_p}}}\right)\left(\frac{\cos\sigma_{r_{B4_p}}}{\cos\sigma_{i_{B4_p}}}\right)} & 0 \\ 0 & \sqrt{\left(\frac{\cos\sigma_{r_{B3_s}}}{\cos\sigma_{i_{B3_s}}}\right)\left(\frac{\cos\sigma_{r_{B4_s}}}{\cos\sigma_{i_{B4_s}}}\right)} \end{bmatrix} \tag{5.24}$$

This method is able to calculate an output Jones vector using a single 'modulator' matrix if all of the different Jones matrices are combined. Similarly, it is also able to calculate the intensity correctly for each ray. This was determined and checked both on smaller scale models of single prisms, and with the sums of the reflections and transmission to ensure that it all accounted for 100% of the light. As the reflection percentage at each boundary can easily be compared to the refractive index database[3], it is clear when the transmission is also being given correctly from the output Jones vector. This change to the model therefore evidently meets the criteria for requirements 2 and 3. Requirement 1 is not able to be met with this form. Despite 2 of the criteria being met, the first criterion is now no longer able to be achieved as the correction factors are asymmetric. This refers to the fact that they affect the terms of the Jones matrix differently. For a very simple explanation of why this causes problems in obtaining the correct polarisation state, take an un-normalised 45° oriented Jones vector as follows: $\mathbf{J} = \begin{bmatrix} 1 \\ 1 \end{bmatrix}$, and perform corresponding corrections to each term, leading to $\mathbf{J} = \begin{bmatrix} 1\cdot C_1 \\ 1\cdot C_2 \end{bmatrix}$, it

[3] See footnote 1.

becomes clear that the orientation of the vector after the addition of the corrections is no longer at 45°. Because of this, the first requirement becomes unobtainable from this model.

**Separation Model**
The next version of the model which was conceived was to split the modulator into two separate prisms and calculate the intensity step by step. To begin with, the first prism is considered by itself. The same Jones calculation is performed where the Fresnel boundaries and the prism waveplate matrices are calculated and multiplied. The Jones output of the first prism is then computed and the intensity of this specific vector is calculated with the correction factors.

At this stage, the polarisation orientation and the relative intensity between the input and output Jones vectors are known. The Jones vector is then normalised again to an intensity of 1, and is put as input to the third prism. The calculations are performed again, but now for the third prism, including coordinate system changes to apply the correction factors correctly. Once a Jones output from this prism is obtained, the orientation of the output polarisation state will be the correct orientation as if the entire modulator had been used. The intensity, however, is still relative to a normalised vector input.

Given the relative intensity between the input and output of each prism, it is now possible to also calculate the intensity at the end of the third prism with respect to the original input vector. The calculation is simple as each input vector is normalised to an intensity of 1, therefore each output vector intensity is a percentage intensity of the input. Knowing, as an example, that 95% of light was transmitted through the first prism and 93% was transmitted through the second, leads to (95%·93%) 0.8835% of light passing through from one end to the other. This method was verified compared to the other two model variants and was shown to give both the correct intensity and the correct Jones vector orientation at the output of the modulator. This therefore makes this model able to meet criteria for both requirements 1 and 2.

With 3 different models, each capable of meeting 2 requirement (1 and 3, 2 and 3, and 1 and 2 respectively), it appeared as though an optimal solution should be obtainable with a little more study. Substantially more time was dedicated to this task in addition to a further literature review in the hopes that there was some small factor which could be used to solve for all 3 requirements. During this literature review, methods were also searched for approximating the refractive index instead, but given the scope and timeline of the thesis the methods would have proven too complex and time-intensive to properly study, understand, and integrate into every function and Python file.

A few new discoveries were made during this review such as the alternative way in which Fresnel matrices were combined with rotation matrices as described briefly at the end of subsection 5.2.1, as well as the small birefringent approximation which is discussed further in section 5.4.

Despite the time invested into trying to combine these methods or find new formulas which would allow for the 3 requirements to be achieved at the same time, in the end no such solution was found within the time frame which could be allocated to this task. Because of this, the requirements had to be labelled as to whether they are more or less important overall.

To obtain a transmission fluctuation graph which can be compared to the experimental results, the most important model output is the intensity itself. After this, to make sure that the model can easily be verified and modified as needed, the second most important requirement is the polarisation state of the light. This results in the last requirement of having the modulator represented as one single matrix as the least critical to progressing towards the goal. Hence, the model version which is primarily used to obtain the results is the separation model.

### **5.2.3.** Model Overview

As a summary, to bring all of the previously discussed steps of the model creation together, this subsection will provide a more concise overview of the final Jones Python model, along with the main verification and testing performed during the model's creation, and the limitations which this model faces.

**Final Model Versions**
First of all, the different model versions in Jones formalism are presented in Table 5.1 along with the capabilities of each model and their limitations regarding the requirements which have been set.

Based on the success of the separation model in both providing the correct output polarisation state and the correct intensity output, this became the main model version which was focussed on.

**Table 5.1:** Table summarising whether the models can or cannot achieve the requirements set at the beginning of model generation.

| | Original Model | Correction Factor Matrix Model | Separation Model |
|---|---|---|---|
| Correct Output Polarisation State | | | |
| Correct Intensity Output | | | |
| Modulator Representable as Single Matrix | | | |

**Model Flow Chart**

To describe how the separation model works, a flowchart is created where the various functions and links between them can be seen. In the flowchart, Figure 5.3, the main elements of the separation model are shown along with the primary interactions between the different steps.

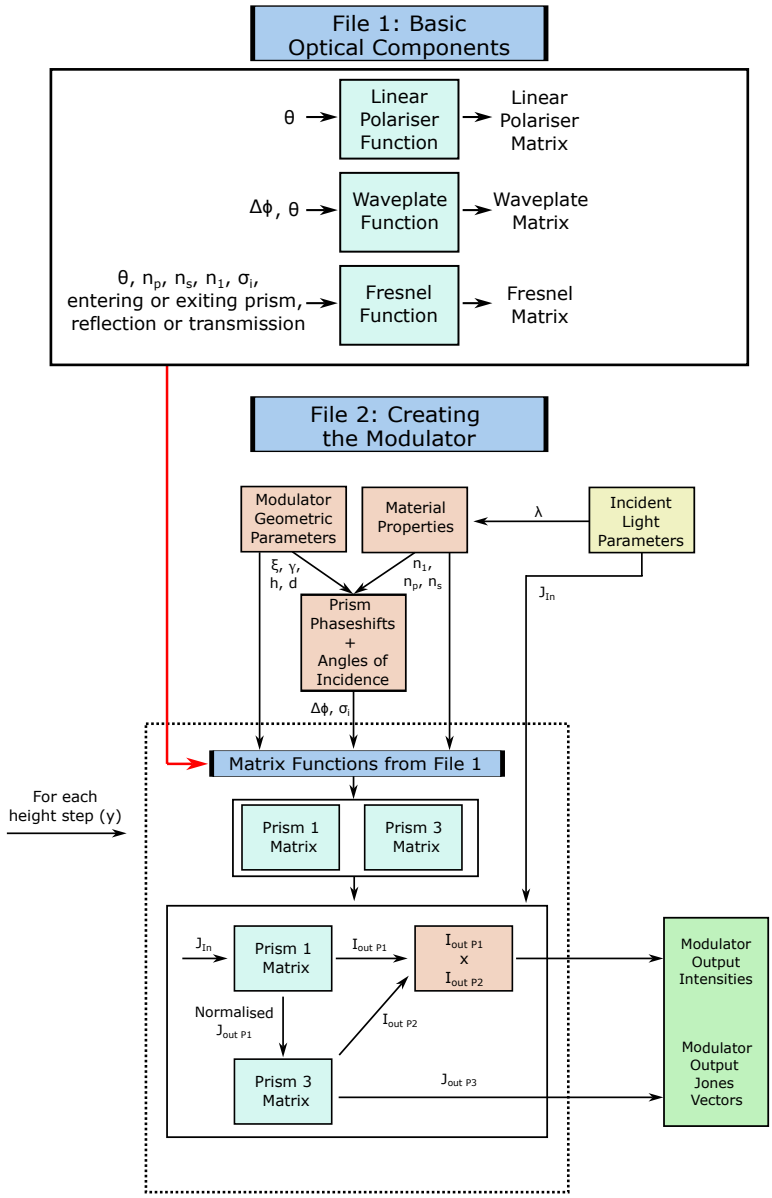


**Figure 5.3:** Flowchart showcasing the main steps and interactions of the Separation model used as the final version of the Jones Python model.

**Jones Model Initial Verification and Testing Summary**
While verification tests which were performed during the creation of the model have already been discussed throughout the methodology in subsection 5.2.1 and subsection 5.2.2, the main tests which were performed during the creation of the Jones model are summarised in Table 5.2 for clarity. The specific cases and results will not be provided, but rather the conclusions of the tests. Specifically, which outputs were primarily observed and whether the outputs which were produced performed as expected.

**Table 5.2:** Table summarising whether the models can or cannot achieve the requirements set at the beginning of model generation.

| Tested Parts | Observations |
|---|---|
| Linear polariser matrices with various orientations | Jones vector outputs were oriented correctly. Intensity loss corresponded to expectations. |
| Waveplate matrices for half and quarter waveplates | Half waveplate and Quarter waveplates working as expected based on incident Jones vector and waveplate orientation. |
| Combination of components (Linear polariser + half/quarter waveplate) | Common combinations of components tested. Linear polariser and half/quarter waveplate combinations gave expected outputs. |
| Fresnel Matrix for isotropic materials | Transmission and reflection intensities were as expected for all cases. |
| Fresnel matrix for birefringent material | Transmission and reflection intensities were as expected for each axis for all cases. |
| 2 Fresnel boundaries back to back | Final transmission intensity and each boundary reflection intensity returned the expected values. |
| Prism 1 on its own | No fluctuations were observed as expected. |
| Prism 3 on its own | No fluctuations were observed as expected. |
| Simple Modulator with no Fresnel behaviour | No fluctuations were observed as expected. |
| Cross-verification of different final model versions | Outputs of each version of the model were compared. E.g. original model and separation model should give the same Jones vector. Results matched on expected outputs. |

If any of these tests produced results which did not follow expectations, it would be a clear sign that the matrices were not being produced correctly or that the multiplications were being performed wrong. Once the matrices were verified, it was necessary to check if the fluctuations which are being investigated also occur with only a single prism, or when Fresnel behaviour is not included in the modulator model. From the earlier experimental observations and previous models produced prior to the thesis, no fluctuations should be present. If any fluctuations were present in these versions of the Jones model, it would have suggested that Fresnel phenomena would not be able to explain the fluctuations and the hypothesis would need to be reconsidered. Fortunately, as seen in the table above, the outputs did follow the expected outcomes.

**Method Limitations**
Beyond just the method by which the model works, and the things the model can do, it is also important to discuss the limitations of the Python code and of the mathematical methods implemented into the functions.

The first limitation is the limitation on transforming the method from Jones to Stokes. This is due to the model not being able to achieve all 3 requirements as listed in subsection 5.2.2. This limits the ability of the model to be transformed into a Mueller-Stokes approximation which would possibly be more easily integrated into the pre-existing Mueller-Stokes models.

The second limitation is the inherent limitation to the input polarisation state caused by Jones formalism. The modulator is designed to work with all forms of incident light polarisation states, but the model is only able to represent fully polarised incident light as Jones formalism cannot do partial or unpolarised representations.

A third limitation of the models is caused by the simplification of the angles of incidence at each boundary. Normally, the ray splitting which occurs due to the birefringent material would result in different angles of refraction for each axis. These in turn would result in slightly different angles of incidence for each axis at the next boundary. To simplify this behaviour, instead the angles of incidence for the ordinary and extraordinary

ray were averaged to give the angle of incidence which was actually used. This simplification was made with the assumption that, due to the refractive indices in each axis being similar, the effect would be negligible.

The next limitation to the models is that the model is not currently designed to entirely take the true ray path into account. What this refers to is the fact that despite calculating angles of incidence and refraction, the ray is considered as always being at the exact same y-value in the height throughout the modulator. In reality, the ray would have changed its height after being refracted at each boundary. As the angles of refraction were within 1°, and the distances between boundaries are within 2.6 mm at the largest point in the actual modulator, the effect of the ray height change was considered negligible for this stage of the research. As an example, at the point where the boundaries are at 2.6mm apart, the angle of the light is at 1°from the horizontal. As the ray propagates, it will hit the next boundary at a height which is only 0.05mm lower than where the ray originated.

Similarly, related to the angles of incidence and refraction, the model does not account in any way for the ray no longer being perpendicular to the x-y plane. In a real experiment, the light will be encountering the birefringent material along an axis system which does not perfectly align with the fast and slow-axis coordinate system. This means that, in the correction factors and the Jones matrices alike, the true values of $n_s$ and $n_p$ will not be exactly equal to the fast and slow-axis refractive indices. As the angles were so small, for the purpose of the thesis it was deemed unnecessary to try to represent this change in behaviour as the effect was expected to only cause minor changes to the results.

Finally, the model as of now does not include the effects of internal reflections or inter-ray effects. The rays which bounce within the prisms and then reach the detector all have an effect on the final results. However, due to each reflection consisting of only around 2% of the light hitting the boundary, after two bounces, light reaching the detector is already only 0.04% of the original incident light intensity. The effect of these internal reflections is therefore neglected.

### 5.2.4. Results

As established earlier, of the 3 requirements which were desired for the model, the most critical in the investigation of the Fresnel fluctuations are the correct outputs of the intensity and polarisation states. As the separation method is the only method which achieves both, the results which are shown in this subsection all stem from this version of the Jones model.

**Results of the Separation Model**

For the collection of results, a wavelength of 0.5876$\mu m$ was used. This wavelength was chosen relatively arbitrarily as a wavelength which was within the range of what the modulator can work with. Using this wavelength, the model was used with incident linear polarisation Jones vectors of intensity 1, oriented along the 0°, 45°, 90°, -45° as well as Jones vectors for both circular polarisation orientations.

At a 0° incident linear polarisation orientation, the Jones 'separation model' produces the output shown in Figure 5.4. In this figure, the output is very clearly linear with no fluctuation. This is consistent with the theoretical foundation of the modulator given that the incident polarisation aligns with the fast-axis of the first prism. It also coincides with the expectation from experimental results performed by other members of the research team previously. Under ideal conditions, the modulator prisms do not create a pattern when the incident polarisation orientation is 0°. The same lack of fluctuation is also true when the orientation of the incident polarisation is at 90° as seen in Figure 5.5.

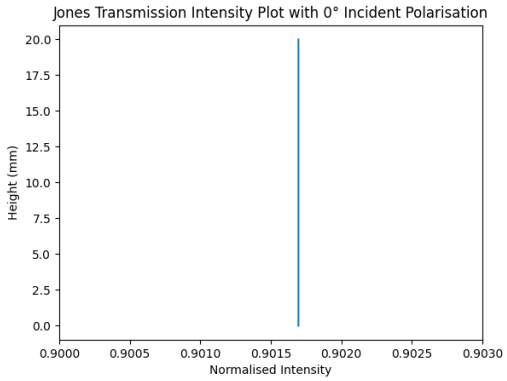


**Figure 5.4:** Transmission output of the modulator with an incident polarisation orientation of 0°

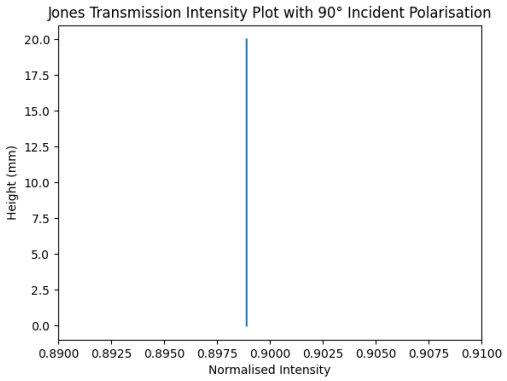


**Figure 5.5:** Transmission output of the modulator with an incident polarisation orientation of 90°

In the 90° case, the light is along the slow-axis of the first prism, but the same inherent linear pattern should occur. In Figure 5.5, the result is exactly as expected, with the only difference, when compared to the 0° case, being the slight reduction in output intensity due to the difference in perceived material refractive index.

The more interesting results occur when the incident polarisation state is instead at the midpoints between the two axes. According to the previous experiments performed, this is where the peak of the fluctuations should occur. When running the model with the incident polarisation state at 45°, the code returned Figure 5.6.

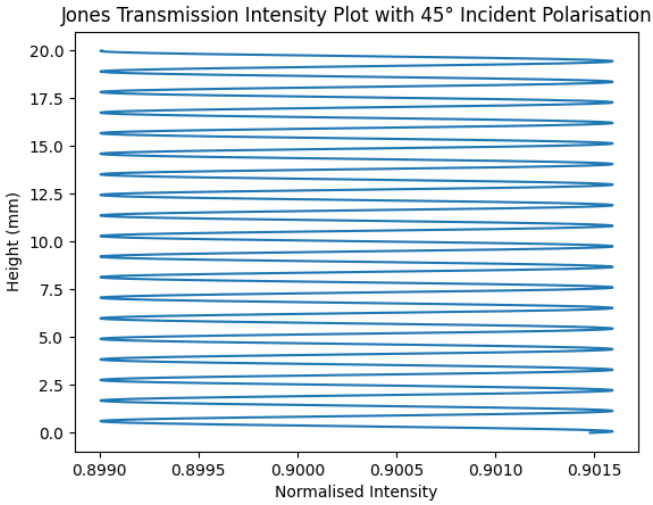


**Figure 5.6:** Transmission output of the modulator with an incident polarisation orientation of 45°

From the figure, it can be noted that the model does return the existence of the fluctuations. These fluctuations are not insignificant in amplitude either, with an approximately 0.2 peak to valley difference in normalised intensity. Along with the consistency in their behaviour, this suggests that they cannot simply be written off as rounding or calculation errors.

At -45°, the fluctuations reoccur the same as for the 45° case, but are mirrored. This is to be expected given the incident polarisation orientation being -45° instead of 45°. In essence, the result shown in Figure 5.6 is the same as the result from Figure 5.7 inverted.

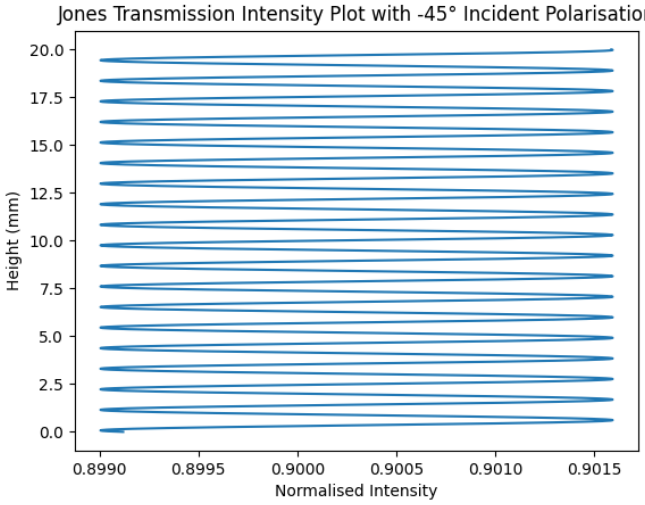


**Figure 5.7:** Transmission output of the modulator with an incident polarisation orientation of -45°

For the circular incident polarisation situations, the results appear as mirrored results similarly to the 45° and -45° results based on if the incident polarisation is right or left hand circular. The fluctuations are positioned as shown in Figure 5.8 and Figure 5.9.

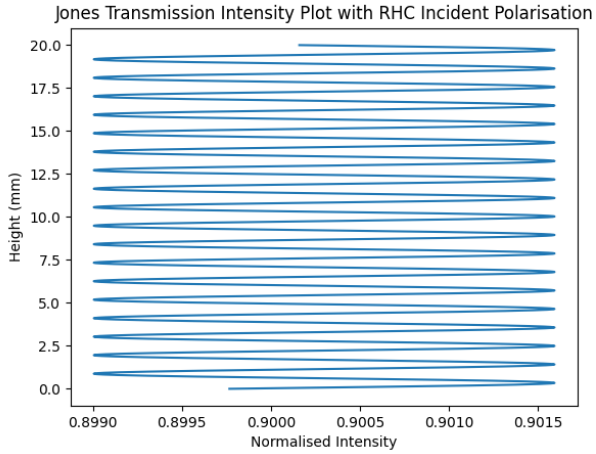


**Figure 5.8:** Transmission output of the modulator with an incident right hand circular polarisation.

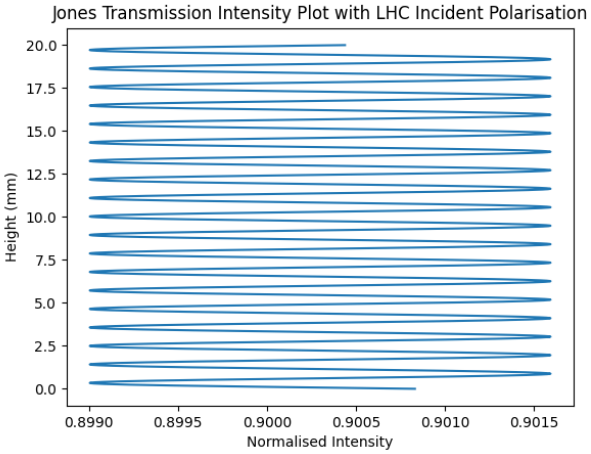


**Figure 5.9:** Transmission output of the modulator with an incident left hand circular polarisation.

At this stage, these results only show that Fresnel behaviour plays a large role in the creation of the intensity pattern. As such, the hypothesis that Fresnel behaviour is a reason that the modulator does not work as intended in its current state can be assumed to be proven. On the other hand, the results cannot be claimed to fully explain the fluctuations until they are verified and validated appropriately.

**Alternative Rotation Matrix Positioning**

In addition to the main results generated by the model, the alternative rotation placement from Gu and Yeh [1999] was also experimented with. As an example as to why this method was rejected, the resulting graph for 45° incident polarisation is given in Figure 5.10, which is the equivalent of Figure 5.6 but using the alternative rotation matrix positioning.

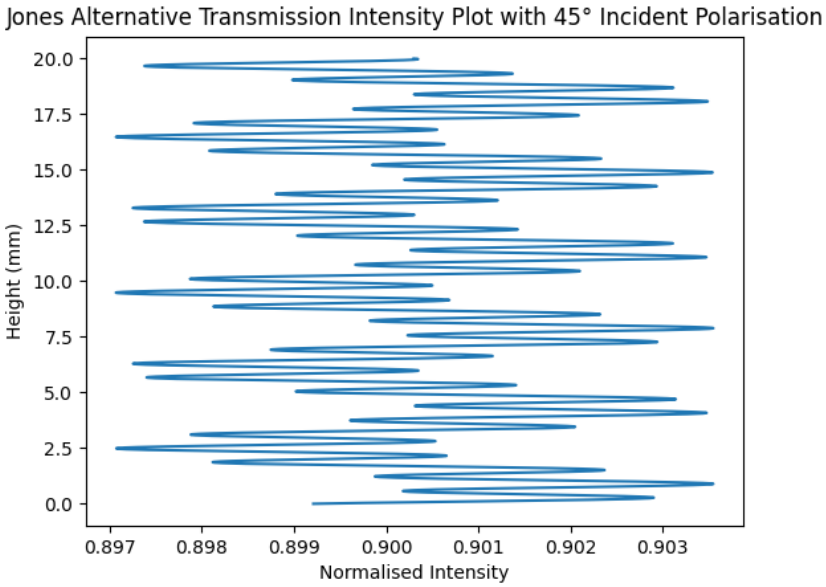


**Figure 5.10:** Transmission output of the modulator with an incident polarisation orientation of 45° and rotation matrices removed from the Fresnel matrices.

At first glance, the fluctuations are already distinct compared to those of the original model. There is a clear superposition of sinusoidal patterns which cannot fundamentally be explained with regards to what these would represent in real-world behaviour. The pattern bears little to no resemblance to the original experimental results from section 3.2. Based on the patterns from the original experiments, and on the understanding of the theory, this alternative calculation was not considered for the final version of the model.

## 5.3. Mueller-Stokes Model

At the same time as the Jones model was being produced to test the hypothesis that Fresnel phenomena caused the fluctuations observed experimentally, a similar Stokes model was also being produced. The reason for having this model in addition to the Jones model is that, as mentioned in chapter 3, the modulator was designed for full Stokes snapshot polarimetry. The limitations of the Jones method in representing partial or unpolarised light make using Jones as the basis for the thesis detrimental to properly representing the behaviour in all use cases of the prisms.

### **5.3.1.** Model Structure and Components

In terms of the structure of the Mueller-Stokes model, the same steps are taken as for the Jones model. First a file was created in which all the base components functions were created. These underwent the same procedure and testing as the Jones model version but, of course, with the Mueller matrices and their respective formulas. The linear polariser, waveplate and rotation matrices fundamentally are created exactly the same as their Jones counterparts, with inputs for orientation and phase difference where needed.

Rotation matrices were again included into each function and the individual matrices were tested to ensure that they could correctly obtain the output Stokes vector expected given a known input vector.

**Simple Modulator**

With the functions for each component already completed, again a simple modulator model can be produced. This model used the same fundamental structure and calculations as the Jones equivalent. The same inputs were given into the Python code except with an incident Stokes vector instead of a Jones vector. Similarly, the prisms and their phase shift formulas do not change between Jones and Stokes versions. The only difference when it comes to this model compared to the Jones model is the use of waveplate Mueller matrices and the Stokes vector representation.

While the purpose of this model is primarily to observe the outputs of the light through the 2 prisms with no Fresnel phenomena, it also can be used to verify the Jones model. In theory, as no additional effects are included, the two simple modulator models should obtain the same exact results in terms of the orientation of the output polarisation state.

### **5.3.2.** Fresnel Mueller-Matrix Limitations

When it came to making the model of the modulator with Fresnel behaviour included, Mueller-Stokes was found to be limited in terms of prior research. Fresnel behaviour has been represented in Mueller formalism previously in articles and books such as Collett [2005]but none of the commonly obtainable Fresnel Mueller matrices are designed for birefringence. As Mueller matrices are also less intuitive to work with that Jones, given the more complex nature of Stokes vectors, it was unclear if it would be possible to adapt the Mueller matrices to fit the needs of the model.

In Equation 4.24, the Fresnel coefficients for which the Fresnel Mueller matrices are designed all have the same refractive index. As the Stokes vector is not separated into two axes which can be aligned for the fast and slow-axis directions, the material properties and interactions between the two refractive indices of the prisms cannot be ignored or simplified in terms of their effect on the output vector by simply applying the corresponding refractive index to the corresponding axis. The design of the matrices being limited to conventional single refractive index materials is especially clear in the matrices for 0° angle of incidence. Articles and papers such as Collett [2005], Garcia [2011], Deibler and Smith [1999], Goldstein and Collett [2003] and Lindqvist et al. [2018] all provided the same form of Mueller matrices, but none combined birefringence into the calculations.

An extensive literature study was performed to further attempt to obtain a version which was capable of representing Fresnel on a birefringent boundary but unfortunately this was not found during the time which could be feasibly allocated to this task. Multiple sources were found which represent Fresnel boundary phenomena, but none established what to do in the case one material is birefringent. While it may be possible to apply the same general assumptions as those used in the Jones model, where the matrix in Equation 4.24 is adapted to use $\tau_s$ and $\tau_p$ with $n_s$ and $n_p$ respectively, it was uncertain if the results would be representative of the actual behaviour. Furthermore, due to time constraints, it was not feasible to perform thorough verification of how the method works with the 0° angle of incidence simplified matrices. It was therefore opted to focus on Jones for this thesis and the comparisons moving forward.

## 5.4. Small Birefringent Approximation

In both the Jones and the Stokes models some complication regarding the formulation of Fresnel phenomena led to the need for additional literature study to try to solve the issues posed by the Fresnel implementation. The lack of a completed model for Mueller-Stokes including Fresnel phenomena meant that there was no way to compare the results to the Jones method and use them to verify each other.

During the literature search, a method to rectify the lack of verification was found. This method, from Gu and Yeh [1999], suggests it is possible to completely remove the birefringent property of the boundaries if the refractive indices are very similar. The small birefringence assumption based on this paper states that, in the case that $|n_p - n_s| << n_p$, then it is possible to take $n_s$, $n_p = n_s$. Using this assumption removes all of the difficulties which the previous models encountered making both Jones and Stokes variants capable of producing the correct modulator matrix, the output polarisation states and the intensities all in one go.

It was decided to create versions of the Jones and the Stokes models using this assumption. This would allow for the comparison to be made between the two models using this assumption to prove that the Jones and the Stokes functions are written and functioning correctly.

### 5.4.1. Results

The resulting transmission plots of the small birefringent approximation methods were created for both Jones and Stokes versions of the model. The main result of interest is what occurs when the fluctuations should be at their greatest. To compare the two methods, both methods were plotted on the same graph to get a proper comparison of the two.

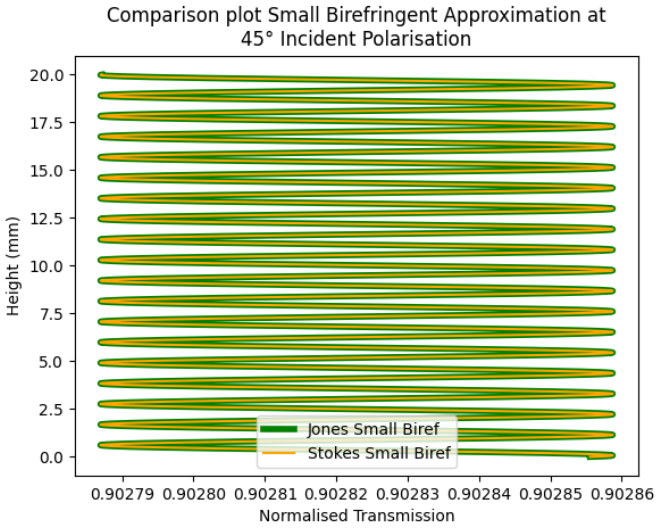


**Figure 5.11:** Small birefringent approximation transmission pattern at 45° incident polarisation, with the orange line representing Stokes and the green representing Jones results.

In Figure 5.11, the graphs for the 45° incident polarisation case are shown. The plot shows that the results for both Jones and Stokes versions of this model are identical. The same holds true for all other incident polarisation states, hence they are not shown.

What this perfect overlap suggests, is that the models in Jones which have been produced so far are correctly implemented and have been verified by the Stokes counterpart in all steps other than the Fresnel birefringent matrices. It can be concluded from the small birefringent approximation that the waveplate matrices, matrix multiplications, input parameters and the outputs are all correctly performed. Additionally, the existence of fluctuations despite the lack of birefringence in the boundary matrices shows that the intensity pattern should exist and can be mathematically proven to occur when the two prisms are modelled with Fresnel interactions. This confirms that Fresnel phenomena cause fluctuations, though whether they cause the precise fluctuations from experimental observations cannot be determined with the small birefringent approximation. Nonetheless, being able to demonstrate that fluctuations correlate to Fresnel phenomena inclusion into the model, even when in a simple form, is a valuable first step in examining the extent to which the experimental fluctuations are related to Fresnel behaviour.

### 5.4.2. Observations and Limitations

The small birefringence assumption has shown that the Jones and Stokes methods are equivalent for all incident polarisation states and has given confidence in the model designs. Despite this, it also is clear that the assumption does not produce accurate amplitudes in the fluctuations. The method is not able to portray the exact behaviour of the light which is also clear as the reflection and transmission percentages of the input light no longer correspond to the true material values from the database.

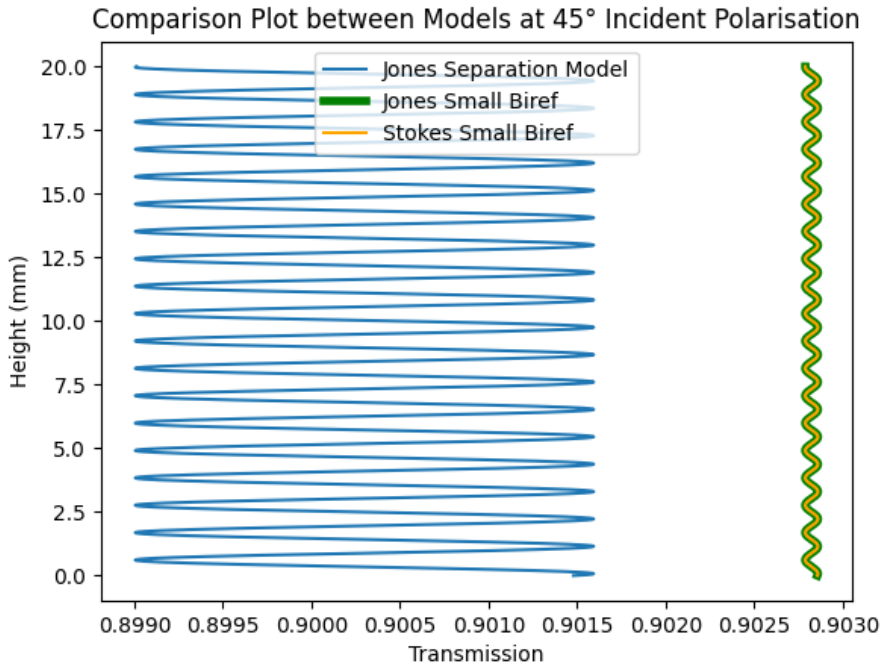


**Figure 5.12:** Plot showing the comparison between the Jones separation model results with the small birefringent approximation results for an incident linear polarisation at 45°.

In Figure 5.12, the period is exactly the same as the regular Jones model with a period of 1.08 mm. The amplitude on the other hand, is incomparable with the separation model having a peak to valley of 0.2 and the small birefringent model at 0.00007. The average transmission difference could be explained possibly as a consequence of the birefringent nature of the boundaries being neglected. As the boundaries all only include the refractive indices of the fast-axis the rays transmit more through each boundary than would be the case if both refractive indices are considered. Potentially using some approximation or averaged value would reduce the difference, however, how to confirm what the true effective refractive index would be is not yet known and was considered outside the scope of the small birefringent approximation model.

# 6

# ZEMAX Simulations

In the previous chapter, all of the Python model variants are discussed. The models have proven their capability to show fluctuations in the intensity due to Fresnel, but have not yet been verified. In this chapter, the ZEMAX simulations created in order to verify the models are presented. To begin with, in section 6.1, the software used is introduced in terms of what it is and how it works. In section 6.2, the steps and choices made during the creation of the simulations are explored. After this, in section 6.3, observations, tests, and simulation issues along with methods to mitigate or remove them, are discussed. Finally, in section 6.4, the method of obtaining the results is discussed, along with noise mitigation strategies used. Furthermore, the final results of the ZEMAX simulations are shown and compared to the Python models.

## 6.1. Software

ANSYS ZEMAX Opticstudio is a software designed for the purpose of simulating optical setups, components and materials. The software is advertised as being created with the intent of letting users design "components and sub-assemblies" within "complex, high-precision optical systems"[1]. According to the ANSYS website, it is described as a software capable of being used for simulating and designing systems in "AR/VR to LIDAR, medical imaging to data communications and more".

### **6.1.1.** Software Capabilities

The software is extremely versatile in designing optical systems. ZEMAX provides the user with the capability to simulate various types of light behaviour.

The main key software capabilities are listed here based on the marketed key features[2]:

- Ray Tracing
- Lens Design
- Tolerance Design
- Parameter Optimisation
- Interoperability
- Multiphysics Simulation

The software capabilities of ZEMAX OpticStudio are far above and beyond what is specifically necessary for the simulation of the modulator used in this thesis, however, the main draw of the software comes in the form of the first two key features. These two features are described in the following way:

- Ray Tracing: ZEMAX employs ray tracing algorithms to simulate the behaviour of light in an optical system. This can be used to analyse the ray through different lenses, mirrors and optical components.
- Lens Design: ZEMAX has a vast array of tools which can be used to design specific lenses. The lens can be adjusted and optimised in shape, material, and coating.

The ray tracing algorithms mean that it is possible to simulate the behaviour of light through the prisms in not only single ray analysis like in the models, but also including ray interactions across a large number of simultaneously analysed rays. Furthermore, the refractions and reflections of the rays can be considered in

[1] URL: `https://www.ansys.com/products/optics/ansys-zemax-opticstudio#tab1-2`, last accessed 05-02-2025
[2] See footnote 1.

the simulation as ZEMAX calculates the path which the ray follows in its entirety, meaning the precise way in which the ray passes through the prisms and interacts with them can be accounted for including internal reflections. This feature is the primary reason for the choice to use ZEMAX for this thesis. The lens design feature which ZEMAX provides is also a major reason for the choice of ZEMAX. Within the lens design tools are also the tools necessary for designing the prisms of the modulator accurately. The shaping tools for lenses can be applied to creating the prism shape, and the material libraries integrated within ZEMAX also include birefringent materials such as Magnesium Fluoride which is used in the modulator. This is the second reason why this software was selected for the thesis.

As an added benefit to this choice, ZEMAX was already relatively easily obtainable as it is commonly used by other members of the Space Instrumentation group in the Space Engineering department who also work on the modulator design. By using ZEMAX it is also possible to collaborate with experts from TNO who are also involved in the project and can provide advice on ZEMAX related issues.

### **6.1.2.** Sequential vs Non-Sequential

ZEMAX has two primary methods by which to conduct ray tracing analysis of an optical system. These are known as sequential and non-sequential mode. The choice between these two simulation modes establishes the complexity and the capabilities of the simulation which will be generated. There are many advantages and disadvantages to each option when it comes to implementation of the modulator simulation. Here, the specific considerations are compiled to explain why each method could be used, which is more helpful to the verification process and how the final decision of which to use was made.

To begin with, both sequential and non-sequential are ray-tracing computation methods which ZEMAX can use to simulate optical behaviour. The primary difference between sequential and non-sequential is how much freedom the software has to trace the ray paths. In sequential mode, the ray path is traced between the specific surfaces as defined by the user. This makes sequential ray tracing extremely fast as the ray is not simulated in terms of behaviour on any path other than the exact path implemented. Furthermore, the software allows for easy definition of all the surfaces with which the ray comes into contact such that the simulation can be adapted to the users needs. One of the ways in which this is possible is with the integrated Jones matrix tool which lets the surface be defined according to the Jones matrix describing its effect on the ray. Beyond this, sequential mode is generally more user friendly and simpler to use for the purpose of designing optical components such as lenses or prisms.

Non-sequential mode, on the other hand, does not limit the ray to a single path. Instead, non-sequential mode will simulate the ray interactions with all objects in 3D space, making positions, incidence angles, orientations and material properties far more critical. Instead of defining the surfaces which the ray comes into contact with, now it is necessary to define the entire system along with each individual component. Because every component is defined in 3D space, the ray tracing is now capable of doing reflections and calculating what occurs as a ray passes through without the user defining exactly where the ray is supposed to go. This means that boundary reflections, internal reflections and rays which are deviated from the expected path can all be simulated to show what the 'actual' effect on the incident light is. The consequences of choosing this mode are that the work and effort needed to implement the system properly increase, and the computation time increases exponentially when more rays and more ray bounces are implemented.

To summarise the main advantages and disadvantages of each ZEMAX mode, Table 6.1 is added below.

**Table 6.1:** Table showing the main differences between sequential and Non-sequential modes for ZEMAX ray-tracing

| Sequential Model | Non-Sequential Model |
|---|---|
| All surfaces are defined in the sequence the ray should interact with them | Surfaces are defined as objects in 3D space |
| Surfaces are easily manually definable with Jones matrices | Objects are simulated based on materials and geometric parameters |
| Fast ray tracing as the ray path is pre-defined | Slow ray tracing as ray can split, reflect and bounce |
| Cannot perform simulations with ray splitting or ray scattering | Can perform 3D simulations of reflections and ray scattering in addition to the transmission of the ray |

## 6.2. Creation of the Simulation

For the proper creation of the ZEMAX simulation there are also additional decisions which have to be made. The ZEMAX simulation mode selected, for example, dictates how the simulation can be compared to the Python model and the experiments directly. If sequential mode is used, each boundary would have to manually set to both cause an energy loss and to do so in accordance to the birefringent properties. While this is possible, it introduces a significant bias towards how the surface is defined. In addition to this, effects related to secondary reflections would be entirely neglected. Furthermore, colleagues working on the modulator design itself had previously recreated the simulations in sequential mode with 'energy losses' at the boundaries to simulate the transmission percentage through the boundary surface. These simulations, were unable to show the intensity fluctuations observed in experiments. As mentioned before, sequential mode requires surfaces to be defined by the user, and in these previously performed simulations the surfaces and prisms had been defined as ideal Jones matrices. Furthermore, the boundaries between materials should be implemented as their own surfaces which was not done in these simulations.

Rather than attempting to come up with a method of telling the simulation how to approximate Fresnel behaviour at the boundaries in a sequential simulation, it was determined that all of the difficulties regarding Fresnel phenomena in sequential mode, along with the bias which implementing the approximations would cause, could be avoided entirely with non-sequential mode.

Non-sequential mode would be able to accurately perform Fresnel ray tracing and would include considerations for multiple internal reflections. Furthermore, as the purpose of the thesis was to explore the possible causes of the intensity fluctuations, letting ZEMAX calculate the ray paths and interactions freely, without telling it what surfaces it should interact with and how, should result in a simulation that includes phenomena which might not have been considered by the group previously.

Having established the mode in which to perform the simulation, now it is necessary to learn how to use non-sequential mode. As no one else on the research team had created a non-sequential simulation of the modulator, it had to be started from scratch. In order to learn how to use ZEMAX an initial study period was set aside. During this study period, resources and tutorials from both the ANSYS site and from the ZEMAX community knowledgebase [3] were used. Some preliminary simulations were performed, recreating the examples which were given until a fundamental understanding of the software was obtained. After this period of study, it was possible to work on the modulator version instead.

### **6.2.1.** Defining the Components of the Simulation

The first stage of creating a non-sequential simulation in ZEMAX, is defining all of the components which need to be put into the simulation. Based on the component list used in the experiment, the system must be composed of the source, spectral filter, linear polariser and quarter-waveplate for source light manipulation, the two prisms, and the detector. For the first 4 components, ZEMAX can simplify everything into a single 'source' which can be set to produce the rays with a specified polarisation state. The wavelength can also be set for the source in the simulation parameters. This leaves a final list of a source, the two prisms and the detector which need to be implemented. For the sake of observing the ray behaviour at different points, multiple detectors were placed in the final simulation.

For the creation of the source, ZEMAX offers many choices in terms of how the rays should behave. These choices are either in terms of the shape of the source or the behaviour of the source. Examples include diffractive sources, diode sources, filament sources, Gaussian sources, elliptical sources, point sources, radial sources, source volumes as well as user defined sources from IESNA or EULUMDAT files. More options also exist, but for the sake of this simulation, complex sources are unnecessary. Instead, the chosen source was the 'Source Rectangle' setting. This setting simply creates a rectangular source which outputs rays equally across the specified area. The parameters which need to be specified for the source are the positional coordinates, the tilt around each axis, the number of rays, the power, and the size of the rectangular source. More options exist to fine-tune the source but are not required as a simple homogenous source is desired. The source was set to be positioned centrally with no tilt, directing rays along the Z-axis. The size of the source was changed depending on simulation area of interest. Originally, this was set to a 20x20mm area which matches the dimensions of the modulator prisms. In future simulations the dimensions were altered either due to artefacts or ray density and computational limits. For the number of rays, it was varied depending on need, with a lower number of $1E+6$ for testing simulations and a peak of $1E+8$ for final simulations. Rather than increasing ray counts, it was more efficient to increase ray density through decreasing the source area. Furthermore, on most simulations, having

[3] URL: `https://community.zemax.com/general-discussion-1`, last accessed 22-11-2024

less rays than $1E+8$ led to the ray counts per detector pixel varying too much to show clear results.

After the source, the two prisms have to be implemented. Creating the prisms requires the most attention in the entire ZEMAX simulation process. There are a few principal steps to creating each prism in ZEMAX properly:

1. Creating a POB file with the vertex coordinates and vertex to vertex links which define the faces of the shape.
2. Importing the file into ZEMAX and ensuring the faces are correctly defined.
3. Positioning of the prism with respect to the source.
4. Importing the ZEMAX materials database in which the desired material is included, and setting the prism to this material.
5. Selection of coating materials for each individual face.
6. Selection of refractive index type, between isotropic, birefringent and GRIN (Gradient Index).
7. Alignment of the fast-axis in the case of a birefringent material.
8. Selection between ray tracing modes within the prism which change how transmitted and reflected rays are traced.

The first step, the creation of the POB file, was performed in a notepad. Within the notepad, each vertex of the prism had to be positioned with respect to whichever point on the prism was to become its 'origin point'. Each prism gets its own POB file, so that they can function as independent objects in ZEMAX rather than being treated as the same object. The POB files for each prism must have their own origin point from which the vertices are defined to create the shape of the corresponding prism.

Initially, the first files created for each prism used the centre of the first face of each respective prism as the origin point, but after the implementation of the second prism, a common origin point for both prisms turned out to be the better solution. Therefore, for simplicity, this origin was chosen as the centre of the front face of the first prism. The vertices were then given coordinates in millimetres with respect to this point. A diagram of the different vertex numbers and coordinates is given below in Figure 6.1.

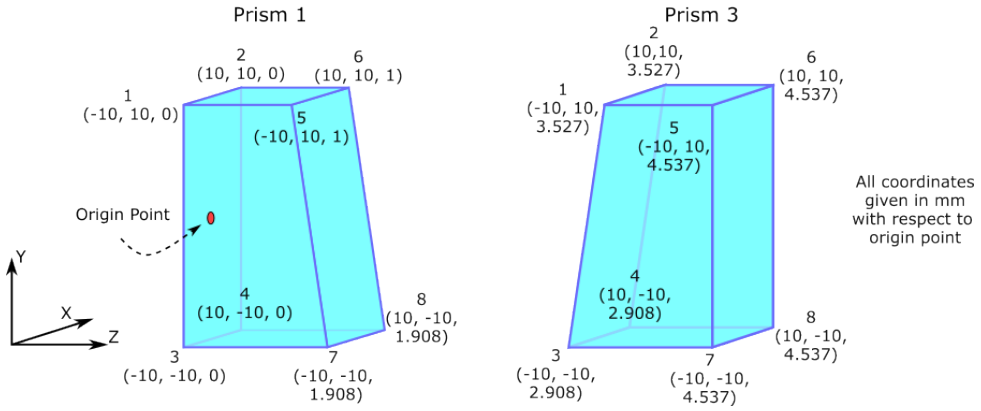


**Figure 6.1:** Modulator Prisms 1 and 3 with the vertex numbers and coordinates used to create the two ZEMAX prism objects. Each prism is its own 'object' within ZEMAX but both are defined with respect to the same point.

As an example of vertex formatting, the line for vertex 3 of the first prism is V 3 -10 -10 0. V is used to designate the coordinates as corresponding to a vertex, the number after the V is the vertex number.

After the vertices are written in, the 'links' between the vertices are also added in the form R 1 2 4 3 0 1, where R stands for rectangular face, and the numbers correspond to the vertices which make up said face. The last number is the face number. Additionally, the order in which the vertices are added to the list establishes how the rectangular sides are formed. The wrong order will result in impossible shapes and will lead to a failure to import the file. The '0' in the list of numbers sets the face to be a default face as opposed to '1' which sets it to be a reflective face, or '2' which makes it absorbing. The files themselves can be found in Appendix B.

Once both prisms have been imported, and everything is working as intended with regards to the shape and position of the prisms with respect to the 'origin' point, the position of the prisms has to be set with respect to the source. As the prisms are defined based on a common origin, the spacing and position of the prisms

with respect to each other is always consistent as long as the origin point is set as the same point for both. Positioning of the prisms in the simulation therefore only requires positioning of this origin point. The origin point was placed 15mm after the source, as the rays should not change behaviour between the source and the prism, but it gave a comfortably large usable space in-between to place additional detectors or components if it became necessary.

To be able to now simulate the behaviour of the prisms appropriately, they must now be set to the correct material. Within ZEMAX there are inbuilt material databases. These databases separate the many possible optical materials based on certain properties. One of these databases is labelled 'BIREFRINGENT' and includes Magnesium Fluoride. It is also possible to create custom materials with specified behaviour, but for the purpose of this thesis the default version is sufficient. The prisms can therefore easily be set to the 'MGF2' setting once the database is imported. ZEMAX also allows a user to implement various coatings for the components. In the case of the modulator prisms, the coating for each face has to be manually set to none rather than the default 'ideal coating' setting. Furthermore, the next step of setting the refractive index type is also necessary to ensure the material is being used as a birefringent material. Simply telling the software to use Magnesium Fluoride is not inherently sufficient even if it is from a birefringent database. After the prisms have been set to be 'birefringent', the fast-axis alignment can be set as well.

The final step to finalising the prisms is selecting the method in which the ray tracing should be performed at the boundaries. This step of the process influences the results in different ways depending on the decision made and therefore requires the most explanation. Because of the need to go into further detail, the explanation has been set aside for subsection 6.2.2.

In the end, the prism settings in ZEMAX look as shown in Figure 6.2, with the final ZEMAX prisms being visually portrayed as shown in Figure 6.3.

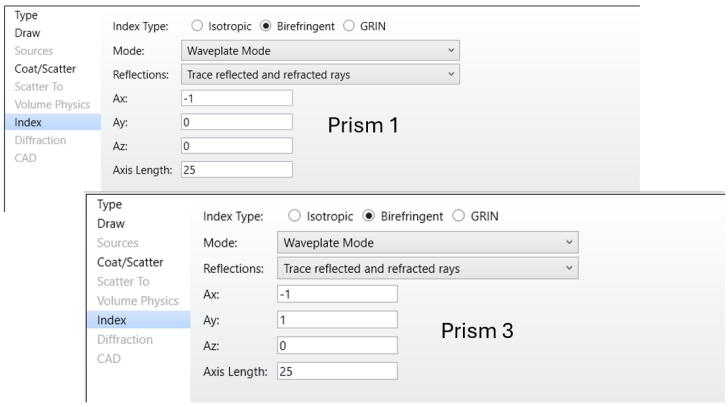


**Figure 6.2:** Parameter settings for the material and ray tracing modes.

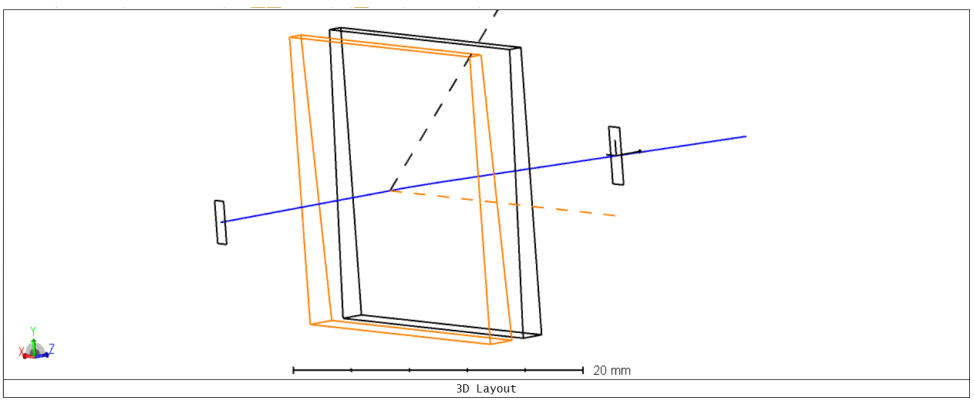


**Figure 6.3:** Prisms as shown in ZEMAX. The orange prism is prism 1 with the black prism as prism 3. The fast axes are shown as the dotted line with each colour corresponding to the prism the line belongs to. Both lines appear at the origin point of the prisms vertex definitions hence the mutual origin.

The last component in ZEMAX which needs defining to get a complete simulation is the detector. The detector 'objects' in ZEMAX are used to dictate where the rays should be measured. Multiple detectors can be used and spread out wherever they are needed. The detector object have a few main parameters which must be set in order to use them effectively. The first parameters are the positional parameters. These change based on where the detector should be. Additionally, the tilt can be used to orient the detector in different directions in case it needs adjustment. The next parameters are the size parameters with which the width and height of the detector are set. The values which should be chosen for these parameters directly influence and are directly influenced by the choice of the next parameters, which are the pixel counts per axis. The pixel counts have a maximum value of 6000 pixels per axis which are evenly distributed along the entire length of their respective axis. This means the choice of detector size influences how large the pixels are. Finally, the last set of parameters which need to be altered are the choices regarding the field of view of the detector. For the simulations performed on the modulator, the default field of view was used. This lets the detectors take light in from any angle that hits the detector surface. The only setting which was changed was the setting to make all detectors 'Front Only'. This prevents the detector from being affected by light at both sides. Due to the nature of the prisms and the internal reflections, having a double sided detector would cause issues as the reflections would interfere with the clarity of the actual desired results.

Deciding on where the detectors should be positioned depends on what needs to be checked in the simulation. It is also possible to have multiple detectors as long as the settings in ZEMAX allow rays to pass unimpeded through detector surfaces. In the end, it was decided that detectors should be placed before and after each component. As such, one is placed immediately after the source to observe the source behaviour. Another two are placed before and after the first prism. The first of them observes the reflections on the first boundary, and the second the transmission through the prism. The same is done for prism 3 with one detector for reflections and one for overall transmission.

### **6.2.2.** Prism Ray Tracing Mode

Within ZEMAX there are two drop down boxes which are labelled 'Mode' and 'Reflections'. These can also be seen in Figure 6.2. Within the drop down boxes are the different options which ZEMAX offers in terms of how the material should affect the ray tracing when the light enters and exits the prism. For the 'Mode' setting, there are 4 options:

- Trace ordinary and extraordinary rays
- Trace only ordinary rays
- Trace extraordinary rays only
- Waveplate Mode

The first 3 options all appear self explanatory based on the knowlegde that a birefringent material causes a separation of the ray into an ordinary and extraordinary ray. Therefore, with these 3 options, the user can dictate whether only one ray is being investigated, or if ZEMAX should keep both in the final results. The more critical decision was between tracing both rays, or the waveplate mode.

To clarify the distinction between the two options, the specific way each works was looked into within the documentation of the software. Based on the documentation provided by ZEMAX, the choice between the two modes is a trade-off between if the ray should simulate polarisation or the true ray paths.

From the documentation of the software, it was suggested that if the option to trace ordinary and extraordinary rays was chosen, the true polarisation state of the ray would be lost in the ray separation. On the other hand, the waveplate mode appears to neglect the separation of the two rays entirely. In waveplate mode, the ordinary and extraordinary ray stay united along the same path. Instead, ZEMAX simulates the change in the polarisation state of the ray as a whole. The true ray path is sacrificed in favour of correctly simulating the effect of the prism acting as a waveplate. To begin with, simulations were performed to verify the behaviour of each mode individually.

The first, when the prisms were both set to trace mode, led to results which showed no fluctuations after the modulator prisms no matter what the incident polarisation state was set to. This lack of fluctuations prior to the analyser is contrary to both the older experimental observations and the Python models created in chapter 5. It is likely that the reason for the fluctuations no longer occurring is related to the fact that there is no consideration of the waveplate effect of the prisms. This also means that the phase shift which is induced differently across the height of the modulator is not simulated, making the transmitted rays identical to each other rather than producing differences in polarisation state.

In the second check, the prisms both had waveplate mode enabled, the results of the simulation immediately

begin following the general expected pattern where fluctuations are present after the modulator prisms. Because of this, if a choice must be made between the two modes, it is believed that waveplate mode is the better choice for the simulation of the modulator.

The clear distinction between the two modes means that there is no inbuilt method of getting both the path and polarisation calculated in their entirety simultaneously. As such, it was decided that some experimentation with the software should be performed to observe if anything could be done to approximate both at once. To this end, some 'boundary' elements were added to the prisms in the configurations portrayed in Figure 6.4.

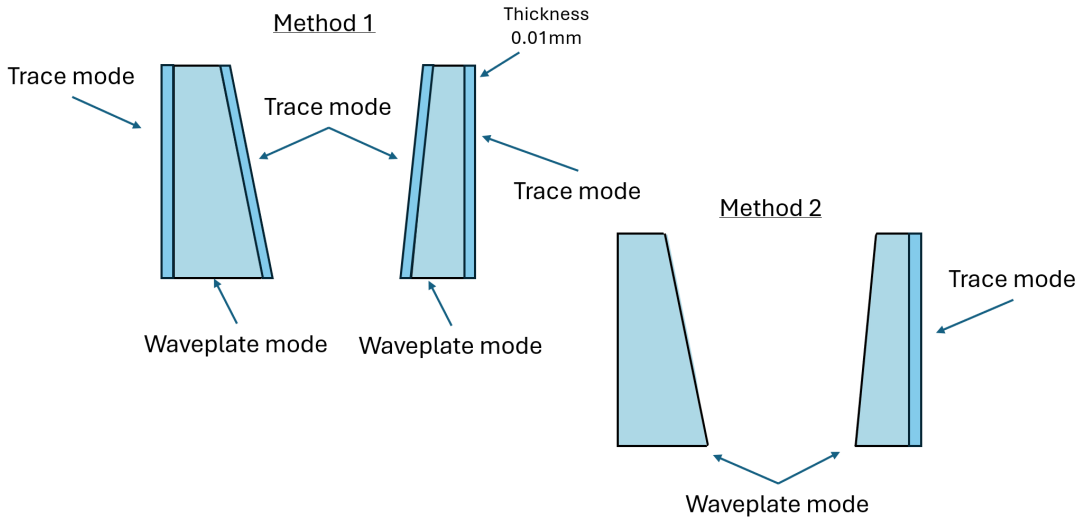


**Figure 6.4:** Diagrams depicting the two attempted methods of simulating both the ray splitting and the polarisation of light simultaneously. Each method was performed by adding trace boundary elements to the prisms in ZEMAX as shown in the figure.

These boundary elements were created in the same way the prisms were as separate objects. The connections with the prism were then altered to be 'ideal' in order to negate the fact that there is a change in 'medium' which realistically would not be there. The idea behind these simulations was to attempt to induce a splitting of the ray in the boundary where it theoretically would occur, and then still have the waveplate mode to calculate polarisation changes in the light.

The first method applied these boundary elements to every boundary the light passes through. The intent behind this method was to get the light to separate at the entry into the prisms, and then also be able to separate at the end of the prism. In this way, light can follow both ordinary and extraordinary rays at each boundary. Furthermore, this also allows for a separated ray to enter the next prism. In this way, ZEMAX has the capability to simulate the exact separation behaviour at each prism edge including any second degree separation caused by exiting the first prism and entering the third.

In the second method, only one boundary element is included at the end of prism 3. The goal of this simulation was to see if there is any significant difference in the results if the polarisation of the ray is calculated using the waveplate mode, and the ray is only separated at the very end.

With the 2 methods established, various simulations were run to compare the results to the Python models and to the regular waveplate mode simulations. These simulations were performed using sources of 2mm in height, centred around the midpoint of the modulator. Because of this, only this region can be compared to the Python model. The region was set to be so small due to computation time limits and due to the pixel size being directly affected by detector height. To ensure that the resolution of the results and the ray density were satisfactory, this was the region selected for this first comparison.

From the simulations, and the comparisons made to both the Jones model and the previous simulations with no trace elements, the following observations were made:

The first method resulted in patterns which were not representative of the expected behaviour. These did not match with the Jones models, nor the waveplate-only versions of the simulation. This resulted in method 1

being disregarded for future simulations as it did not appear to accurately represent real behaviour.

For the second method, where only the last boundary was applied, the results were very similar to the simulations which did not include trace elements at all. To clarify the decision between the two simulation versions, a consultation was requested with ROB Vink, a ZEMAX expert from TNO. In the consultation, the conclusion was that, despite ZEMAX performing the simulation successfully and the results being similar to waveplate mode, the inclusion of the trace mode elements did not actually allow ZEMAX to simulate both effects together. While overall the results appeared consistent when a trace boundary element was included at the end of prism 3, the uncertainty in how exactly ZEMAX dealt with the polarisation state and the cause of the remaining differences between the simulation versions made it undesirable to use the boundary elements at all.

After this investigation, the ZEMAX simulation was reverted to the two waveplate mode prisms with no additional elements. This minimises the unknowns regarding how ZEMAX is simulating the ray propagation, and also simplifies the simulation in terms of computation time. While trace mode is fully sacrificed, the result is more reliable and can lead to more consistent conclusions.

The plots obtained from the simulation, and a more detailed explanation of how the comparisons were performed, are both presented in Appendix C.

### 6.2.3. General Simulation Overview

In this subsection, a general overview is given of the simulations. Generally, the only changes between simulations were the incident polarisation and detector positions and sizes. Figure 6.5 shows the general layout of all of the simulations, with the relative positions of each component.

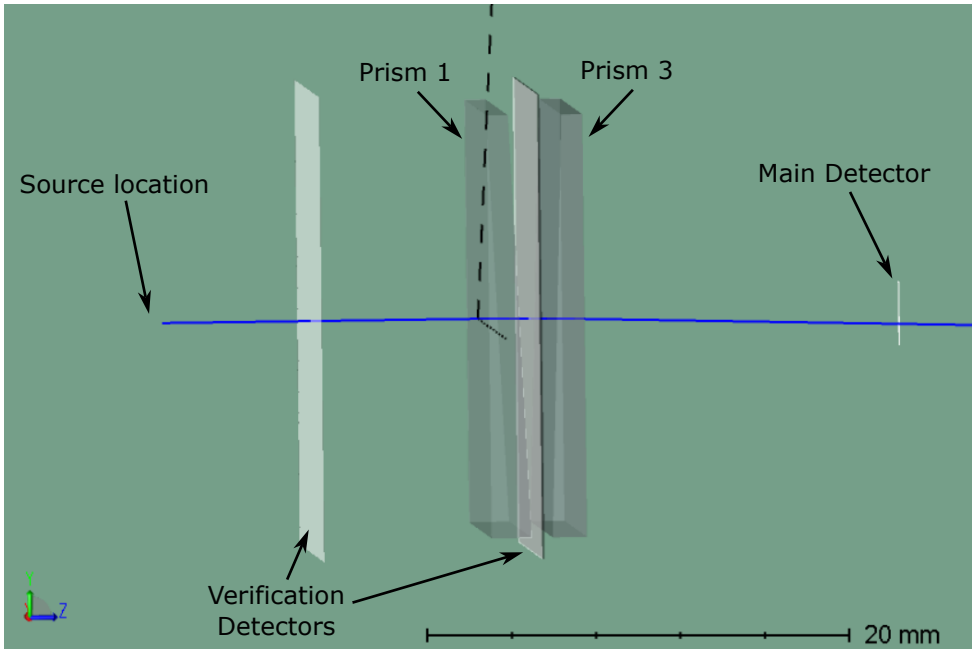


**Figure 6.5:** Overview of ZEMAX prisms and detector positions. The ray shown originates from the source on the left side. All objects and detectors are set to their final positions and sizes. The internal reflections are not included for clarity.

The original simulations were performed with detectors which matches the size of the modulator in terms of height. This gave a full view of the patterns in the output along the full height of the prisms. Later, due to reasons which will be discussed in subsection 6.3.2 and due to pixel density considerations, the source, and the detector used to monitor the output through the prisms, were reduced in size substantially. Beyond this, the prisms remained unchanged along with the detector positions along the z-axis.

The ZEMAX simulation specific parameters which are of particular importance are shown in Table 6.2. These parameters affect the wavelength of the source light, the number of ray intersections and the times a ray can be split.

**Table 6.2:** Table showing main ZEMAX simulation parameters for ray tracing.

| Parameter | Value | Reasoning |
|---|---|---|
| Wavelength | 0.588 | Closest to the Python models as ZEMAX allows |
| Maximum Intersection Per Ray | 100 | Gives an upper limit for the ray to interact with boundaries multiple times |
| Maximum Segments Per Ray | 2000 | Given an upper limit so each ray segment to be traced after each interaction |
| Minimum Relative Ray Intensity | 1E-7 | Reduces computation time by limiting the ray intersections and segments based on ray intensity |

Finally, to summarise the simulation shown in Figure 6.5, the settings used for the final components and objects implemented into the simulation are given in Table 6.3. In this table, all of the components of the final simulation are presented with their position, dimensions and any other relevant parameters. The large detectors, all of which are 22mm by 22mm, were used to verify that the simulation was performing ray tracing as expected. As they were not used for the final plots of the transmission, they did not need to be scaled down, nor have increased pixel counts. As for the pixel counts of the main detectors, the y-axis is the axis of interest and therefore has the higher pixel counts.

**Table 6.3:** Table showing the objects which form the final simulation, and their positions, dimensions and relevant additional parameters in their final forms.

| Object | Position Coordinates (x,y,z) (mm) | Dimensions width x height (mm) | Additional Information |
|---|---|---|---|
| Source Rectangle | (0, 0, 0) | 1 x 3 | 1E8 Rays at user specified polarisation state, 1W Power |
| Source Detector | (0, 0, 7) | 22 x 22 | Backward-facing only, 150 x 150 Pixels (x, y) |
| Boundary 1 Reflection Detector | (0, 0, 7) | 22 x 22 | Forward-facing only, 150 x 150 Pixels (x, y) |
| Prism 1 | Origin at (0, 0, 15) | (Set by POB file) | MGF2 Birefringent material Prism shape set by POB file |
| Prism 1 Transmission Detector | (0, 0, 17.35) | 1.2 x 4 | Backward facing only, 150 x 3000 pixels (x, y) |
| Prism 3 Reflection Detector | (0, 0, 17.45) | 22 x 22 | Forward-facing only, 150 x 150 Pixels (x, y) |
| Prism 3 | Origin at (0, 0, 15) | (Set by POB) | MGF2 Birefringent material Prism shape set by POB file |
| Final Transmission Detector | (0, -0.5, 35) | 1.2 x 4 | Backward-facing only, 200 x 3000 Pixels (x, y) |

## 6.3. Observations

In this section, the main observations from the various simulations are discussed. It is necessary to look at all the different behaviours of the simulation and explain how the simulation changed. This includes both initial tests related to understanding how ZEMAX simulates birefringent materials, boundary behaviour and testing if the behaviour of single prisms is consistent with experimental observations, but also different unexpected behaviour which had to be treated and resolved. The method through which such unexpected behaviour was dealt with is also discussed.

### **6.3.1.** Single Prism Verification

To begin with, the initial tests which had to be performed in ZEMAX were the checks that the expected behaviour of a single prism follows based on the theory and the experiments performed previously. A single prism was simulated at first, to verify that there are no detectable fluctuations in the light output at any incident po-

larisation state. With this simulation, it was confirmed that ZEMAX produces the same constant transmission patterns which are expected at any incident polarisation. The lack of an intensity fluctuation after a single prism is exactly as expected from previous models. This gave the confidence to continue working with ZEMAX and to continue the implementation of the combined first and third prisms. This also confirmed that any resulting fluctuations when using 2 prisms is, in face, occurring due to the combination of 2 prisms and not because it already existed from the first.

### 6.3.2. Artefacts and Anomalies

One of the unexpected behaviour instances to be discussed occurred when using sources which were the size of the prisms entire height. This was mentioned briefly in subsection 6.2.3 and is one of the reasons for changing the source and detector size. In Figure 6.6, a white line can be seen at the bottom.

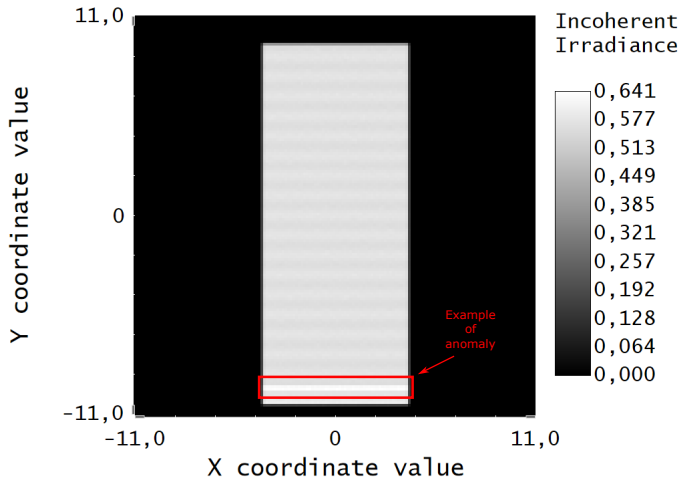


**Figure 6.6:** Example of early simulation results showing both intensity fluctuations and the artefact at the bottom as a disproportionate peak in intensity.

The same type of artefact occurs at any incident polarisation state and are consistently visible whenever the source and detector are as tall or taller than the prism. These lines appear to be extremely high intensity light which has been detected by the detector. As the intensity value at the white line is almost exactly equal to the incident light intensity it is assumed that they do not represent a real ray behaviour which can be replicated in an experiment. Instead it behaves as though the ray does not interact with all of the boundaries and passes through directly from one side to the other unimpeded.

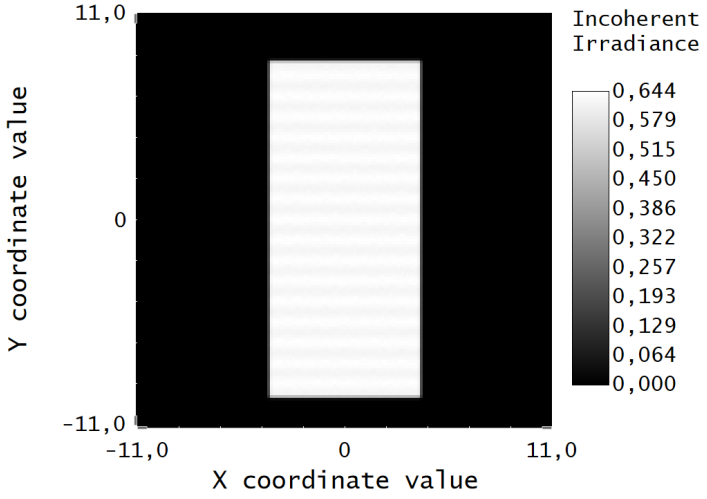


**Figure 6.7:** Example of early simulation results after the source was slightly reduced to remove the artefact.

Upon reducing the height of the source and avoiding the edges of the prism, these lines were not visible any more even if the detector was moved up and down to various other locations. With the artefacts not showing up with the smaller source sizes, the investigation into their cause was stopped at this point. An example of the same results with the detector reduced in size can be seen in Figure 6.7. As the source was reduced in size, the ray density was increased resulting in the difference in the values of incoherent irradiance between this figure and Figure 6.6.

### 6.3.3. Ghosting

Another instance of unexpected behaviour was the appearance of a fluctuation pattern when an incident linear polarisation at either 0° or 90° passed through both prisms. Based on the models and the theory behind the prisms effect on polarised light, this should not be occurring. As the first prism has either the fast or slow-axis perfectly aligned with each of these polarisation states respectively, the first prism should have no effect on the light, turning the system into an equivalent to a single prism simulation with a reduced incident intensity. Despite this, Figure 6.8 shows the resulting pattern at 0° incident polarisation that should not have been occurring.

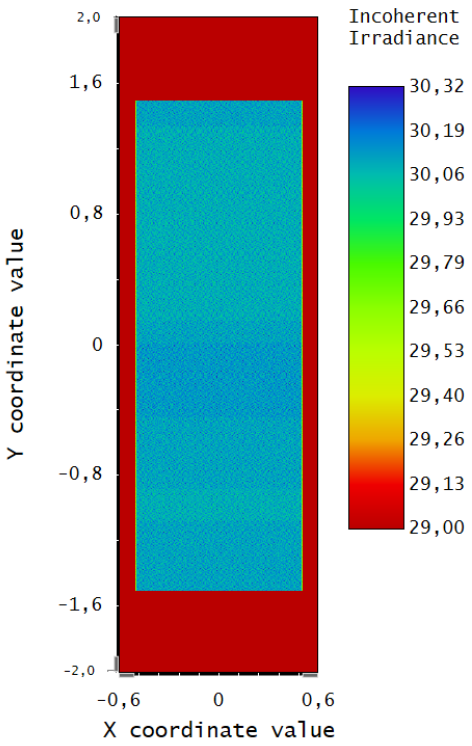


**Figure 6.8:** Ghosting pattern seen with 0° incident polarisation.

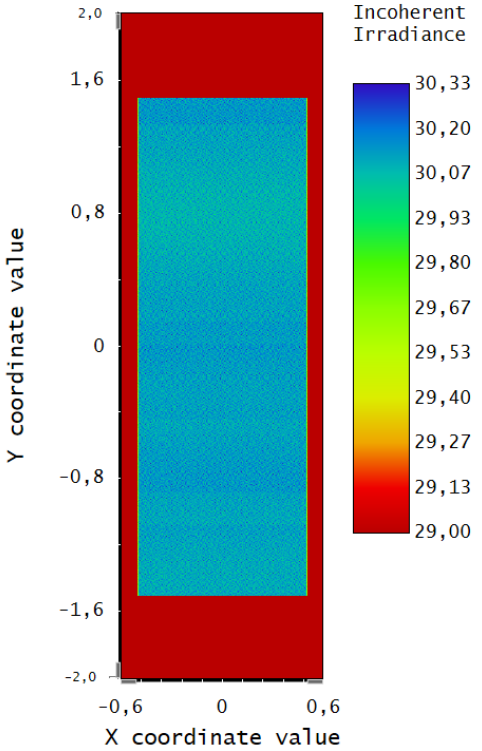


**Figure 6.9:** Ghosting pattern seen with 45° incident polarisation.

The pattern was also visible in the case of 45°, overlapping with the expected fluctuation which should be visible as seen in Figure 6.9, though it is difficult to distinguish in the ZEMAX detector plot. The area between 0 and the -0.8 y-coordinate value shows the highest contrast, though at +0.8 and throughout the detector the same behaviour can also be seen.

The first step taken in figuring out what the issue might be was moving the detector up and down to observe the movement of the pattern. In Figure 6.10, it is visually clear that the pattern does not seem to change with source and detector placement.

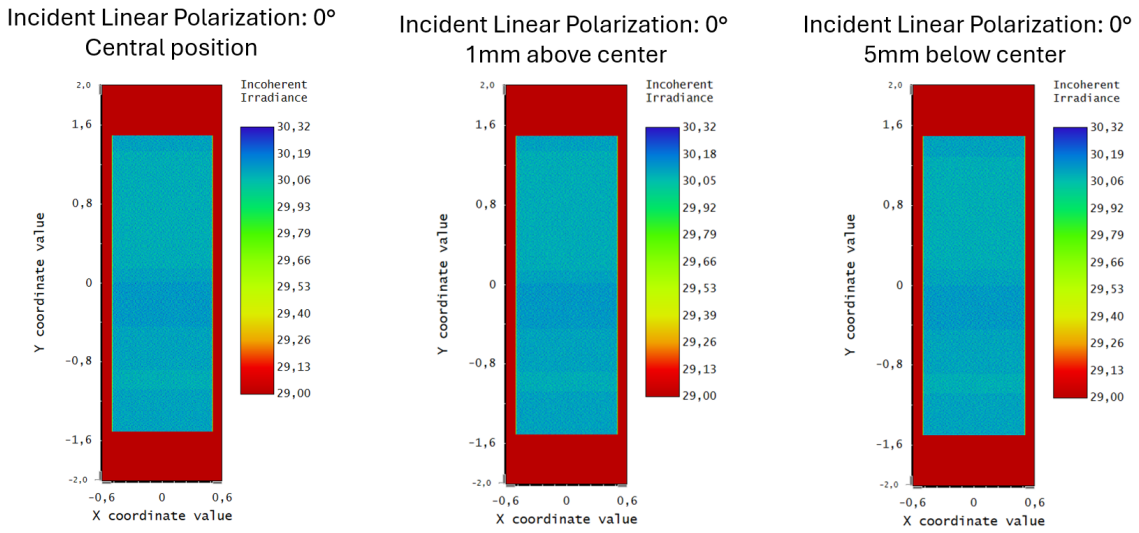


**Figure 6.10:** Comparison between the Ghosting pattern at different source and detector locations.

Plotting the 0° case against the same simulation with the source and detector at a 5mm offset gives Figure 6.11 where it can be concluded that any differences are due to noise and not inherent differences in the pattern itself. Furthermore, to demonstrate how far apart the detector locations are from each other, Figure 6.12 and Figure 6.13 show the two simulation layouts from ZEMAX. For each change in the detector, the source was also changed as there was no need to increase computation time by simulating rays which would not reach the end detector.

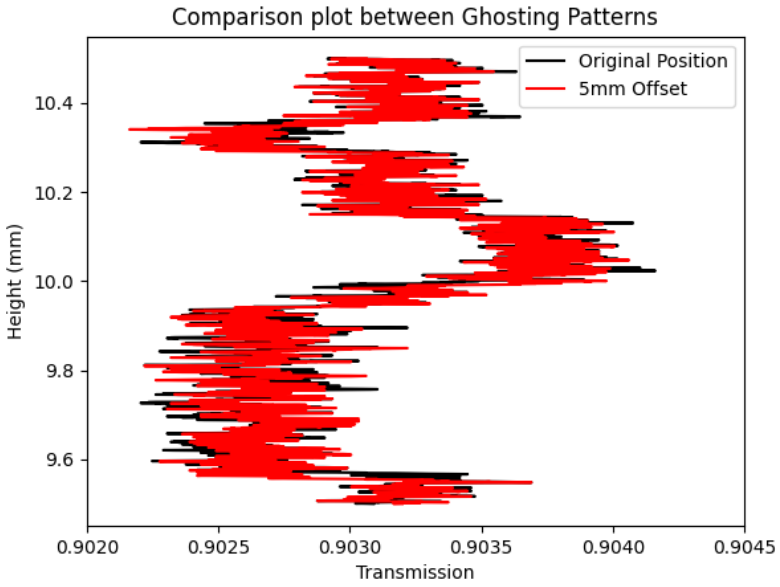


**Figure 6.11:** Comparison plot of the ghosting pattern at the regular position compared to the 5mm offset simulation at 0° incident polarisation.

The detector and source were also changed in size to see if the pattern was caused by the detector itself or was the result of the ray tracing itself. Upon making the detector smaller, rather than the pattern appearing again in full across the reduced detector height, instead only a reduced portion of the pattern was visible.

From this, along with the extremely artificial appearance of the step function-like behaviour, it was determined that the likely cause was the ray tracing ZEMAX was performing and not the detector. The source was also verified during the process to ensure that there was no strange pattern in how the rays were distributed. No such pattern was observed.

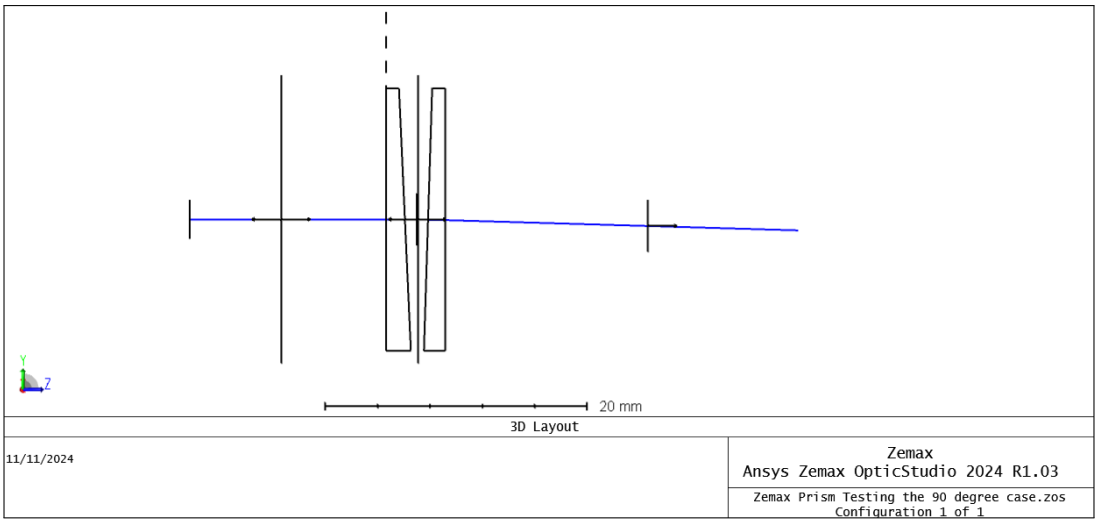


**Figure 6.12:** Normal position of the source and detector.

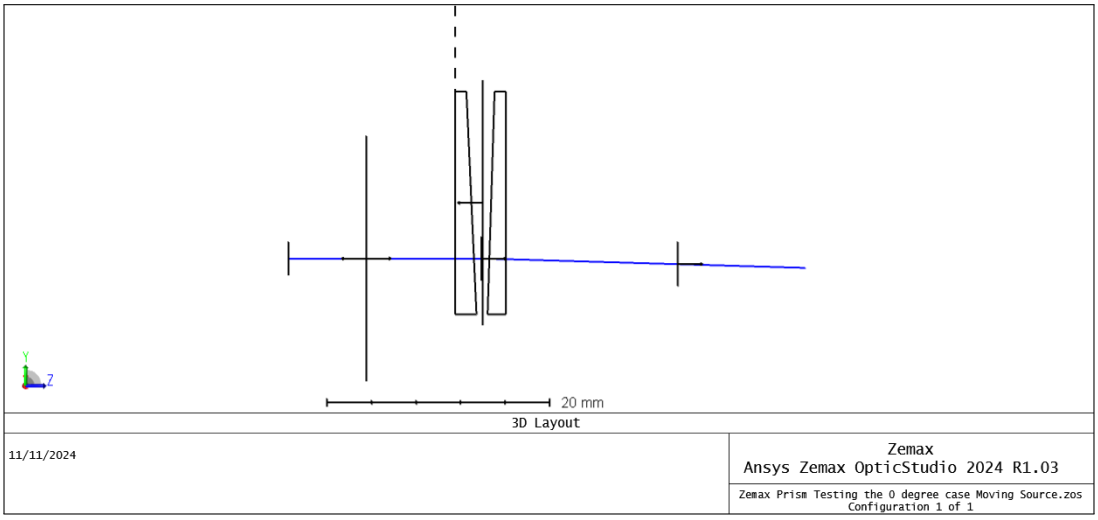


**Figure 6.13:** 5mm Offset position of the source and detector.

**Explanation**

After various attempts were made to try to understand the cause of the pattern, it was established that ZEMAX itself was the culprit. This meant that the pattern had to be removed from the results in order to obtain the true intensity pattern which would be useful in verifying the Python models from chapter 5. However, without knowing the exact ray tracing issue which produced these results, there was a fear that the pattern could cause different and possibly harder to detect discrepancies in future simulations. Because of this, some advice was requested from TNO where a ZEMAX specialist was contacted. With their assistance, the nature of the step-like pattern was determined.

The cause of the pattern is 'ghosting'. To explain ghosting, use will be made of diagrams both created for this explanation and some provided by Mr. Rob Vink from TNO. To begin with, in order to explain the ghosting effect, the first thing which needs discussion are the ray paths. If a single ray is considered rather than the full array of rays from the source, it is possible to trace the ray through the entire modulator. Figure 6.14 portrays the first ray as it passes through to the detector along with a visual representation of the intensity peak created by this ray.

If some possible internal reflections of the ray are now considered, in which the ray bounces twice such as in Figure 6.15, the twice reflected portion of the ray now travels out of the prism elsewhere along the height of the prism, possibly intersecting the detector again. This process can be performed for any of the many possible reflections which all result in some transmitted output.

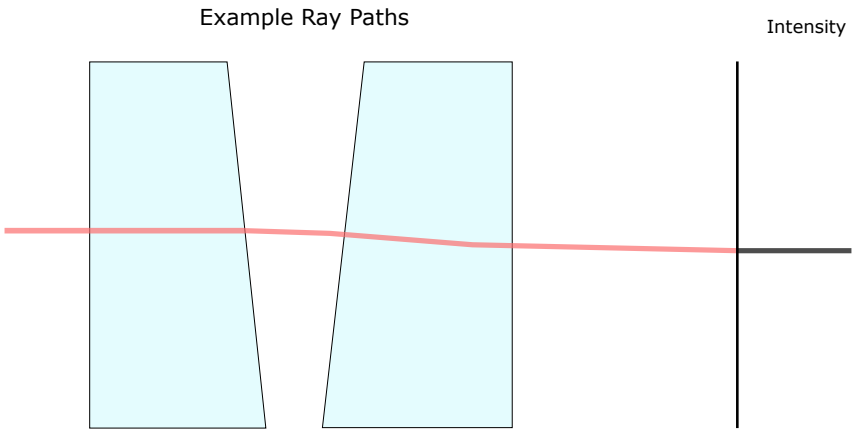


**Figure 6.14:** Figure showcasing an example ray path through the prisms and a visual representation of the intensity spike this ray may cause on a detector. The figure is not to scale.

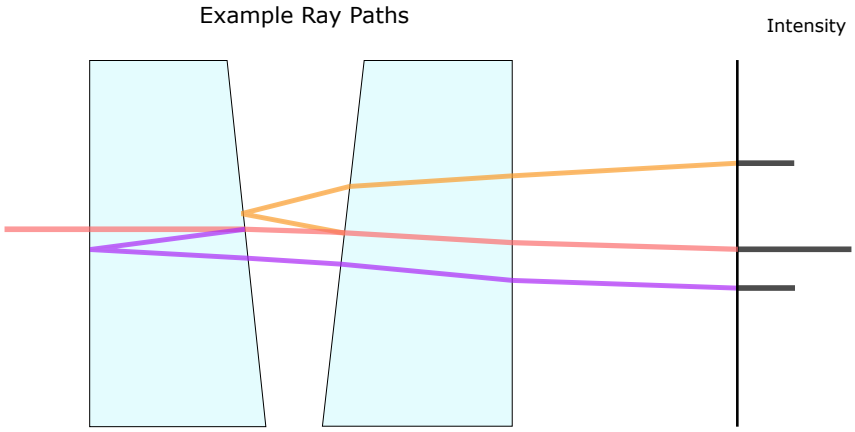


**Figure 6.15:** Example of ray internal reflections (orange and purple) resulting in additional intensity spikes on the detector.

To further clarify the cause of the ghosting, it is also necessary to consider the incident rays parallel to the ray which has been considered this far. In Figure 6.16, some of the rays exiting the source and travelling parallel to each other through the modulator are shown. All rays in the diagrams are considered as having either 0° linear polarisation states, meaning that all rays will output the same intensity. If instead of a small, discrete number of rays, all rays were considered and their respective intensities, the intensities create a 'block' of equal intensity on the detector.

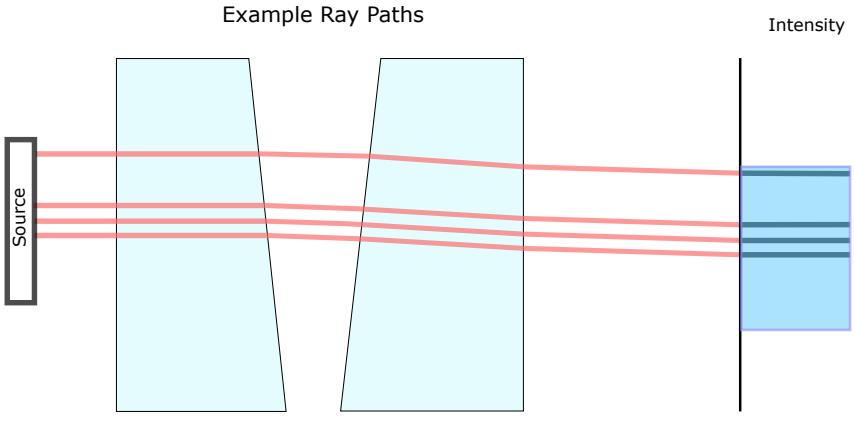


**Figure 6.16:** Representation of a 'block' of equal intensity created from all of the rays travelling parallel to each other through the modulator.

The same 'block' behaviour can also be generated for all of the rays travelling parallel to each other while also bouncing off the same boundaries. This results in Figure 6.17 where the blocks have been drawn on to represent all of the intensity peaks caused by the rays following the same paths. For clarity, the blocks have been outlined in the colour corresponding to the ray path.

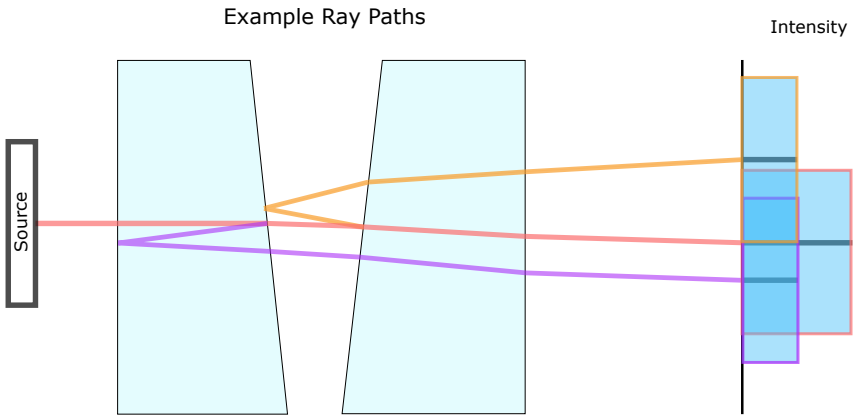


**Figure 6.17:** Representation of blocks for some example ray paths. The boxes produced by parallel rays following the same paths have outlines coloured based on the 'path' which produces them. Where more of these boxes overlap, the cumulative intensity increases.

Such blocks are also represented by Mr. Rob Vink in Figure 6.18 where the x-axis is the location along the height of the detector at which intensity spikes occur, and the y-axis is the intensity. In this figure, more of the paths are represented.

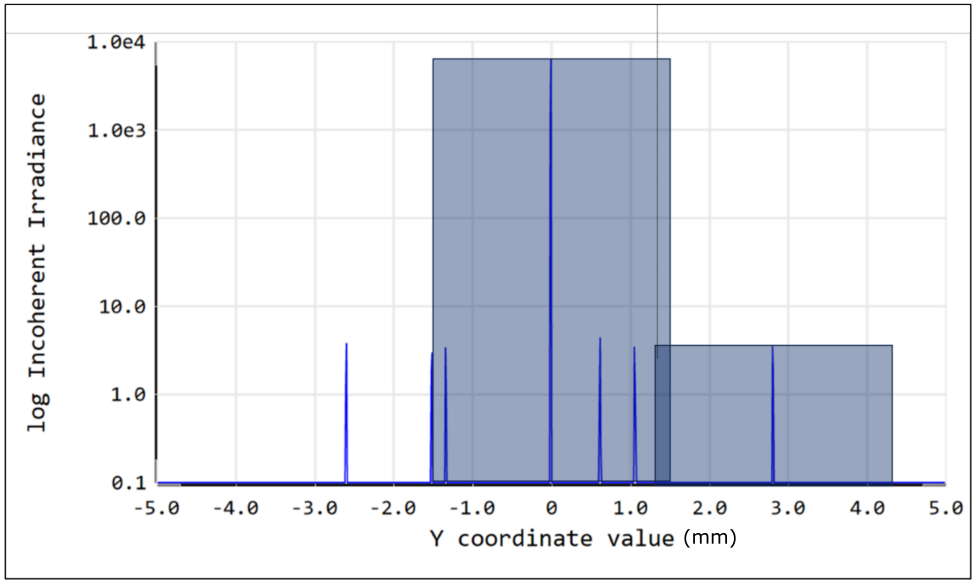


**Figure 6.18:** TNO provided figure showing the intensity spikes caused by different possible ray paths originating from the same incident source, and of the blocks representing the intensities of all other parallel rays.

If the process of creating these 'blocks' is performed for each individual sequence of internal reflections and for all sets of rays following the same parallel paths, the blocks begin to overlap significantly, as different blocks occur in different locations when exiting the last prism. Mr. Vink showcases this in Figure 6.19. In this figure, the original detector result is given in the background, along with all of the 'blocks' for different ray paths being overlaid on top. The original detector result aligns with the block produced by the ray path which directly transmits with no internal reflections. This block is also the tallest as the lack of reflections along this path means less intensity is lost as the ray propagates. The lower incoherent irradiance blocks all represent the blocks of different ray paths which reflect off at least 2 surfaces before transmitting towards the detector.

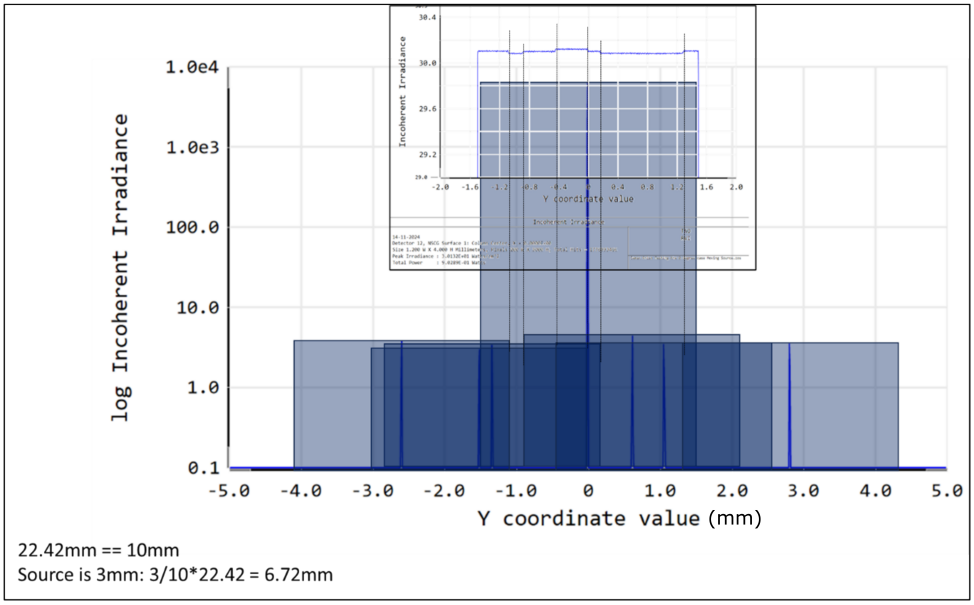


**Figure 6.19:** TNO provided image showing all the blocks for every ray path, along with the ghosting pattern observed on the detector in the smaller graph at the top. The ghosting pattern above and the intensity pattern below are aligned to correspond to their relative positions.

The first observation is that the blocks are not limited only to the detector surface even though the source is the same size as the detector. This is easily explained by the diverging angles of reflection depending on the sequence of boundaries on which the ray bounced. The more important observation is how the detector pattern matches perfectly with the overlapping blocks. In areas with higher degrees of overlap the detector shows a higher intensity output. In areas with less overlap the intensity is lower. Essentially, the step functions observed in the detector are caused by the cumulative summation of the different intensities of these blocks at a certain location. As the incident light polarisation is 0° in the example used, the pattern is not caused by any Fresnel behaviour and can therefore be directly correlated to the cumulative intensities as discussed.

While ghosting is a phenomenon which can occur in real laboratory conditions, such effects were not observed in previous experiments, nor in the validation experiments which will be discussed in chapter 7. It is likely it is more prominent in ZEMAX due to the smaller scale of the source relative to the modulator size than is used in a lab. In the lab, the source is larger and distributes rays across the entire modulator surface resulting that the effect of specific reflection 'blocks' are significantly reduced to the point they are not distinguishable. Therefore, as the source is small in the simulation to densely pack the rays without reducing computation time, this ghosting is a consequence which has to be dealt with.

**Removal Process**

To remove the effect of the ghosting, the ideal process would be to isolate the ghosting effect on each individual output and then simply compensate by subtracting that same pattern from the detector output. Unfortunately, such a trivial solution is hindered by the transmission pattern which appears at incident polarisation states which do not align with the first prism fast or slow axes. The superimposed patterns make it difficult to inherently remove the ghosting from the result directly. One method to remove the ghosting would have been to remove all internal reflections in ZEMAX, however, as the internal reflections cannot be removed in a lab experiment, it was preferred to maintain these to obtain a better comparison with experimental results.

Instead, the method applied for removing the ghosting for the 45° incident polarisation case, is to take the outputs for the 0° and 90° cases and calculate the average value of the transmission for each of them. Doing so showed that the pattern was exactly identical with the exception of noise and a slightly shifted average value. Because the inherent pattern remained the same, it was assumed that it would once again maintain the same distribution around the average value when the incident polarisation was changed to 45°. The 45° results were then taken, the pattern was removed as if at 0° incident polarisation, and the average value was then re-adjusted to compensate for the fact that, at 45°, the average value should be between the 0° and 90° cases.

As a demonstration of the average being in between the two alternative cases, Figure 6.20 shows the 3 different incident polarisation cases side by side. The values of incoherent irradiance of the detector pixels were divided

by the maximum incoherent irradiance of the source which in these cases was $33.33 W/cm^2$. From the incoherent irradiance values, the 45° case is approximately half way between the 0° and 90° results. The sinusoidal fluctuations caused by the Fresnel behaviour, which was being investigated, slightly alter the maximum and minimum values of the results but the average was taken as being halfway nonetheless.

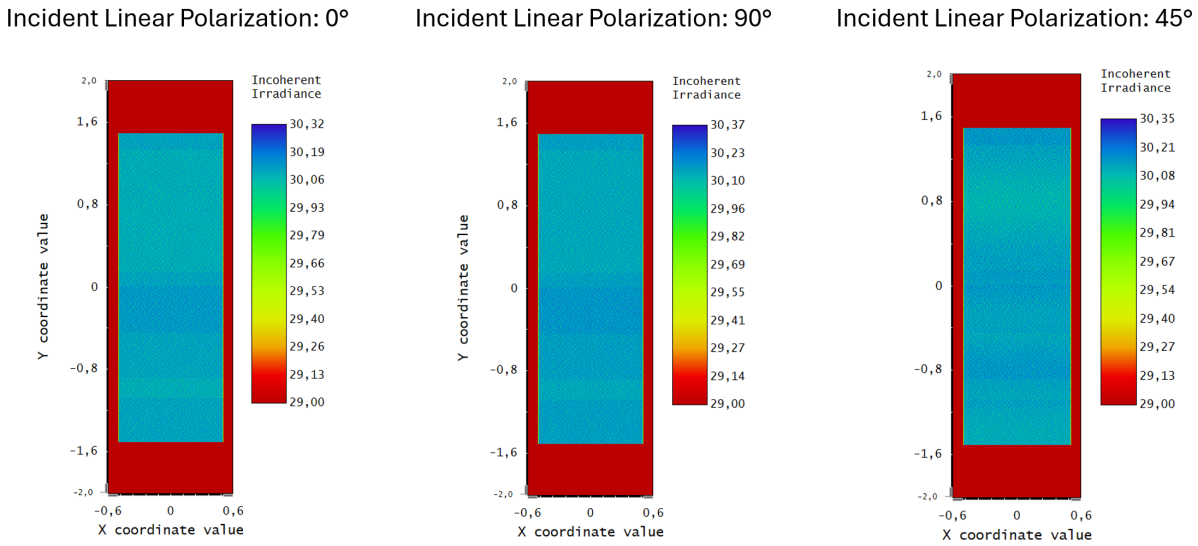


**Figure 6.20:** Comparison between ghosting plots using different incident polarisation orientations.

## 6.4. Results

In this section, the results of the ZEMAX simulations will be discussed. In addition to the results themselves, it was decided to compile the method for obtaining the results here as well. This entails explaining the process of taking the ZEMAX data and turning it into the final graphs, along with the rolling mean to reduce noise, and the integration of the ghosting removal process.

### 6.4.1. How the Results are Obtained

In terms of how the results are obtained and then plotted, ZEMAX provides all detector data from simulations as a text file. This text file holds information for each pixel and its respective incoherent irradiance in the detector. Additionally, information is saved regarding the file name, date, which detector, the size and pixel count of the detector, the total hits on the detector and various positional details regarding how the detector is oriented in the simulation space. This text file is easily convertible into a csv file using common applications such as excel where the data can be imported and then exported to properly transform the file from a text file with no delimiters into a csv file which can be read in Python.

Once the csv file has been acquired, a Python script was created in order to read the data. Due to the quantity of data and because of how long new simulations take to run, the script was made to give a sufficiently clear overview of the csv data without causing further delays when large quantities of pixel values have to also be investigated. As such, the script at this time only takes one column of data which is then saved to be plotted. Each value of the chosen column, which is the central column at the middle of the detector, has a value corresponding to the incoherent irradiance. To get the percentage transmission instead, and therefore be able to compare with the Python Jones model, the detector placed right after the source is also taken into consideration. As the source is homogenous, the incoherent irradiance should be the same for every pixel. By checking the detector just after the source, the incident irradiance can be obtained. The division of the output values by the value from the source gives the percentage transmitted through the prisms.

As the detector is usually larger than the area which actually detects any light, the csv data is trimmed to remove pixels with values significantly lower than expected. The data is briefly looked through to see what the approximate incoherent irradiance values are, after which all values below the values seen in the region of interest are removed entirely.

Once the desired pixels have been selected, it is also required that they all are assigned to the correct locations along the height of the modulator. To do this, the source is taken as reference rather than the detector position.

The reason for this is that the Python model does not account for ray displacement, meaning that for a proper comparison, the results need to be adjusted slightly to align them with the Jones model. As the csv includes only pixel details and not specific heights, the way in which the heights are assigned is by looking at the detector area which remains after the trimming of undesirable pixels, and then noting down the start and end points of the area of interest. This area is then divided by the number of pixels along its height to get the height of each respective data point.

The resulting plots at this point often look noisy and unclear. A trend can be seen from the results, however, the precise pattern is difficult to discern. Options for reducing the noise have to be considered at this stage to be able to actually understand the data properly. One of the options to do this would be to average the data across all of the different columns. However, at the moment when the noise reduction was implemented, there were still concerns regarding having to plot graphs for many simulations, and therefore the time required to adapt the code for this was not available. Instead, it was decided to attempt a 'rolling mean' noise reduction.

**Rolling Mean**

A rolling mean entails taking the data points to the left and the right of the data point which is being adjusted (or in this case the data to the top and bottom). The data point and the values of the data points to either side are all summed together and then divided by the total number of data points used to give the mean of the data as the new value. The 'strength' of this noise reduction method is based on the degree of approximation used. This degree of approximation essentially establishes how many data points are used on either side. With a degree of approximation of 10, it would mean using 10 values on each side resulting in 21 values total when including the original data point. At points closer to the start or end of the list than the degree of approximation allows, all values available are used to get as close to the same number of values as possible, but this does inherently cause a loss of precision in the data near the end points of the set.

Another consideration which needs to be taken into account is the fact that a larger degree of approximation brings all of the results closer to the same mean value. If the degree of approximation is raised too high, the true 'shape' of the data will be lost. If the value is too low, on the other hand, the data will not have reduced the noise sufficiently to a point where the data can be properly analysed. As the data sets from the simulation have 3000 to 6000 data values along a single column depending on the simulation, this limitation does not cause problems as the degree of approximation used normally only varies between 5 and 30. Even accounting for the data trimming which is performed, the degree of approximation is always maintained below a hundredth of the data set on either side of the data point. Furthermore, the degree of approximation is visually selected by selecting the minimum degree of approximation at which the noise no longer impedes the analysis of the amplitudes and period, which means it is often lower.

As an example of how the different degrees of approximation affect the results, a data set obtained during the testing of the ZEMAX prism ray tracing mode will be used. Originally, the data used a degree of approximation of 10 with a remaining pixel count. In Figure 6.21, the plot can be seen in its original form, with a degree of approximation of 2 and with the same degree of approximation of 10. The difference the choice in degree of approximation makes is even clearer when looking at a 0° incident polarisation ghosting pattern with a 3mm source size as seen in Figure 6.22.

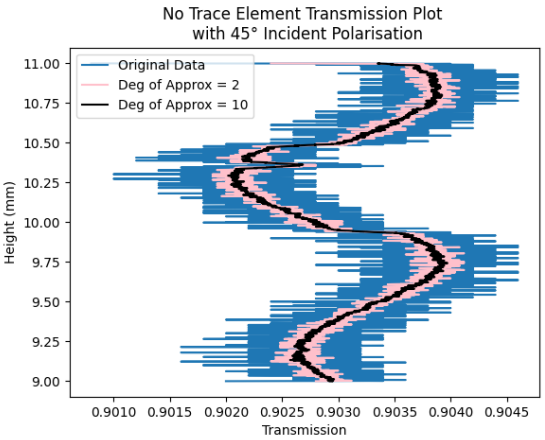


**Figure 6.21:** No Trace element plot with varying degrees of approximation in their rolling means.

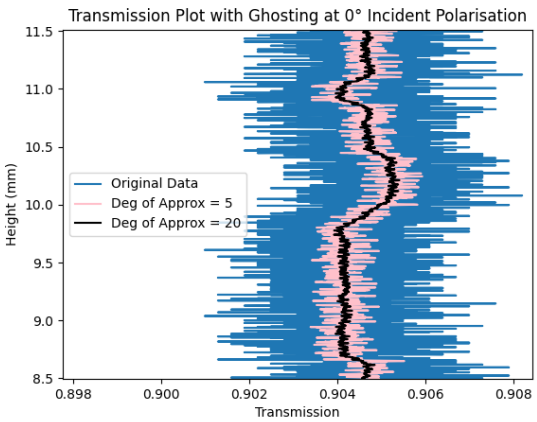


**Figure 6.22:** Ghosting Pattern as seen at 0° incident polarisation from a 3mm tall source.

The final plots used to investigate the fluctuations as simulated by ZEMAX all had approximatively the same number of data points, and, therefore, all only needed degree of approximations of 20 prior to further data analysis such as the removal of ghosting effects.

**Ghosting**
After the rolling mean has been implemented, the ghosting removal process also had to be included. This has already been described in broad terms in subsection 6.3.3, but it is still worth mentioning that the ghosting removal is done prior to applying any rolling mean. The original data set is used, the ghosting pattern is then subtracted from the data set, after which it is trimmed and plotted. The rolling mean is performed for clarity in the figure, and to analyse the outcomes. Removal of the ghosting came with an unexpected benefit in the form of removing a substantial part of the noise. The simulations all have similar noise distributions which results in the noise almost entirely cancelling out when the ghosting pattern is subtracted from the simulation. This had the fortunate benefit of reducing the degree of approximation on the ZEMAX results from 20 to only 5, therefore significantly reducing the degree to which the rolling mean affects the results.

### 6.4.2. ZEMAX Simulation Results

In terms of the simulation results themselves, the different outputs will be shown here. Much like in the Jones model results section, subsection 5.2.4, the 0°, 45°, 90°, -45°, and right hand circular polarisation cases are all shown. For the final simulations, the parameters given in Table 6.3 were used. To begin with, for the 0° and 90° linear incident polarisation cases, as the ghosting removal process essentially uses the 0° and 90° results, removing the ghosting from these particular cases just gives the average value of the plot instead.

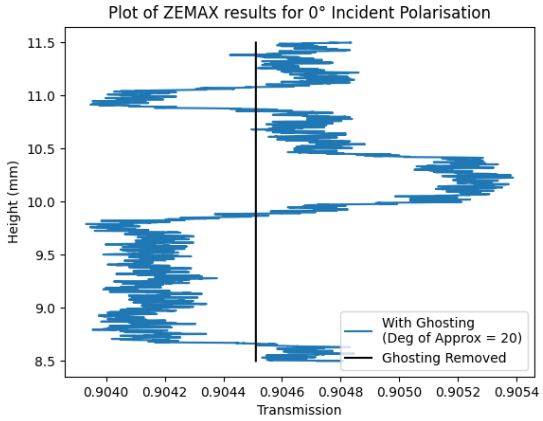


**Figure 6.23:** ZEMAX simulation results for a 0° incident polarisation using a 3mm source. The results both with and without ghosting are included.

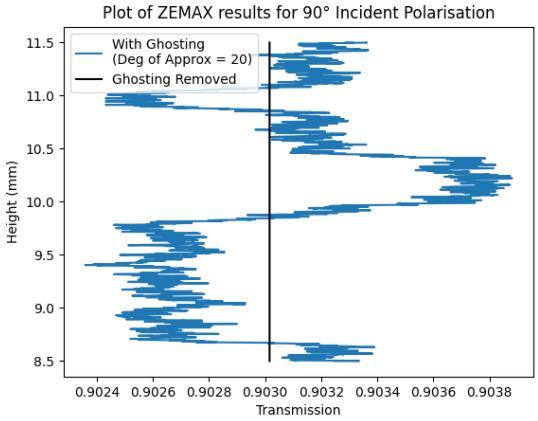


**Figure 6.24:** ZEMAX simulation results for a 90° incident polarisation using a 3mm source. The results both with and without ghosting are included.

For the simulation of 45° incident polarisation, the plot, as shown in Figure 6.25, originally presents an inconsistent pattern from which it is difficult to distinguish the ghosting pattern from the expected intensity fluctuations. In previous examples and iterations of the simulation, such as Figure 6.21, the source and detector were smaller and a clear sinusoidal pattern was visible without any large effect from ghosting. With the final source and detector parameters, however, the pattern, is greatly affected by ghosting. This is because the size of the source and detector both directly correlate to how prominent the ghosting is. The larger the source and detector become, the more ray paths which can result in overlapping intensity 'blocks'. As the ghosting patterns for the 0° and 90° cases have already been shown in Figure 6.23 and Figure 6.24, it is fortunately possible to remove the ghosting from Figure 6.25.

Once the ghosting is removed from the plot by the means discussed in subsection 6.3.3, the plot transforms into a clear intensity fluctuation pattern with very little noise. This is seen in Figure 6.26. The same process can be performed for the -45° case leading to Figure 6.27. The sinusoidal pattern obtained after the removal of ghosting is in line with the shape which would be expected from the Fresnel phenomena induced fluctuations being investigated.

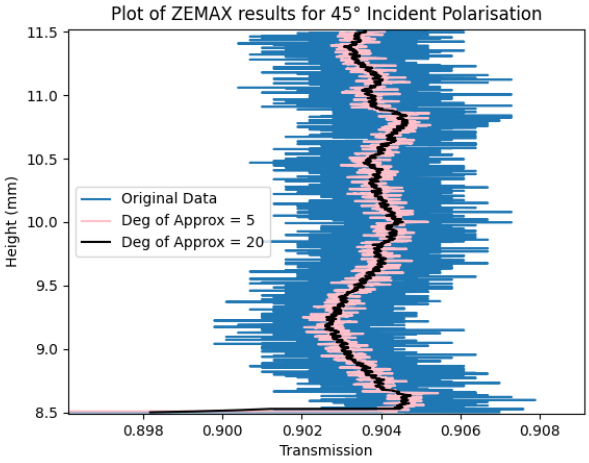


**Figure 6.25:** ZEMAX simulation results for a 45° incident polarisation using the same 3mm tall source as the 0° and 90° cases. Ghosting has not yet been removed.

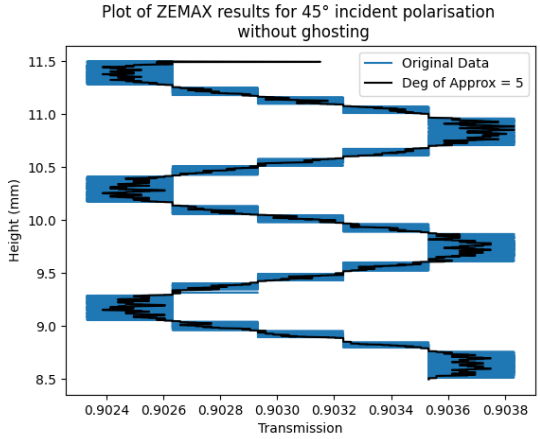


**Figure 6.26:** ZEMAX simulation results for a 45° incident polarisation. Ghosting has been removed and only the fluctuations are now visible.

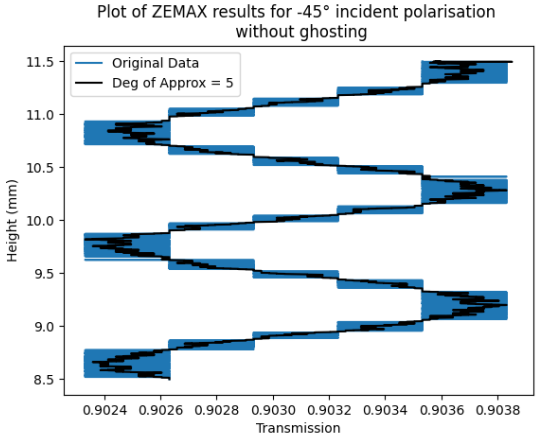


**Figure 6.27:** ZEMAX simulation results for a -45° incident polarisation. Ghosting has been removed and only the fluctuations are now visible.

The same method is also applied in the cases of left or right hand circular incident polarisation. To demonstrate this, the right hand circular results are shown in Figure 6.28. Left hand circular incident polarisation returns the same results but mirrored and therefore is left out as all conclusions from right hand circular are also applicable to left hand circular polarisation.

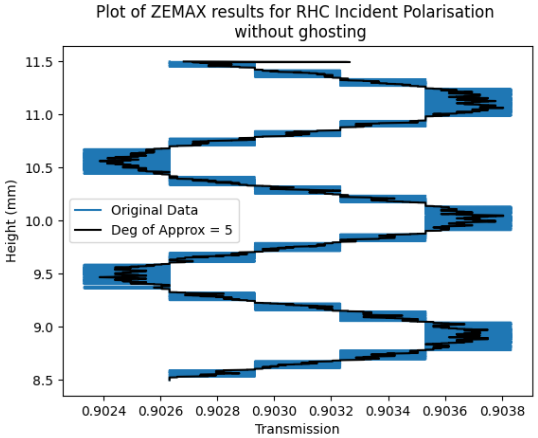


**Figure 6.28:** ZEMAX simulation results for a right hand circular incident polarisation. Ghosting has been removed and only the fluctuations are now visible.

### 6.4.3. Initial Comparisons with models

As a first round of verification of the simulation, it can also be compared directly to the Jones model created in Python. To begin with, the 0° and 90° cases are found in Figure 6.29. Both orientations of the incident polarisation are given together to show the general differences between both the methods and the choice of polarisation orientation. For the 45° case, the results are shown in Figure 6.30.


**Figure 6.29:** Comparison of the Transmission plots from Jones and ZEMAX at 0° and 90° incident polarisation orientations.

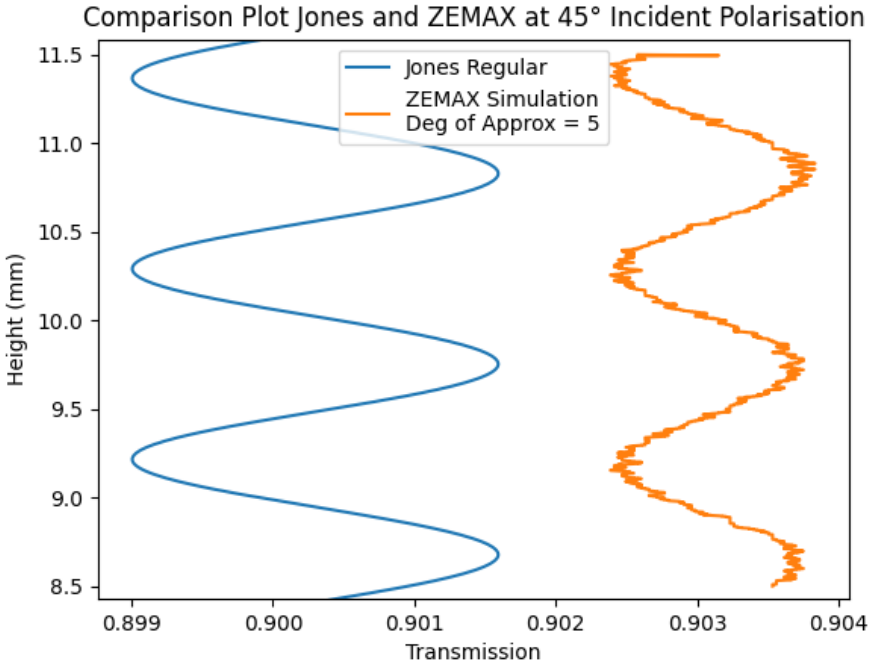


**Figure 6.30:** Comparison of the fluctuations between Jones model and ZEMAX simulation for the 45° incident polarisation case.

The -45° case is presented in Figure 6.31 where the results are essentially mirrored across the average transmission once again.


**Figure 6.31:** Comparison of the fluctuations between Jones model and ZEMAX simulation for the -45° incident polarisation case.

It is immediately evident that the fluctuations resemble each other and share some similarities, such as the period, but still prove to give distinct results in terms of not only the expected average transmission but also in the amplitude of the fluctuations. To further investigate how the two plots compare, the periods and amplitudes were calculated to the closest degree possible using the rolling mean ZEMAX plot and the Jones model results.

**Similarities**

From this investigation it was found that the period of the ZEMAX simulation plot is approximately 1.087mm with some slight variation of ±0.01 depending on what was considered the 'peak'. This is extremely close to the 1.08mm calculated for the Jones model previously. The peaks also appear to align across the model and simulation, though the remaining noise makes specifying the exact peak difficult. Taking an approximate location for the peak suggests they are within 0.05mm of aligning if a generous margin is considered. This margin also suggests that the period difference is within this same margin of error as a slight misplacement of the peaks may result in a ±0.1mm period.

Any deviation between the two graphs in terms of their height can be explained by the ray tracing of ZEMAX not following a perfect linear path to the detector as the rays interact with the prisms. While it was attempted to align them based on the original source position, this does not entirely resolve the issue fully. Even so, the graphs demonstrate that both ZEMAX and Jones are expecting the same fluctuation periodicity and approximate peak and valley positions when Fresnel phenomena is added, hence verifying that Fresnel phenomena are a clear contributor to the behaviour seen in section 3.2.

**Limitations**

In terms of the differences between the two plots, the average transmission could be due to the assumptions made in the Jones model such as not including internal reflections which still hit the detector, or due to the method in which the Fresnel coefficients are calculating predicting that more light will reflect somewhere along the modulator.

For the amplitude difference, there are fewer indications as to the cause. Potential reasons for the lower amplitude shown in the ZEMAX results could, again, stem from the method in which the Jones model calculates the boundary conditions as the s and p components of the rays are separated entirely from one another. It is possible that the simplification where the Jones model treats the p component as only interacting with $n_p$ and the s component only interacting with $n_s$ is not sufficient to represent the actual refractive indices which the

ray experiences. As the Jones model treats the light ray as passing through the entire modulator horizontally, the angles of refraction caused by each boundary are not considered. For ZEMAX, on the other hand, the light ray coordinate system will not align with the prism fast and slow axes once the ray is refracted. The Jones model therefore assumes the light experiences the fast and slow-axis refractive indices at an ideal angle, while the ZEMAX refractive indices which the ray experiences are actually closer together. This difference in the material properties may account for the difference observed in the graph.

Essentially, while the specific method by which ZEMAX models the material, especially along axes not corresponding to the fast or slow axes of the material, is not readily available, the calculation is more complex than what is performed in Jones. Therefore the material properties are not treated as either the maximum or the minimum refractive indices, but rather varying refractive indices in between. This could then explain why the difference in the peaks and valleys is smaller than in Jones.

Finally, the overall effect of using the waveplate mode and not including the trace elements at all is not yet entirely understood. From the results of the investigation in subsection 6.2.2, it was observed that the trace element at the end of the prisms appeared to increase the overall amplitude of the plot while maintaining the period and position of the peaks. Images of these results are found in Appendix C. It is possible that performing the simulations with the element re-added may give results closer to the expectation, however, the presence of ghosting effects was also observed to be greater in the results. It is therefore unclear if the increase in amplitude when the trace element is added is a result of the method being more accurate, or simply because the addition of this element enhances the ghosting effect by splitting every original ray path into ordinary and extraordinary rays.

# 7

# Experiment

In this chapter, the experiment performed for the validation of the models and simulations is reviewed in detail. Within the chapter, a detailed explanation of the objectives, method, and results of the experiment will be provided such that a complete overview of the steps taken can be obtained. These can be found in section 7.1, section 7.2, and section 7.3, respectively, together with limitations of the experiment provided in section 7.4.

## 7.1. Experimental Goals

After the final versions of the models and the simulations were obtained, and some initial comparisons were made, it was also necessary to validate the results. Performing experiments would provide a deeper understanding of why the models created in Python do not fully coincide with the simulation results, and how they compare to real world behaviour.

The main objective of the experiments was to obtain lab results for each of the main model and simulation cases. This can then allow for a full comparison at each of the main incident polarisation cases.

To achieve proper validation of the previous results and properly establish what the experiments should consist of for a complete set of data, the experimental sub-objectives must first be established. This means listing each case which requires particular investigation and planning how to procure the results as needed.

The main polarisation states which are of particular relevance to the thesis investigation into Fresnel transmission and reflection behaviour are the 0°, 45°, 90°, 135° and either Right or Left hand circular polarisation. At these incident polarisation states, measurements must be taken to obtain the fluctuations as observed by the camera after the light passes through both prisms. Additionally, for comparison with previously discussed models and simulation results, it is also necessary to be able to obtain the fluctuations as a percentage transmission of the original source light.

## 7.2. Method

In this section, the experimental setup and methods are discussed along with the considerations made when choosing to perform the experiments as stated. The characterisation of key components and the measurements which were taken are also reviewed.

### **7.2.1.** Setup

The setup used in the experiments is designed to resemble as closely as possible the models and simulation which were created for this thesis. As such, it necessitated some key considerations to be taken into account.

In Figure 7.1 a simplified diagram which shows the different components and the order they are placed in can be found.

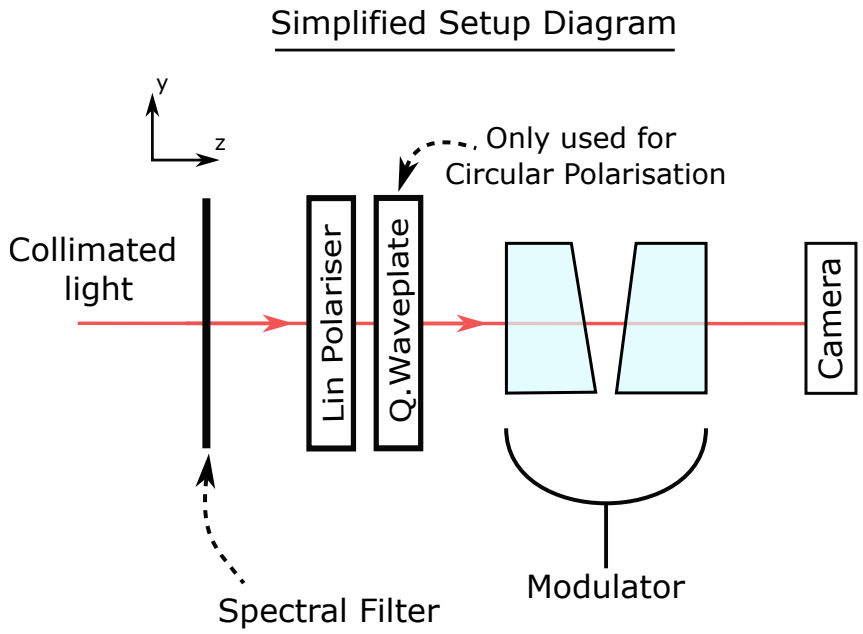


**Figure 7.1:** Simplified diagram of the setup components.

First of all, the incoming light into the modulator prisms had to be manipulated in order to match the sources used in the simulations and models. The source available in the lab was a white light source. This white light source is then collimated to ensure the rays are all parallel as they pass through the setup.

To match the experimental light wavelength with the wavelength used in simulations and models, a spectral filter is placed between the light and the rest of the setup. For the sake of ease of use, and due to the equipment being in use by other members working on the modulator, it was decided to set the spectral filter to a pre-existing setting. The setting selected was the closest option available to the wavelength already in use in the models. It did, however, mean that the models and the simulations would have to be altered for a true comparison.

This is then followed by a linear polariser in a rotating mount and a removable quarter waveplate in its own rotatable mount such that any desired polarisation state can be obtained.

Having achieved the means to recreate the simulation source, the next part of the setup revolves around holding the modulator in the correct spot. For this purpose, a stand with 2 clamps is used. A prism is placed in each clamp to recreate the modulator from the models. Due to physical limitations involved in working with 20mm tall, 1mm thick, extremely delicate prisms, these are placed on their side instead of vertically. The spacing between the prisms is noted for further adjustment of the simulations for a closer comparison.

Finally, the last component is the camera used to take all of the images from which the data will be obtained. The camera is a FLIR Blackfly S and required adjustment of certain parameters to ensure the images were of a suitable quality. These are referred to in subsection 7.2.2.

There are also a couple of additional pieces of equipment used for additional important steps that are not used in the main measurements. These include a beam splitter, opaque black plastic sheet, and, of course, an opaque surrounding box to prevent exterior light and stimuli from affecting the results.

A few images of the setup taken in the lab can be seen in Figure 7.2 and Figure 7.3. These images were taken after the experiments, and therefore represent the layout more-so than the exact position of each specific element.

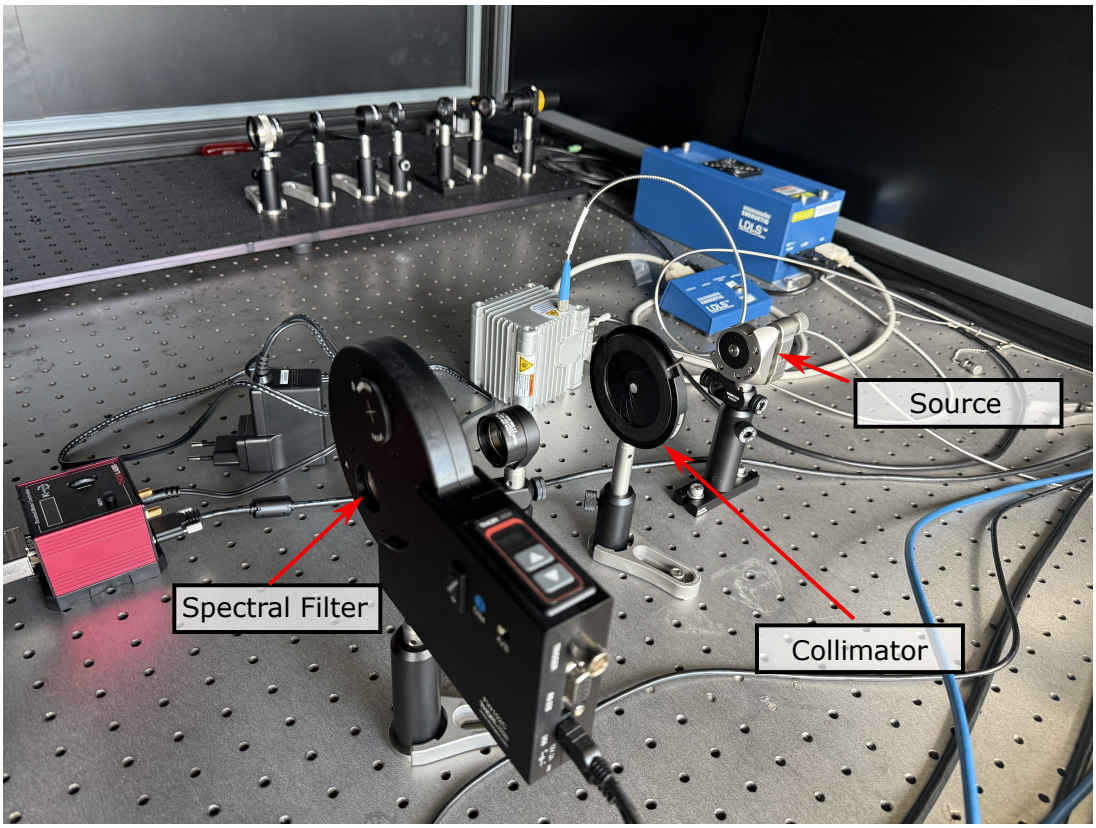


**Figure 7.2:** Photograph of, from right to left, the source, collimator and spectral filter.

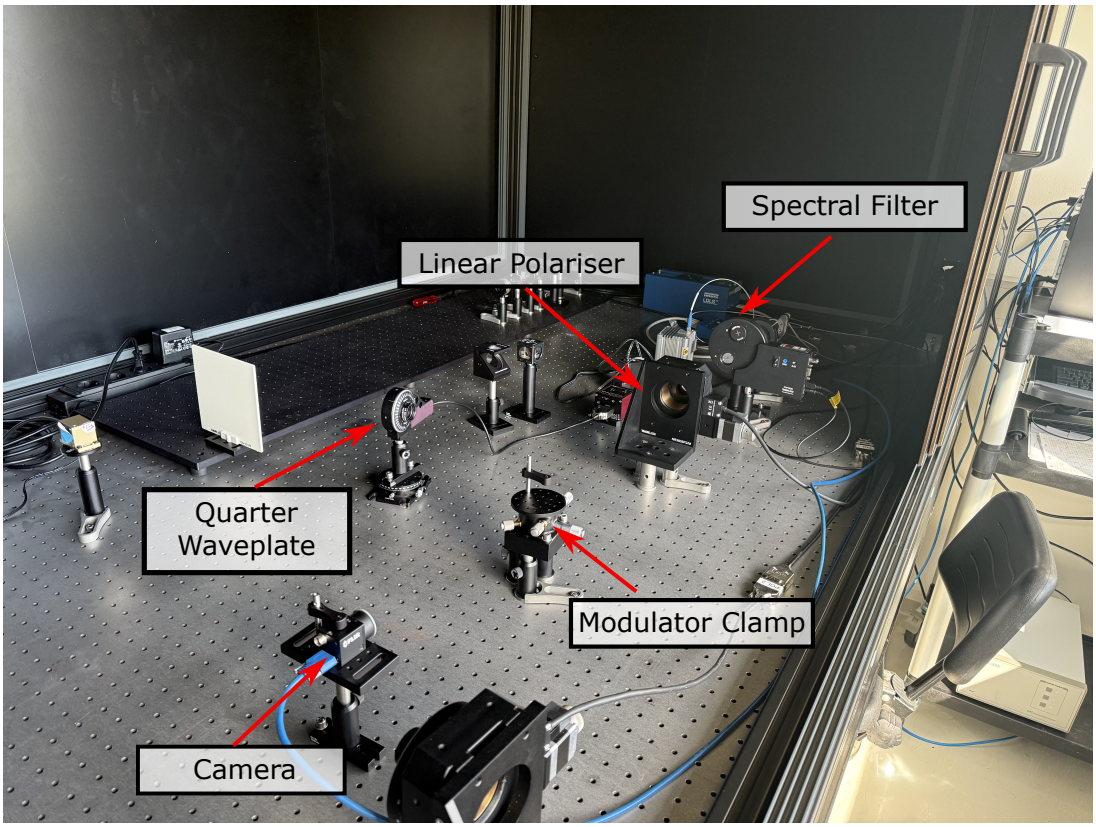


**Figure 7.3:** Photograph of the Setup taken from the Camera side towards the source. The camera, modulator stand, linear polariser and spectral filter are all visible in this order. The optional quarter waveplate is off to the side.

Note that the images of the lab setup in Figure 7.2 and Figure 7.3 show the setup from the opposite side compared to Figure 7.1 due to lab space constraints when taking the images.

### 7.2.2. Characterisation of Key Components

The method used to perform the experiments involves multiple mandatory steps to be taken both before, and after, the main desired results can be obtained.

As real components are vulnerable to errors in manufacturing and assembly, the first stage of the experimental process was calibrating the equipment. The very first part of the setup which requires calibration is the camera. The camera had to be able to provide images of sufficient quality before it was possible to continue working on component calibration. To do this, the camera settings are adjusted in Spinview, the camera specific app, in which all of the main parameters affecting image quality can be found. Among these settings, the most crucial are the gain, exposure and gamma settings, as enabling or disabling them changes the output significantly. These settings are originally set to standard values used in previous experiments on the same equipment, and are then optimised from there. In the case of the gain and the gamma settings, these were disabled for previous experiments and, based on the similarity in the measurements desired, they were left as such for this experiment as well. Some trial images were then taken with which to adjust the exposure time. An already existing MATLAB code was used in order to optimise the exact value for this parameter through observation of the signal output of the camera while the test images were being taken. The settings used in the end were:

- Auto Exposure: Off
- Exposure time: 12ms
- Integration time: 12ms
- Gain: Off
- Gamma: Disabled
- Pixel Format: Mono16

Once the camera was adjusted appropriately and produced images which achieved a satisfactory quality, the other components can be characterised as well.

The most important element to characterise is the linear polariser used to adjust the incident polarisation state entering the modulator. The reason this procedure is required is due to the possibility that the linear polariser is not perfectly aligned with the mount. It is possible that when the mount is set to align the polariser horizontally, for example, the actual polariser encased in the mount may actually be at a different angle. This means that there is no way to know what linear polarisation angle is actually entering the prism as the offset compared to the mount 0° axis is unknown.

The process of checking the offset angle between the true orientation of the polariser and the mount calibration requires the setup to be modified such that it includes a beam splitter before the linear polariser and no additional components to be added between the linear polariser and camera. Given that the beam splitter is known to separate exactly vertical polarisation from horizontal polarisation, allowing only horizontally polarised light to pass, it is possible to determine the orientation of the linear polariser compared to its mount based on the image produced by the camera. This method gave close approximate angle at which the linear polariser appeared to visually be exactly horizontal.

To properly get the exact mount angle corresponding to a 0° horizontal linear polarisation, the THORLABS motor controlling application, which is compatible with the mounts, is combined with a Python script allowing measurements to be taken at specified angles within a set range. As previous calibration data was available, the range was set to 176.76° ± 10°, where 176.76° was the previous calibrated 0° horizontal polarisation observed. The measurements were taken in step sizes of 1°.

Once the measurements for these values were completed, another existing code was used which use Malus' Law to allow for the checking of which point had maximum intensity. This point corresponded to the closest measurement to the polariser being at true horizontal. When the angle was found to be 174.76°, another set of measurements around this value were taken with steps of 0.1°. This same process led to a final value of 174.56 degrees as the true horizontal orientation of the linear polariser.

### 7.2.3. Measurements

Now knowing the angle of the linear polariser, it was possible to proceed with actual measurements for linear incident polarisation states. The beam splitter is thus removed from the setup and the modulator prisms are carefully placed onto the stand with two clamps between the linear polariser and the camera.

Once the modulator prisms are in position, the measurement taking Python script was adjusted to take actual measurements. For these measurements, the settings were adapted to perform measurements at every 0.1° ranging from 164.56° to 184.56°. The camera settings were left as 5 images per measurement with the same exposure and camera settings as previously used.

When the process was completed, the same was done again for linear polariser angles of 219.56°, 264.56° and 309.56° which correspond to linear polariser angles of 45°, 90° and 135°.

Before adding, moving or removing any components, as doing so would negate camera alignment and may alter how the light impacts the prisms, it was decided to take a wide spectrum of results as well. For this, the same procedure was used, except now in single degree steps ranging from 0.56° to 359.56°. The majority of these angles do not correspond to any model or simulations investigated to this point, but provide the option to review certain results and ensure they make sense. Furthermore, it may prove beneficial for future project developments and/or additional simulation comparisons if the results are unclear.

An additional final step was needed for the full completion of these linear polarisation measurements. This final step is to measure the 'dark' of the camera. What this entails, is to block off the direct light from the source. For this purpose, a black plastic panel was placed immediately after the source, effectively blocking direct line of sight between source and detector. A single measurement was taken with the same 5 image, default camera settings. The purpose of the 'dark' measurement is to measure the effect of internal reflections and stray light within the enclosing box around the setup. This would allow the possibility to compensate for additional effects and errors caused by these undesired light bounces, as well as any sources of light which are originating from outside the box and managing to enter through any small gaps in the encasing.

The next step after linear polarisation measurements were finally fully completed was the measuring of results for circular incident polarisation. To do this, the quarter waveplate had to be added to the setup. Much like the linear polariser, the waveplate requires calibration to ensure that the 0° angle written on the mount is also equivalent to the angle of the waveplate 0° angle as well. Normally, this involves removing the modulator prisms and adding another, second, linear polariser just in front of the camera. Unfortunately, time constraints and limitations imposed by the difficulty of removing the modulators made this task unfeasible to do in the standard method. The second linear polariser was therefore not included, nor were the modulator prisms removed. As such, a substitute method was devised to allow for the obtaining of results despite this.

Unlike the main linear polariser which was used for all of the previous measurements, the waveplate mount has a different design with markings showing the approximate locations for each angle of the waveplate axis. This means that it is not required to characterise the waveplate entirely from the very start. Knowing this, and knowing that when the waveplate axis and the linear polariser axis align the waveplate will have no effect, it is possible to verify the measurements taken for circular incident polarisation.

In total, the following measurements had to be taken: First of all, measurements had to be taken around the mount '0°' position. These were done using the same camera settings as usual. The linear polariser was changed per measurement for each angle ranging from 169.66° to 179.56° in steps of 0.1°. By observing the change in the fluctuations detected by the camera, it is possible to determine the minimal effect of the QWP and therefore its alignment. The same was done for the 90 degree QWP mount position using linear polariser angles between 259.56° and 269.56°. This set of measurements is meant to allow for the offset observed in the previous measurements to be verified.

Finally, the desired circular polarisation measurements could be performed. For these, the linear polariser was set to its 45 degree equivalent state at 219.56° on its mount. The QWP was set at 0° again and measurements were taken for the linear polariser angle range from 214.56° to 224.56°. In this way the offset could to some extent be compensated based on the prior measurements performed and a sufficiently accurate analysis for the incident circular polarisation was possible.

The last step before the experiments were completed was the measurement of the source itself. To do this, the camera was moved right after the linear polariser. As moving the modulator prisms was not possible at that instance in time, this method had to be used instead, though it causes issues with image pixel alignment compared to the previous measurements. Nonetheless, averaging the images from these measurements should give a baseline pixel intensity with which to compare the outputs.

## 7.3. Results

In this section the main images taken during the experiment are shown, along with the primary analysis of the images to obtain the results. Due to the modulator prisms being placed sideways as mentioned in subsec-

tion 7.2.1, note that in results analysis, the 0° linear polariser orientation for the incident light actually corresponds to a vertical polarisation state based on the modulator coordinate system.

### 7.3.1. Compiled Images

In this subsection, some examples of the compiled images will be shown. While showing all images would be excessive, the ones corresponding the closest to the 0°, 45°, 90° and -45° cases, with respect to the modulator axes, are shown here in Figure 7.4 to Figure 7.7.

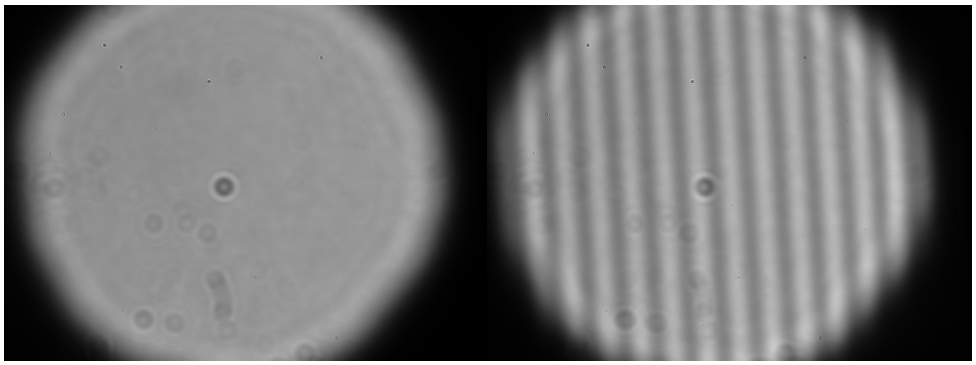

**Figure 7.4:** 0° incident polarisation image.



**Figure 7.5:** 45° incident polarisation image.

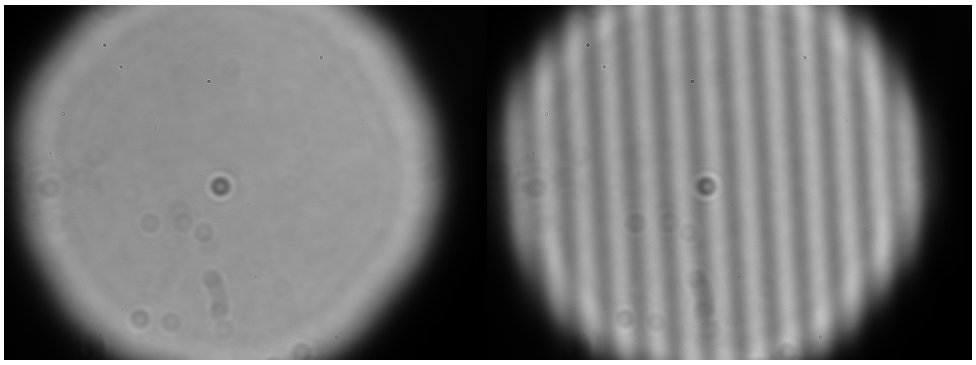

**Figure 7.6:** 90° incident polarisation image.



**Figure 7.7:** -45° incident polarisation image.

**Circular Polarisation**

Circular polarisation measurements were also performed but due to complications regarding the quarter waveplate orientation and insufficient time to properly analyse the images appropriately, these will be neglected for this particular study. To show the behaviour of circular polarisation at least to a degree, Figure 7.8 shows one of the measurements at what is assumed to be close to the ideal right hand circular polarisation.

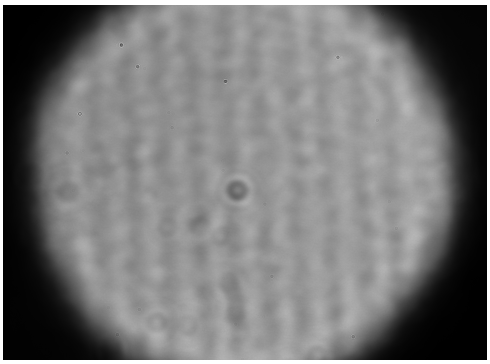

**Figure 7.8:** Incident right hand circular polarisation image.

Due to time constraints, and concerns with having to recalibrate the modulator positioning within the clamp, it was not possible to perform a conventional characterisation of the quarter waveplate. A different method

was applied which would have formed the foundation required to still obtain the measurements which were desired. As the results are not utilised and therefore do not provide additional value to the data analysis and comparisons in future sections, the details on the method through which the calibration would have been performed during the analysis of the images, are provided in Appendix D.

### 7.3.2. Analysis of Images

When it comes to analysis of the images, it is not sufficient to simply take the camera outputs as they have been produced. When looking at the resulting pictures for each incident polarisation state, it is not only the fluctuations which can be seen. In addition to the pattern which was being sought in the experiment, there are also other phenomena presented. These are dust particles that are deposited on the components and the camera. As the lab is not based in a clean room, there is little which can be done to remove this properly, and the time in which the lab was available did not allow for a proper cleaning of the setup, nor the recalibration of each component which would have to take place after cleaning was performed. This means that a different method must be applied to negate their effect as much as possible. One such method is to select a region of the image to use rather than the entire picture. Fortunately, the dust particles are in the same places in all measurements across all of the different incident polarisation states, therefore the same region can be used everywhere.

Two regions of the images were identified as the 'cleanest' regions with reduced effect of the particles. These are depicted in Figure 7.9. The red region spans a vertical range from pixel 670 to 1300 and a horizontal from 650 to 3050, while the orange region ranges a vertical from 1000 to 2200 and horizontal from 2100 to 3000. While the previous plots were the raw images as obtained from the camera, the images below are now shown after some initial Python processing. With Python it was possible to apply an RGB colouring based on the number of intensity 'counts' which each camera pixel has. Rather than maintain the greyscale of the camera, this colouring provides a more clear contrast and scale to the figures and will be used from now on.

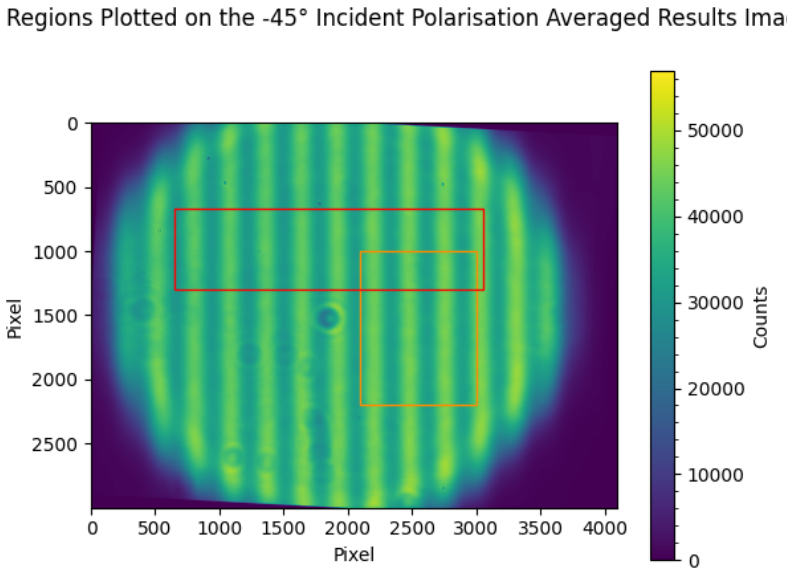


**Figure 7.9:** Regions with limited dust particle effects marked in red and orange.

In the end the red region was chosen as the primary region for further study, primarily due to the inclusion of more fluctuation cycles which can therefore give more usable data to analyse.

Simply selecting the region to look at is not sufficient to immediately begin plotting the fluctuations. The image, prior to being cropped to just the region of interest first has to have the 'dark' image subtracted from it. This is performed by taking the images corresponding to the 'dark' of the measurements, averaging out the 'dark' images, and removing the values of each pixel from the actual measurements for each corresponding pixel. After this is performed, the image is also rotated to make the lines caused by the intensity variation to be as close to vertical as possible. this is to make the analysis of the period and amplitudes easier when averaging pixels along each column of the figure. The precise misalignment is unknown and therefore this step is performed manually through observation. The process involved rotating the image degree by degree and determining at

which step it was most vertical visually. In Figure 7.9, the results have already been rotated by -3° which was the final rotation at which the image was left.

This process is repeated for all of the 5 images in the measurement corresponding to the chosen incident polarisation state. The results of all 5 images are then averaged together as well and a final 'cumulative' image is produced representing the averaged image. This is followed by the cumulative image being cropped to only the region of interest.

Finally, to obtain plots which can be analysed and compared to the Jones model or the ZEMAX simulations, the pixel values along each column are averaged and then divided by the average pixel value of the source measurements. This step was intended to allow for a transmission comparison between the source light and the output in order to obtain the percentage transmission. An example of the source measurement is shown in Figure 7.10.

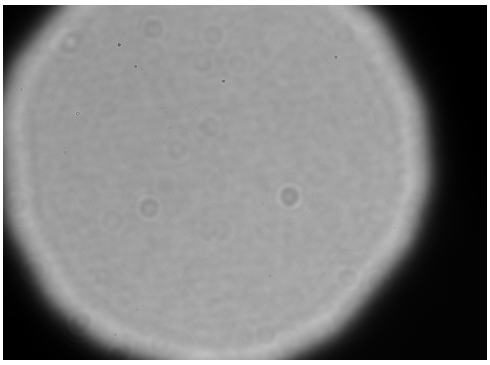

**Figure 7.10:** Example image of the source.

Unfortunately, the average source pixel value did not necessarily correspond to the same instance in time nor the same exact running conditions of the source and camera as the measurements ended up being taken only at the end of all of the other measurements. Furthermore, the components had to be moved to take the source measurement properly which also affected the pixel alignment and values of the source image. The reason this is important is because, without any further modification, the results can show intensities higher than the source intensity, which should not be possible. The results which needed to be altered are shown in Figure 7.11 and Figure 7.12.

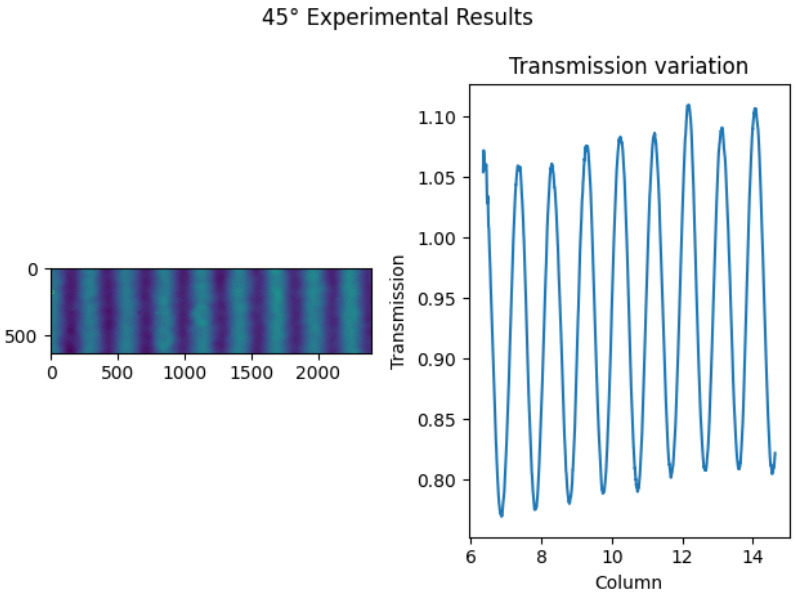


**Figure 7.11:** Experimental results for 45° incident polarisation without normalisation.

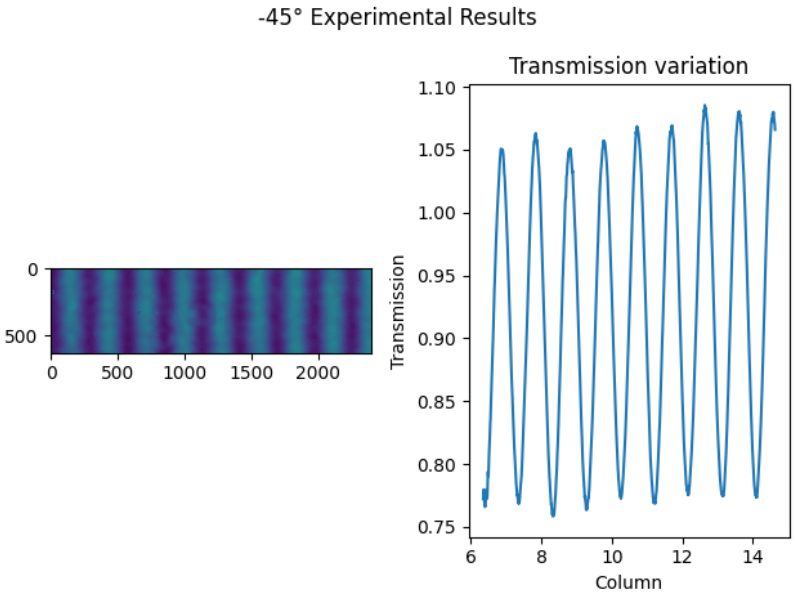


**Figure 7.12:** Experimental results for -45° incident polarisation without normalisation.

A simple solution, albeit only an approximative fix, is to normalise the data and make the peak equal to 1. This obviously does not give the 'true' values of the fluctuation per se; however, it does give a plot which can be used to compare at least qualitatively, and draw some general conclusions. This was only required for the 45° and -45° cases, whereas the 0° and 90° cases were already below the source output. It also only affects the amplitudes, while the period is not affected.

Determining which specific angle of the linear polariser corresponded to the desired incident polarisation state was performed using these plots by comparing the amplitudes of the fluctuations and selecting the measurement with the smallest fluctuations for 0° and 90°, and the largest for the 45° and -45° cases.

This process of obtaining the transmission plots resulted in the final graphs from Figure 7.13 to Figure 7.16 where the final processed region and final intensity plot are shown.

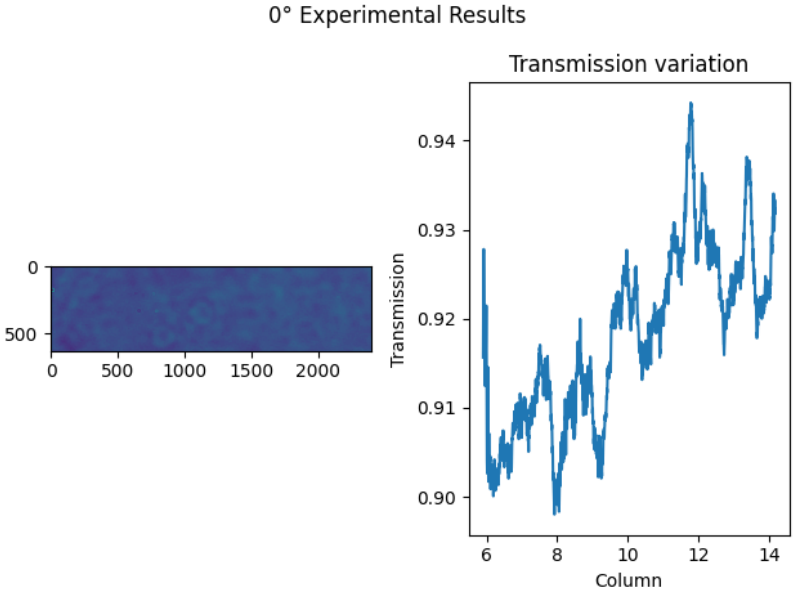


**Figure 7.13:** Experimental results for 0° incident polarisation.

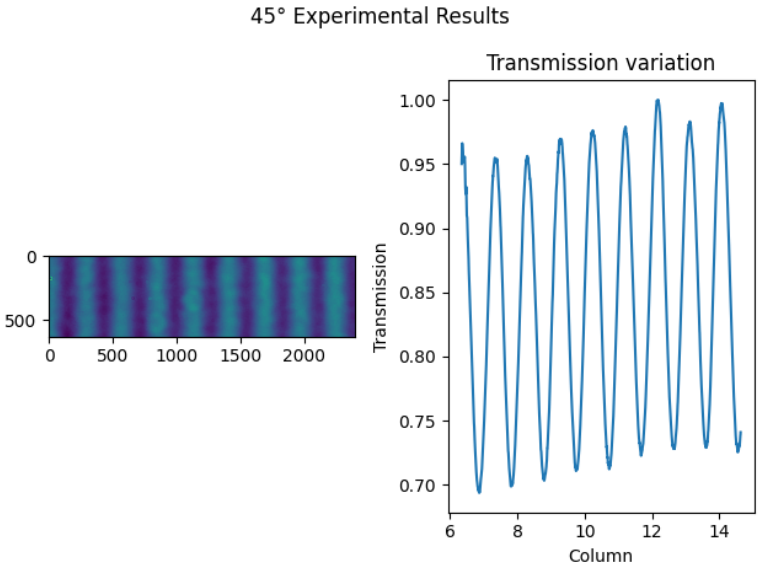


**Figure 7.14:** Experimental results for 45° incident polarisation.

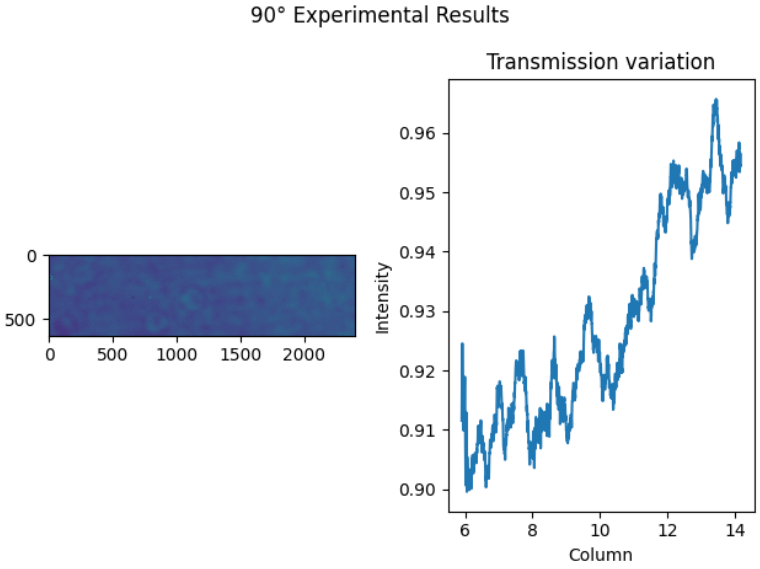


**Figure 7.15:** Experimental results for 90° incident polarisation.

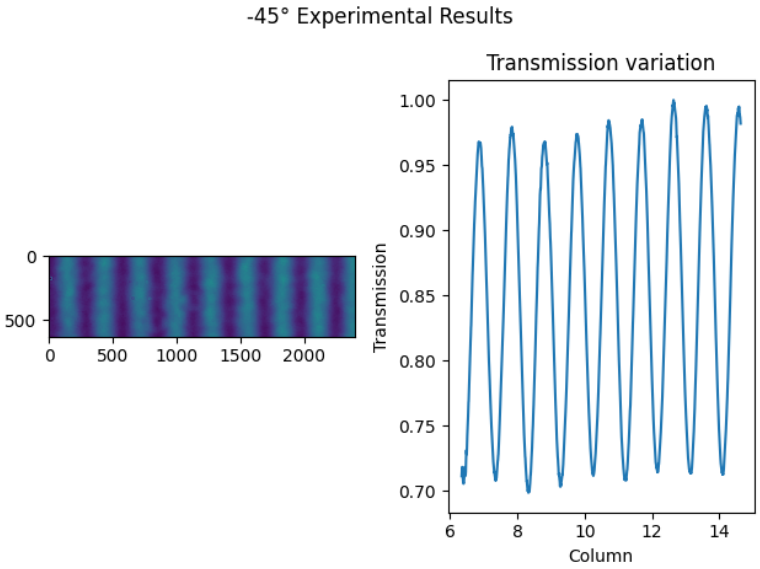


**Figure 7.16:** Experimental results for -45° incident polarisation.

For a better visual look at the cropped images themselves, the averaged figures, which are the final measurement after the 5 images taken per measurement are averaged out, are also shown in Figure 7.17. All of the images are on the same contrast scale to allow for visual comparison to be made between the results.

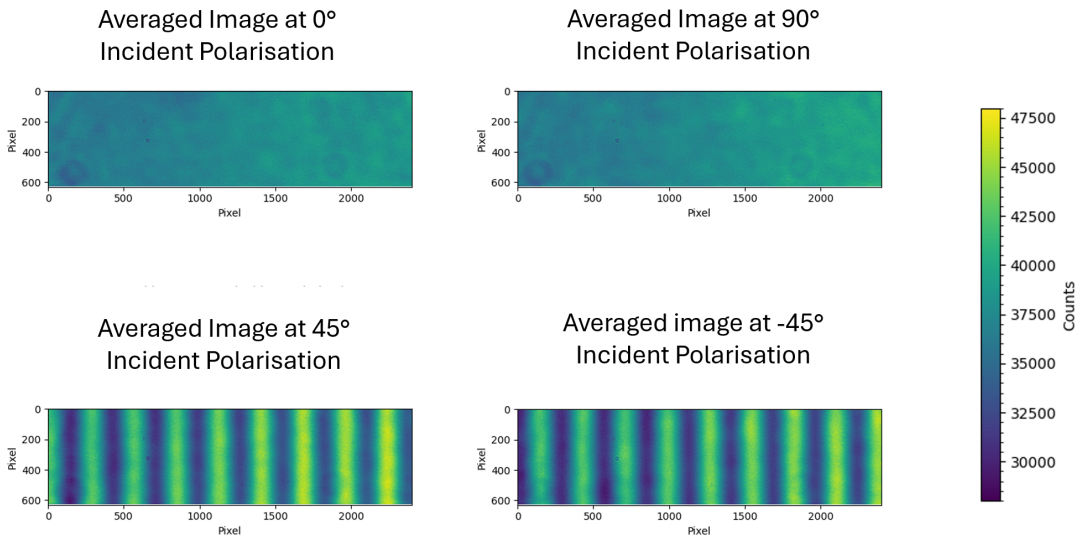


**Figure 7.17:** Averaged images at 0°, 90° and ±45 incident polarisation.

From the results of the experiment and how they were plotted, the 0° and 90° cases stand out significantly compared to any fluctuations seen so far in the report. The expectation was that there would be no fluctuations visible in the plotting of these cases. From the images themselves, no inherent fluctuations which could be linked to Fresnel phenomena can be seen with the naked eye, which supports the current knowledge that there should not be any. Additionally, no patterns indicative of ghosting are present either. There are, however, fluctuations in the colours of the pixels in each column in the image, and a noticeable gradient from left to right both contribute to the final pattern. As the gradient is visible in the images with no additional analysis being performed, it explains the large degree of variation in the transmission intensity as the column number increases.

The general trend of intensity fluctuation in these results seems larger than it should be due to the relatively low pixel count per column. This means that there are not sufficient pixels to average out which can reduce the effect of outliers or inconsistencies in how the light is being detected by the camera. Using the orange region of Figure 7.9 may have reduced how prominent this effect is. Alternatively, further adjustment of the camera settings may have been able to reduce the larger deviations in pixel values along the same column.

For the 45° and -45° plots, on the other hand, the fluctuations greatly resemble what has been seen before. At a first glance the fluctuations appear far larger than expected, but this is supported by the fact that they are also visible on the camera to the naked eye as well. The extent to which the transmission intensity of the light is representative of the true transmission is unclear because of the issues with measuring the source which were mentioned before, but it can be concluded that the experiment has larger amplitudes than the Jones or ZEMAX methods predicted. The precise comparisons between the methods and their outcomes are discussed in chapter 8.

## 7.4. Limitations

A remaining aspect of the experimental work which is critical to discuss is the limitations of the experiments and data analysis. These are listed below:

The first, and most impactful, limitation was the method of alignment of the prisms. Specialised equipment was not available at the time of the experiment, and because of how small and fragile the prisms are, it was only possible to judge their position and alignment by eye and by observing the light reflections occurring in each respective prism (using a white sheet to observe where each face of the prism was redirecting the light). Specifically, the method used for the alignment of the prisms was to use the reflections off each face of the prism. For Prism 1, the reflection off the first face was used to ensure normal incidence. The source was shone against the

prism, and a white sheet of paper was used to observe where the reflected light was being directed. The same process was performed for each subsequent boundary to make sure the angle of incidence to each boundary is as close to the expected angle as possible. Nonetheless, this method, of course, limits the experiment to the level of human error incurred in trying to determine the alignment of the prisms by eye, and by having to clamp them manually. The added element of having apex angles barely visible to the naked eye also results in uncertainty in the position of the edges of the prisms. As the purpose of the thesis is to do a preliminary research into the Fresnel behaviour, and due to both models and simulations using approximations and having their own subsequent errors, it was deemed sufficient to perform the modulator prism placement in this way for the sake of a first comparison.

Another limitation of the current experiments is the fact that no additional dark measurements were taken at each new measurement point. As the conditions were deemed sufficiently unchanged that the extent to which the results would be affected is negligible within the margins of error already created from models, simulations and setup design, it was neglected in favour of achieving all measurements with the time constraints imposed by equipment availability.

When it comes to the source measurement performed at the end, some more limitations must be discussed. The measurement was taken only at the very end. This is because moving the camera between measurements would cause errors due to misalignment and unintentional movement of other components along with taking far longer to complete measurements. Taking the source measurement this way of course means they do not correspond to each measurement done for the modulator specifically. The source may have changed to some extent as all the other measurements were taken and both camera and source heated up.

Ideally this means that new measurements should have been taken for the source at each new measurement for the incident polarisation state, however, this source of error was deemed negligible. Given both the sources of error which are already known to be present from modulator placement, simulation and model approximations, and the difficulty of recreating the exact same position for the camera each time without affecting the fragile modulator prisms, the overall change in performance of source and camera is being considered as less detrimental than changing the entire layout of the setup repeatedly.

# 8

# Comparisons between Methods and Results

In this chapter, the final comparisons between the different methods by which the Fresnel behaviour was measured or modelled are discussed. In section 8.1, the plots of all of the different fluctuations which can be compared to one another are showcased. The analysis of the results is also provided. After this, in section 8.2, the results are discussed in terms of their significance, and relation to the original goals of the thesis..

## 8.1. Final Comparisons

In this section, the Jones Python mode, the ZEMAX simulations and the experimental results are all brought together in order to explore the methods and the extent to which these are able to answer the research question. As the Python models and the ZEMAX simulations were created prior to the experiment being performed, the original plots do not match the exact specifications of the experiment. The experiment used light at a wavelength of $515nm$ whereas all previous results discussed in chapter 5 and chapter 6 all used $587.6nm$ as the arbitrary wavelength taken for the original checking of the Fresnel phenomenon. To solve this, modifications were made to both Python and ZEMAX which align the wavelength of the models and simulations to the wavelength enforced by the spectral filter used in the lab. Another small adjustment which was required in order to fully compare all of the methods was to transform the columns of the image into corresponding heights as the image was taken with the modulator on its side. To do this, the pixel size was obtained from the specifications of the camera as being 3.45 microns. This was transformed into mm and then the column number was multiplied by this value to get the corresponding height.

### **8.1.1.** Final Results

Once the model plots were recreated, and the simulations were re-run with the new wavelength selected, the results for each incident polarisation state for which results could be obtained for all 3 were plotted together to allow for an assessment to be made of how the predictions of the intensity fluctuations compare to the experimentally observed fluctuations. To start with, the 0° and 90° plots, seen already in section 7.3, are known to be different to the expected behaviour. Despite this, the results were still plotted for the sake of understanding how they compare and how significant the effect of the image quality is on the output. The results are given from Figure 8.1 to Figure 8.4 with both a wider view showing the entire set of experimental data and a narrower view which focusses on the ZEMAX simulations smaller detector surface.

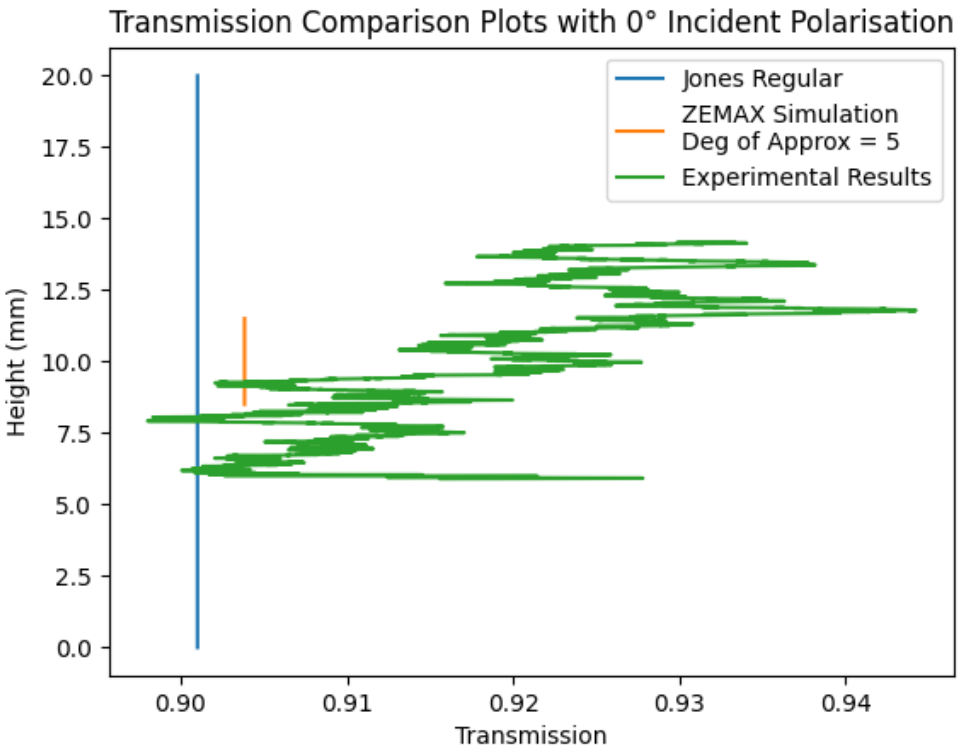


**Figure 8.1:** Wide view of the comparison plot of all the methods results for a 0° incident polarisation case.

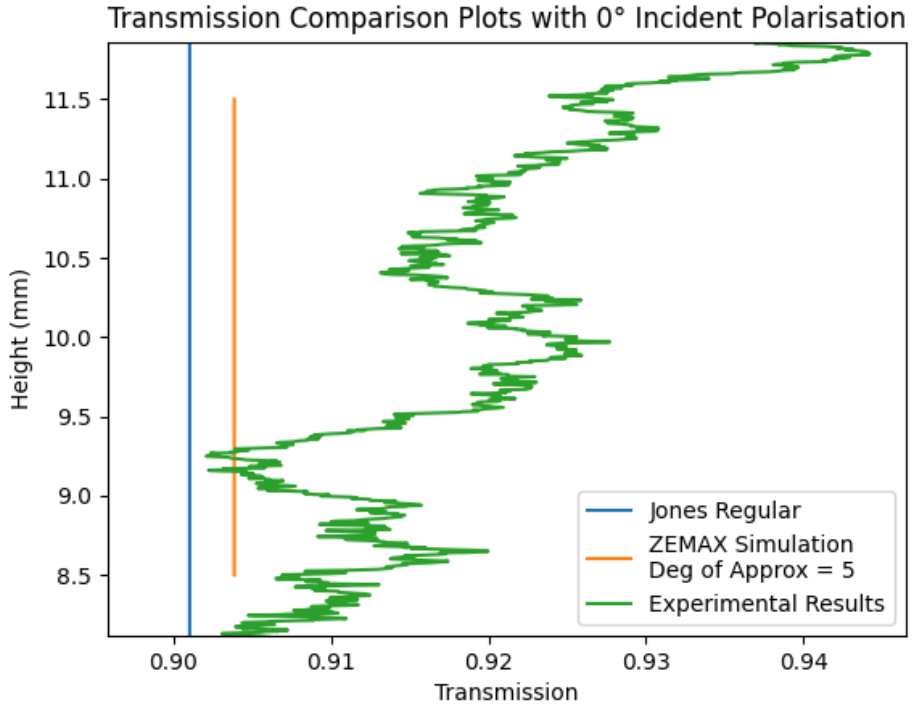


**Figure 8.2:** Narrower view of the comparison plot of all the methods results for a 0° incident polarisation case, focussed on ZEMAX results.

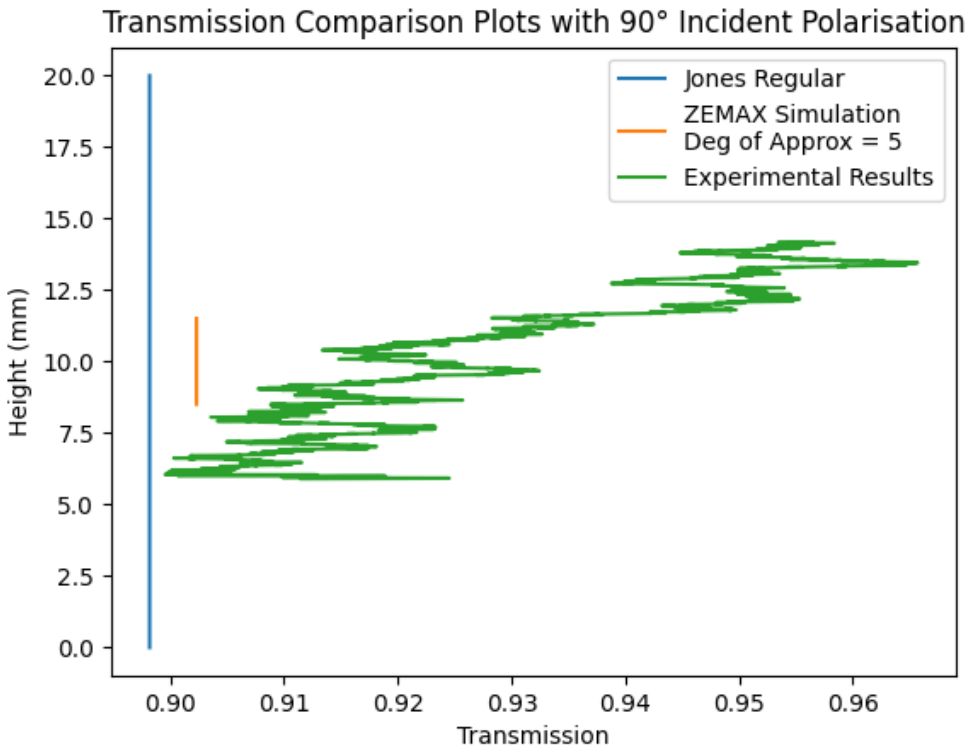


**Figure 8.3:** Wide view of the comparison plot of all the methods results for a 90° incident polarisation case.


**Figure 8.4:** Narrower view of the comparison plot of all the methods results for a 90° incident polarisation case, focussed on ZEMAX results.

From these comparisons, there are a few main points to make note of. The first is that after ghosting is removed, ZEMAX shows an overall transmission which is close to the Jones model at 0.9038 compared to Jones at 0.901 in the case of 0° transmission, and 0.9023 compared to 0.8982 in the case of 90° incident polarisation. The difference can be potentially explained by the Jones Fresnel coefficient calculation method, or due to the

secondary reflections which are not considered at all in the Jones model. For the experimental results, a higher degree of data analysis would have to be applied to compensate for the lighting inequalities on the camera, and the increase in intensity specifically on the upper end of the modulator. Ideally, more measurements should be performed as well with the lab setup adjusted and closely monitored to remove such effects, or compensate for them. This is, however, beyond the time frame of this thesis.

When it comes to the 45° and -45° results, the experiment was able to produce results which do follow expectations based on previous experiments from section 3.2 and from the models and simulations. In Figure 8.5 to Figure 8.8 the comparisons are shown, once again with a wider view as well as a narrower view focusing on the peaks of the 3 plots.

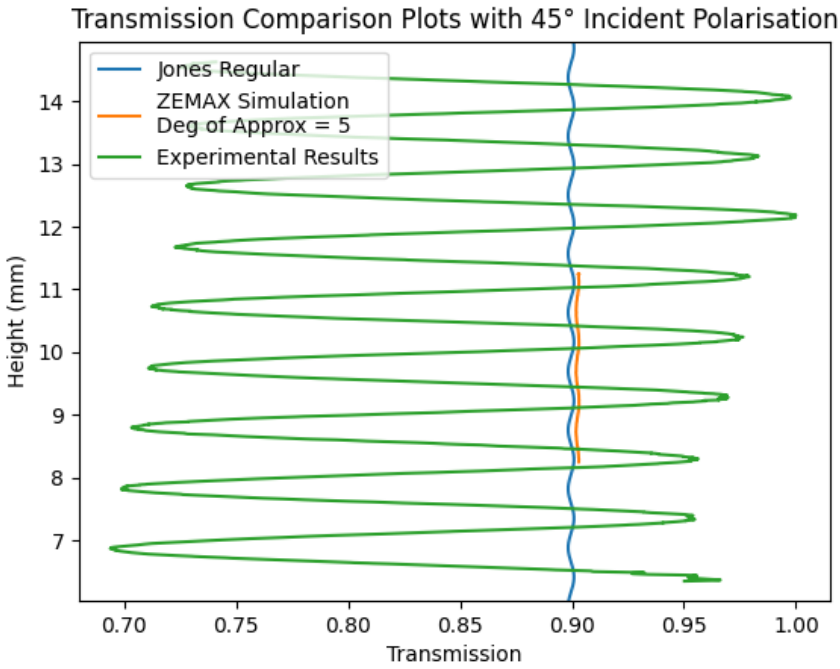


**Figure 8.5:** Wide view of the comparison plot of all the methods results for a 45° incident polarisation case.

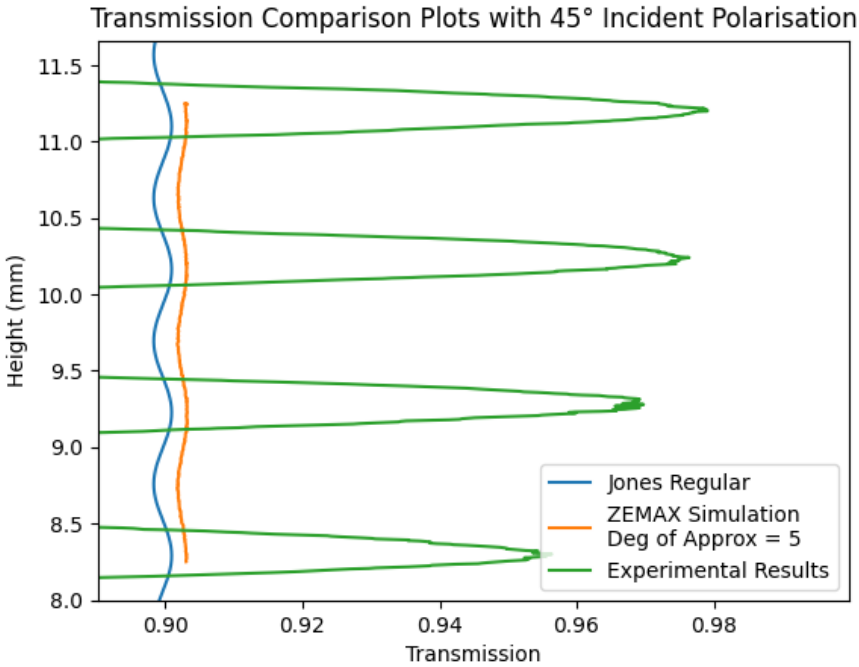


**Figure 8.6:** Narrower view of the comparison plot of all the methods results for a 45° incident polarisation case, focussed on the peak alignment.

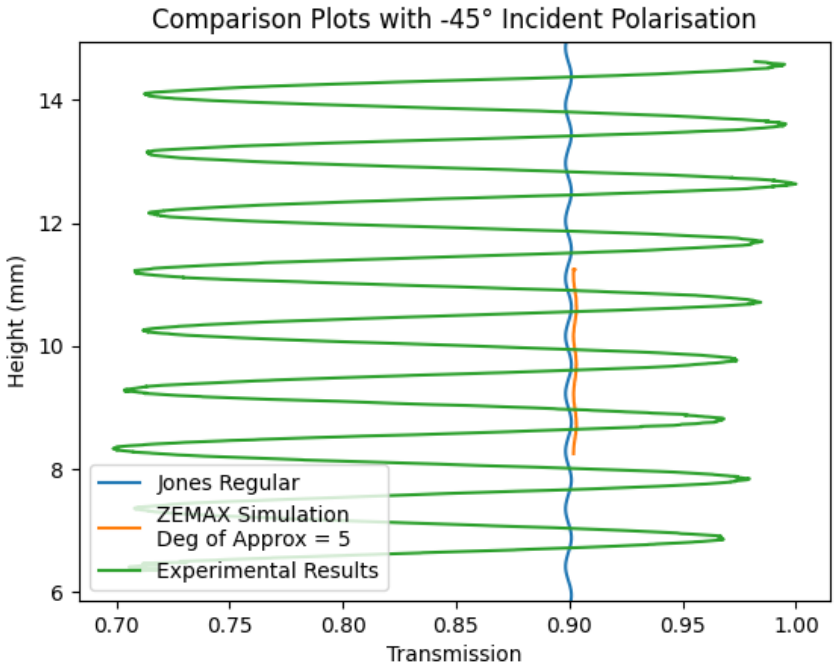


**Figure 8.7:** Wide view of the comparison plot of all the methods results for a -45° incident polarisation case.

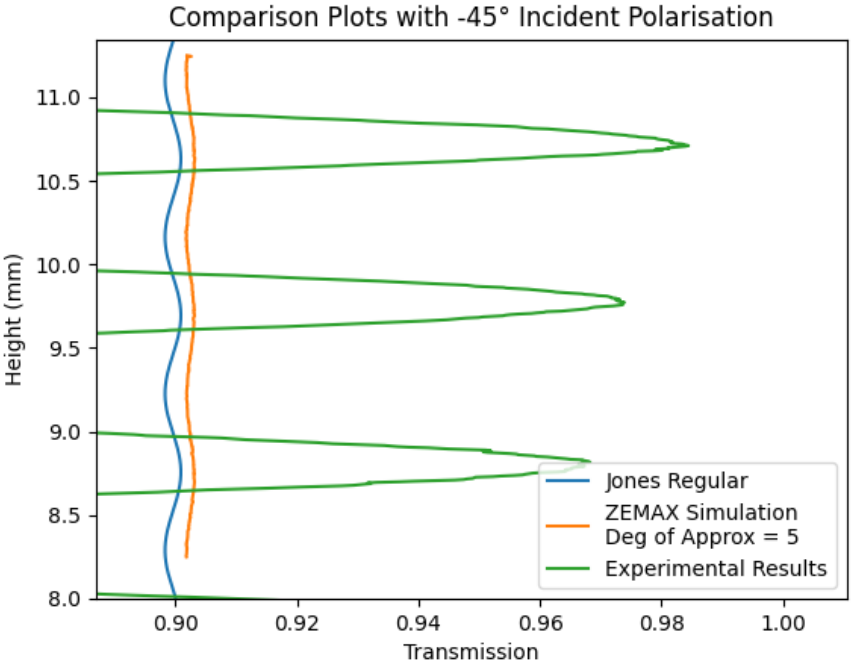


**Figure 8.8:** Narrower view of the comparison plot of all the methods results for a 45° incident polarisation case, focussed on the peak alignment.

It is also important to note that the results have been adjusted to align the peaks and valleys manually and conclusions cannot be drawn on the precise position of each peak or valley in terms of the modulator height. This is because, unlike ZEMAX, the Jones model does not take into account that the exit rays to not exit at the exact same height level as they initially entered at. ZEMAX changes the precise position of the fluctuations depending on material properties and material property induced refractions which change based on wavelength,

while the Python model does not. The experimental results are also manually aligned as the precise section of the modulator from which the fluctuations originate in the images is not precisely known. It was deemed acceptable to make this adjustment as the comparisons can only be made in terms of the shapes of the fluctuations and not their precise position anyway as the positions would have to be estimated regardless. The adjustments were also made in such a way that the pattern still remained as close to where ZEMAX originally placed them, resulting in a downwards adjustment of only 0.3mm.

The resulting plots of all of the different fluctuation graphs at 45° and -45° all agree on the existence of fluctuations in the intensity output. The existence of these fluctuations in all 3 performed methods confirms that the fluctuations were not an error of the lab setup, nor an issue with the design of the prisms function. In addition to this, the fact that the Jones model shows these fluctuations only once Fresnel phenomena are modelled supports the original hypothesis that these phenomena are the primary source of the variation in intensity. An additional element which supports the hypothesis that the intensity fluctuations can be explained by Fresnel phenomena, is the extremely similar period in all 3 methods.

As for the actual value of the periods, as an example, in the 45° case, Jones returns a period of 0.94mm, ZEMAX returns a period of approximately 0.953mm and finally, the experimental results show an average period of 0.967mm.

The amplitudes of the ZEMAX graphs compared to Jones also are similar. ZEMAX returns smaller overall intensity variation than the Jones Python model does, but this could be attributed to the Jones model using only the maximum and minimum refractive indices of the prisms without any consideration for the refraction of the ray resulting in the material properties changing slightly.

Now in terms of the differences, the most obvious one is that the amplitudes of the experimental results are far greater than anything which has been predicted by Jones models and ZEMAX simulations. Of course, this comparison can only be performed approximatively because of the method through which the relative transmission is calculated using the images of the source, but nonetheless, the fluctuations are several degrees greater in scale than expected. In addition to this, the average intensity is also different. Finally, the period, although close, is not an exact match when it comes to the experimental data.

### 8.1.2. Summary of the Results

For more clarity, the specific values for the 45° and -45° incident polarisation cases can be summarised to provide a more clear quantitative comparison. These values are given in Table 8.1 and Table 8.2.

**Table 8.1:** Main values for the 45° incident polarisation case.

| 45° Incident Polarisation | Jones Model | ZEMAX Simulation | Experimental Results |
|---|---|---|---|
| Peak to Peak | 0.00261 | 0.00130 | 0.26164 |
| Average Transmission | 0.8996 | 0.9025 | 0.8445 |
| Period (mm) | 0.94 | 0.953 | 0.967 |

**Table 8.2:** Main values for the -45° incident polarisation case.

| -45° Incident Polarisation | Jones Model | ZEMAX Simulation | Experimental Results |
|---|---|---|---|
| Peak to Peak | 0.00260 | 0.00130 | 0.27684 |
| Average Transmission | 0.8996 | 0.9025 | 0.8460 |
| Period (mm) | 0.94 | 0.958 | 0.964 |

While the values themselves generally appear similar, especially in the case of the periods, the cause of the differences must still be explained conclusively. This will now follow in subsection 8.1.3.

### 8.1.3. Analysis of the Results

To attempt to explain why the models, simulations and experiments all provide different results, an investigation was conducted into the main differences in the shape of the fluctuations occur and how these could be replicated.

The simplest difference to suggest an explanation for, is the difference in average intensity between the graphs. For Jones compared to ZEMAX, the most likely causes are the lack of consideration for internal reflections

which still do end up hitting the detector at the end of the modulator. The second order reflections which hit the detector are each approximatively 0.0005% of the light. For each incident ray in the Jones model, there are also 6 possible paths which include two reflections and still reach the detector. Summing all 6 of these paths results in an additional 0.003% which should be added to the average transmission. Based on the plots of the results, the average transmission of ZEMAX results is 0.9025% while the Jones model predicts 0.8996%. The difference is approximately 0.0029% which suggests that these internally reflected ray paths would account for the slight deviation.

For the experimental setup, light was likely lost as the components along the rays paths are not 'ideal' in their function and can have absorptive or reflective behaviour to some degree. Despite the high quality of the components used, the presence of dust particles already suggests that the components do not perform at ideal theoretical levels and this may account for the slight decrease in overall average intensity transmitted. Since the method of calculating the experimental fluctuations also depends on the source measurements which were unreliable, it is also possible that the current position is not the true average transmission either.

For the amplitude difference and the period difference, the theory which was investigated was whether the prisms themselves had some minor inconsistencies in the refractive indices as compared to the design specifications. As such, the Jones model was adapted to test two different situations. The first was keeping the difference between refractive indices the same, and changing the average refractive index value. The second, was to maintain the same average refractive index but increase or decrease the difference between the refractive indices.

With the first method, the refractive indices were increased and decreased by 1% and 2% of the average refractive index to observe the effect which this had on the results. Based on Figure 8.9, it was seen that by just shifting the refractive indices but maintaining the difference between the fast and slow-axis refractive indices, the only change was in the average transmission.

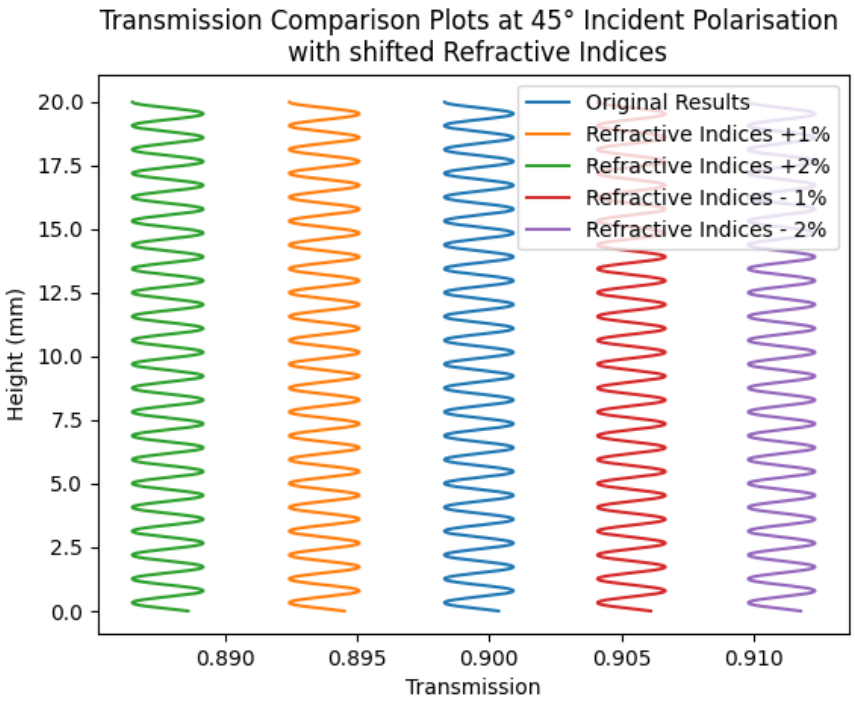


**Figure 8.9:** Results of shifting the refractive indices up or down by 1% or 2% of the average refractive index value.

Based on the fact that the refractive indices directly correlate to how much light is transmitted, increasing or decreasing the value of the refractive indices is expected to cause this kind of behaviour. The amplitudes and period, on the other hand, are unaffected by this change in material properties. Therefore, this is not sufficient to explain the main differences between the model and the experimental results which still require the most investigation.

The second method, which involves changing the difference between the fast and slow-axis refractive indices

rather than shifting the average, was similarly performed by increasing and decreasing the difference. It was noted that a change in the difference between the refractive indices caused an effect on both period and peak to peak values. In Figure 8.10 and Figure 8.11, it is possible to see 2 extreme examples of the changes which occur.

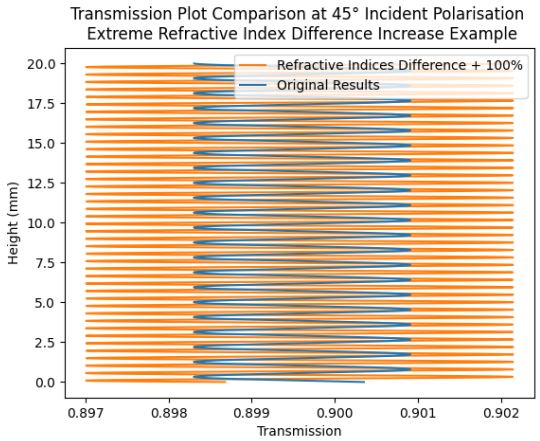


**Figure 8.10:** Original Jones model results compared to a version with the difference between the fast-axis and slow-axis refractive indices increased by 100%.

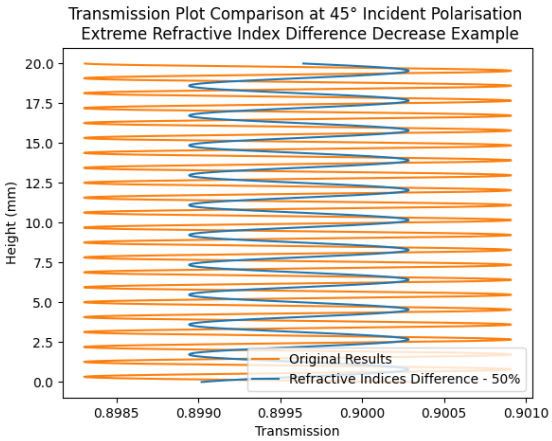


**Figure 8.11:** Original Jones model results compared to a version with the difference between the fast-axis and slow-axis refractive indices decreased by 50%.

The effect on the peak to peak value directly correlates to the maximum and minimum refractive intensities which the light experiences. The period depends on the phaseshift which is induced. As the difference in refractive indices directly affects both of these factors, the changes are expected. As a less extreme example, the comparison for a case where the difference is increased by 10% is shown in Figure 8.12 and Figure 8.13 where the original results can be seen beside the altered version.

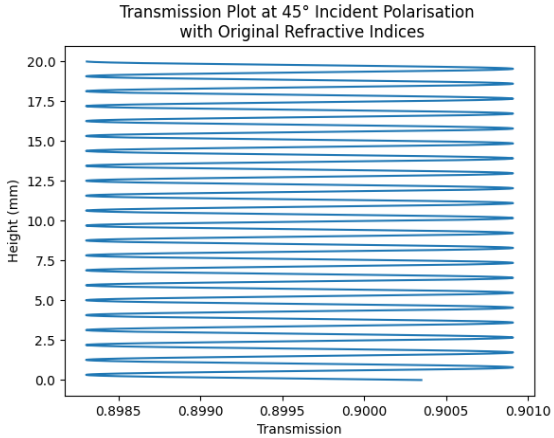


**Figure 8.12:** Original Jones model results with no change to the fast-axis and slow-axis refractive indices.

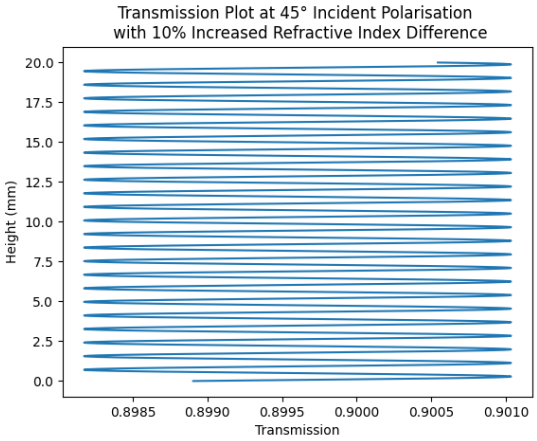


**Figure 8.13:** Jones model results with a 10% increase in the difference between the fast-axis and slow-axis refractive indices.

Between these two sets of results, the period changes from the original 0.94mm period to a period of 0.85mm instead. With a 10% decrease in the difference, on the other hand, the period becomes 1.04mm instead. It is possible to recreate the period of the experimental results with only a 3% decrease in the difference between the refractive indices, resulting in a period of 0.97mm.

From the testing performed based on changing the material properties in this way, it was determined that the changes shown in Table 8.3 take place for increases and decreases of 1%, 3% and 5%.

| | Change in the Difference between Refractive Indices | | | | | | |
|---|---|---|---|---|---|---|---|
| 45\degree\Incident Polarisation | -5% | -3% | -1% | Original Data | +1% | +3% | +5% |
| Peak to Peak | 0.00248 | 0.00253 | 0.00258 | 0.00261 | 0.00263 | 0.00268 | 0.00273 |
| Period (mm) | 0.99 | 0.97 | 0.95 | 0.94 | 0.93 | 0.91 | 0.89 |

**Table 8.3:** Table showing the difference in the peak to peak values and period as the refractive index difference is increased or decreased by 1%, 3% and 5%.

The change appears consistent with each additional 2% change to the difference in refractive indices causing a shift of approximately 0.02mm in the period, and around 0.00005 in the peak to peak value.

To summarise these findings in broad terms, it was determined that

- Method 1: The period stays the same, the average transmission increases with lower average and decreases with higher average.
- Method 2: Increasing the difference increases the period and increases the peak to peak values, decreasing the difference reduces the period and decreases the peak to peak values.

More research would be needed to demonstrate that this pattern remains consistent with greater changes to the refractive indices for method 2, and to determine what happens if a combination of both methods is applied at once.

While neither method explained the amplitude difference which was observed in the results, the slight change in period between the model and the experiment could be caused by a slight difference in the actual material properties.

For the difference in amplitudes between the Jones mode and experimental results, another model adaptation was introduced in which the angles of incidence were shifted away from the ideal case. Due to time constraints it was not possible to attempt this method for every boundary, but after some testing it was observed that, if the angle of incidence into the first prism was increased to 10° instead of normal incidence, the amplitudes would begin to show a noticeable increase. During the experiment the first prism was placed as close to normal incidence as possible, therefore 10° or higher deviations are extremely unlikely. Prism 3's exact orientation, and the correct position of the prisms, could not be verified however. This means that it is possible for the angle of incidence on boundaries 2, 3 and 4 to not match with ideal situation. As the prisms have such small apex angles, it was not possible to see exactly which side corresponded to the 'front' and which corresponded to the 'back', so a modulator prism setup as shown in Figure 8.14 is possible to have occurred, as well as other variations in which directions the prisms face.

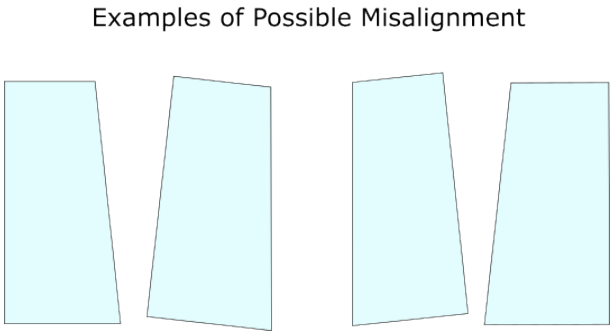


**Figure 8.14:** Some examples of possible prism misalignments where one prism is rotated the wrong way. Due to the scale of the prisms, the reflections of the faces would behave as expected when aligning, but the material properties will be different.

Additional investigation into the exact recreation of the amplitudes from the experimental results was not achievable within the timeframe of the thesis, but it is theorised that the amplitude measurements are sensitive to the precise positioning of the prisms, while the period is sensitive to the precise difference between fast and slow-axis refractive indices. There may also be additional phenomena working to enhance the effect of the Fresnel behaviour and therefore the variation amplitudes.

A misalignment of the prisms can technically explain the difference in both amplitude and period as the material properties change from the misalignment too. Hence, the period would be altered alongside the peak to peak values of the results in the case of the prisms shifting from their ideal positions.

## 8.2. Discussion of the Results

With the final comparisons of this thesis having been made, it is possible to review the findings in the context of the research goals and sub-goals. From the plots in subsection 8.1.1, it was shown that the fluctuations observed in experiments performed before this thesis study can be linked directly to Fresnel phenomena.

As to the extent to which the intensity fluctuations can be explained by Fresnel behaviour, the models and simulations have shown that Fresnel effects must be considered for the results to show variations in intensity. The Jones models did not demonstrate any variation in intensity when Fresnel phenomena were not included. Once included, the results were verified with ZEMAX simulation results, which showed that these fluctuations should, in fact, be occurring. Furthermore, the differences between ZEMAX and Jones are easily explainable through the inclusion of internal reflections in the ZEMAX simulations, and the slight changes in material properties caused by the refraction of the light. This solidifies that the fluctuations observed are representative of the same behaviour that the Jones Python code attempted to model.

If the experimental results are now also considered, the periodicity of the fluctuations appears closely linked to Fresnel phenomena at the boundaries, as each of the methods used to create the results has a very similar period. The differences in the period between the 3 models can be attributed to the material property changes shown in Table 8.3. It is therefore possible to connect the period of the fluctuations to the Fresnel behaviour directly. With slight modifications to the Jones model to compensate for the ray refraction, it is also possible to model the fluctuation peaks with respect to the location along the height of the modulator.

The scale of the fluctuations in terms of the amplitude variation, however, cannot be modelled just through the simple addition of Fresnel phenomena to the models. It appears, from the peak to peak scale of the fluctuations in the experimental results, that there is an additional factor determining the size of the peaks and the dips.

Attempts were made to explain the amplitude differences between the different methods. The main theoretical way of explaining this difference was due to the lab experiment not being an 'ideal' representation of the intended setup whereas Python and ZEMAX assume all components are both placed, and function, perfectly with no losses, or additional effects. The actual lab setup is influenced by potential issues in the alignment of components, primarily the modulator, as well as uneven lighting across the images which were obtained. Along with this, the source measurements require further improvement. The amount of light lost as it propagated through the setup was also not investigated thoroughly due to time constraints.

Due to the limitations of the experimental method applied, it is difficult to validate the Jones and ZEMAX results in terms of the peak to peak values. Therefore, additional measurements should be taken with improvements made to the modulator placement technique and the source measurements. It would also be valuable if measurements were taken with coatings applied which mitigate Fresnel reflections. In this way, it may be possible to observe if there are additional effects influencing the scale of the fluctuations.

There are a number of ways in which the results of the study can be used, based on the desired goal. From the Jones method in particular, it was observed that fluctuations do not occur without the Fresnel matrices. Assuming that no additional factors are significantly affecting the results, applying anti-reflective coatings to the prisms has the potential to diminish or even remove these fluctuations entirely. This would improve the performance of the modulator by removing one of the main causes of unexpected behaviour.

Alternatively, if coating the prisms is undesirable or unfeasible, the results have demonstrated that it may be possible to fully describe the Fresnel induced fluctuations with some additional adjustments to the Jones model. With another set of lab experimental results that can confirm the extent of the amplitude difference, it appears likely that the Fresnel fluctuations can be predicted and therefore removed during data analysis. Even if the amplitude cannot be entirely modelled, the fact that the period is known means that the intensity variation caused by Fresnel phenomena can still potentially be extracted given that the locations of the peaks and valleys can be calculated.

This research therefore can directly lead to improvements in the accuracy of the spectropolarimeter by having explained the origin of at least a portion of the unexpected behaviour which was previously observed. By having proven that there is a correlation between the Fresnel phenomena and the variations in intensity, future studies can now be directed towards compensating for, or removing the problem, rather than working towards explaining the origin further. This will help make the spectropolarimeter design achieve its intended goals of performing full-Stokes spectropolarimetry without moving parts and with a compact design suitable for a broad range of space applications.

# 9

# Conclusions and Recommendations

In this report, the methodology and results of the MSc thesis project are provided. The thesis focussed on the investigation of a new full-Stokes snapshot spectropolarimetry method which is under development at TU Delft. Specifically, the primary basis of the thesis project was to analyse the causes of unexpected fluctuations in intensity which were observed to be caused by the modulator of the spectropolarimeter. Fresnel behaviour, prior to this thesis, had not been accounted for in models. As the modulator is comprised of multiple birefringent magnesium fluoride prisms, the behaviour at each of the boundaries when the light enters a new medium, was not taken into consideration. As such, the main goal for this thesis was to determine the extent to which the fluctuations in intensity can be explained by Fresnel transmission and reflection behaviour within the modulator.

To achieve this goal, an extensive investigation plan was created. First, a comprehensive literature study was performed in which the fundamentals required for this thesis were researched. Among these, polarimetry, Jones and Mueller-Stokes mathematical representations of polarisation, Fresnel behaviour, and the specific principles of the spectropolarimetry method under investigation were studied.

The scope of the thesis was also narrowed to a single wavelength of light passing through the first and third prisms of the modulator, which are the main active components, as the second prism was not included during the original experiments in which the fluctuations were seen. Having a single wavelength studied at a time served to focus the study on the fluctuations themselves and to ensure clear results were obtained.

Following the literature study, it was decided to create Python models of the modulator in both Jones and Mueller-Stokes formalisms. These models would be used to demonstrate that the inclusion of Fresnel phenomena can produce fluctuations similar to those observed experimentally. During the creation of these models, a gap in the current state of research was discovered when it came to representing Fresnel behaviour in birefringent media. Because of this gap in knowledge, it was determined that a Jones model would be used to model the specific behaviour of the modulator with the inclusion of the Fresnel phenomena at the boundaries, while a simplified Stokes model was used as a primary verification to ensure the models were consistent. The Jones method was favoured over Stokes in this thesis due to the more intuitive nature of the Jones formalism when applied to birefringent materials. This made it easier to verify the accuracy and performance of the model. Along with the decision to focus on Jones, the incident polarisation states which would be used were limited to 0°, 90°, ± 45° and circular polarisation states.

As an additional method through which to thoroughly verify the Python models and to check that the fluctuations occur even when using an independent alternative calculation method, ZEMAX simulations were created. These ZEMAX simulations used non-sequential ray tracing to simulate the precise behaviour of rays as they pass through the 2 main active prisms. The simulations therefore were designed to include not only the transmission of the ray, but also the internal reflections which take place. In this way, it is possible to compare the simulations to, not only the Jones model, but also to experimental results in which internal reflections are present. This would serve to verify the Jones model and provide a better understanding of the phenomena taking place.

When comparing these two methods, the Jones and ZEMAX models created similar results. For 0° and 90° incident polarisation, Jones returned the smallest transmission at 90.1%, and 89.8% of the incident light respectively. ZEMAX estimated a higher transmission by only 0.3% which can be entirely accounted for by internal

reflections, which ZEMAX uses while the Jones model does not. For the 45% and -45% incident polarisation the Jones Python model predicted a lower average intensity by approximately 0.3% once again. In terms of the fluctuation pattern, the Jones method has a slightly higher peak to peak variation than the ZEMAX simulations. The peak to peak values of the fluctuations in ZEMAX are half the size of those from Jones. This difference is expected to originate from the changing refractive index of the material as the ray refracts in the ZEMAX simulation. The ray path in Jones is considered as staying entirely horizontal which is not the case for ZEMAX where ray-tracing is used instead. For the periodicity of the fluctuations, the values are almost identical with Jones predicting 0.94mm periods and ZEMAX results showing around 0.953mm. Much like in the case of the peak to peak values, the material property changes caused by how the ray path is modelled are the suspected cause of this effect.

In order to validate the Python models and the ZEMAX simulations, experimental measurements were also performed. For the experimental measurements, the same layout was used as for the other methods in which only the first and third prisms were considered in the same layout as they would be for the actual modulator. A spectral filter was used to limit the light to a single wavelength, and a linear polariser was used to create the different incident polarisation states which were used in the Jones model and ZEMAX simulations with the exception of circular polarisation.

When comparing the Jones model results to the experimental lab measurements, the differences were greater than between Jones and ZEMAX. The results for 0° and 90° incident polarisation did not demonstrate any recognisable patterns, though the results were affected by slight inequalities in the lighting across the camera. For 45° and -45° results, the fluctuations were present as expected, but were also far larger in their amplitudes than the Jones or ZEMAX results. The results were also distinctly lower in average transmission. The peak to peak values, being around a 26.2% variation in transmission is around 100 times larger than Jones expected. The periodicity, on the other hand, is of about 0.96mm which is only slightly larger than the Jones result at 0.94mm, and ZEMAX at around 0.95mm.

An additional investigation was performed on the potential causes of these differences. During this investigation, the Jones model was adapted to have slightly different refractive indices to observe how this affects the fluctuations. It was determined that by decreasing the difference between the two refractive indices of the birefringent prisms by 3%, the Jones model returned the same period as the experimental results. This suggests that the material which the prisms are made of may be slightly different than the 'ideal' values. Alternatively, it is also possible that this effect is caused by how the light travels through the prisms. The latter option was further reinforced by the observation that implementing a misalignment of the prisms into the Jones model resulted in a noticeable increase in the amplitudes of the fluctuation. Therefore, it is considered likely that the prisms were not placed in an optimal configuration during the experiment due to the difficulty of working with such sensitive and small prisms without additional structural support.

Nonetheless, each of these 3 methods independently demonstrated the presence of intensity fluctuations after the modulator prisms, without the inclusion of a linear polariser following them. Furthermore, each method showed that no fluctuations were expected using 0° and 90° incident linear polarisation states, while ±45° incident linear polarisation resulted in the largest fluctuations. This was consistent with the original observations which led to the thesis project. The periodicity of the fluctuations induced by Fresnel phenomena is also consistent across the methods, suggesting that the specific pattern observed is linked to Fresnel behaviour at the prism boundaries. The similarity between Jones model and ZEMAX results especially, along with the differences being relatively easy to explain, appears to verify the Jones model itself. Furthermore, the Stokes models, implemented for verification, provided exactly the same results as the Jones model for the test cases used. Despite this, the experimental results are incomparable in scale.

The results of this thesis allow the research into the spectropolarimeter to now move past the stage of explaining the origin of the fluctuations and will be able to move on to removing these fluctuations from the data.

To continue the thesis work and determine whether the Fresnel phenomena are affected by other factors which enhance their effects, or if the experimental method required further improvement, some potential solutions to the Fresnel phenomena are provided, along with some recommendations for future study.

**Recommendations**

The thesis study has shown that the fluctuations can, at least in part, be correlated to Fresnel phenomena at the modulator prism boundaries. This means that, by preventing Fresnel phenomena from occurring, it may be possible to remove the need to account for the fluctuations. This could be done by applying anti-reflective coatings to the boundaries of the prisms. Of course, future studies will have to observe the effects

and consequences of having the coating present, but the current issues will be mitigated significantly.

Another possible solution is to try to model the fluctuations further. This can be done in future studies which aim to quantify the effects of the Fresnel phenomena more precisely. Doing so would allow for the fluctuations caused by Fresnel to be accounted for in the final measurements of the spectropolarimeter. Therefore, recommendations for how this study into Fresnel phenomena can be continued are also given.

In future studies on the Fresnel fluctuations caused by the modulator, the first and most important recommendation is to perform another set of measurements using the same setup, but ensuring that the prisms are aligned carefully. A theodolite could be used to make sure that the alignment of the prisms is not affecting the results. By making these measurements, it will be possible to compare them to the previous measurements and understand the precise effect which the prism positioning and orientation can have on the Fresnel fluctuations.

In the case that this is not possible, an alternative method would be to adapt the Jones model, ZEMAX simulations and experimental measurements again but with prism 2 included as a structural support. The effect prism 2 has on the results has not yet been investigated, however, including prism 2 will make it easier to maintain the relative prism positions. Furthermore, by adding this prism to the Jones model and ZEMAX, it will be possible to compare the models with versions used in this thesis to quantify prism 2's influence on the results as well.

To ensure a full explanation of the discrepancy between the Jones Python model and ZEMAX simulations, and to explore the current hypotheses on the origins of the differences, the Jones model should be adapted to include at least second order internal reflections. This would confirm whether the change in average transmission is entirely due to the internal reflections. To take this a step further, adapting the Python model to also account for the refraction of the ray, and the material property changes caused by the changing of the ray's path, would significantly improve the comparisons between the two methods.

Additionally, to mend the identified knowledge gap, it is recommended to continue the research into how to represent Fresnel phenomena at boundaries with birefringent materials. For this thesis, the Jones and Mueller matrices were adapted from Fresnel transmission and reflection matrices designed for isotropic materials. While the adaptation was relatively intuitive for Jones formalism, due to both birefringent materials and Jones vectors treating the behaviour along two independent axes, there is still a level of uncertainty when it comes to how this method affects the results. Furthermore, the Mueller-Stokes model was not pursued to the same degree as the Jones model due to not being able to determine if adapting the Mueller matrices in a similar fashion would provide accurate results. Further literature study and research into whether it would have been achievable to use the Fresnel Mueller-matrices would be valuable in making the models more compatible with the entire full-Stokes range of polarisation states which the spectropolarimetry method is designed for.

Lastly, it is recommended to investigate the ZEMAX simulation parameters which determine how ray tracing is performed within the prisms. This includes not only the waveplate mode compared to trace mode behaviours, but also how the material itself is simulated. Some degree of difference in the results has been directly linked to changing material properties, and therefore it would be ideal to understand how the models differ in terms of how the material is simulated fundamentally.

# Bibliography


Biron, D., Lupi, G., Montini, G., Labate, D., Bruno, U., Melfi, D., Sist, M., Zauli, F., and de Leonibus, L. (2013). Metop-sg 3mi (multi-viewing multi-channel multi-polarization imaging), a powerful observing mission for future operational applications. In *Proc. EUMETSAT Meteorological Satellite Conference, Vienna, Austria*, pages 16–20.

Campo, J., van Amerongen, A., Rietjens, J., Dogan, E., Dingjan, J., Nalla, R., Caron, J., and Hasekamp, O. P. (2018). SPEXone: a Compact Multi-Angle Spectropolarimeter. In *AGU Fall Meeting Abstracts*.

Chaumette, F. (2021). Face identification. In *Computer Vision: A Reference Guide*, page 305–307. Springer.

Clarke, D. (2009). *Stellar Polarimetry*. Wiley.

Collett, E. (1971). Mueller-Stokes Matrix Formulation of Fresnel's Equations. *American Journal of Physics*, 39(5):517–528.

Collett, E. (2005). Field guide to polarization. Spie Bellingham, WA.

Deibler, L. L. and Smith, M. H. (1999). Infrared polarimetry using attenuated total reflection. In *Polarization: Measurement, Analysis, and Remote Sensing II*, volume 3754, pages 99–107. SPIE.

del Toro Iniesta, J. C. and Collados, M. (2000). Optimum Modulation and Demodulation Matrices for Solar Polarimetry. *Applied optics*, 39:1637–42.

Deuzé, J. L., Bréon, F. M., Deschamps, P. Y., Devaux, C., Herman, M., Podaire, A., and Roujean, J. L. (1993). Analysis of the POLDER (POLarization and directionality of earth's reflectances) airborne instrument observations over land surfaces. *Remote Sensing of Environment*, 45(2):137–154.

Dubovik, O., Li, Z., Mishchenko, M. I., Tanré, D., Karol, Y., Bojkov, B., Cairns, B., Diner, D. J., Espinosa, W. R., Goloub, P., Gu, X., Hasekamp, O., Hong, J., Hou, W., Knobelspiesse, K. D., Landgraf, J., Li, L., Litvinov, P., Liu, Y., Lopatin, A., Marbach, T., Maring, H., Martins, V., Meijer, Y., Milinevsky, G., Mukai, S., Parol, F., Qiao, Y., Remer, L., Rietjens, J., Sano, I., Stammes, P., Stamnes, S., Sun, X., Tabary, P., Travis, L. D., Waquet, F., Xu, F., Yan, C., and Yin, D. (2019). Polarimetric remote sensing of atmospheric aerosols: Instruments, methodologies, results, and perspectives. *Journal of Quantitative Spectroscopy and Radiative Transfer*, 224:474–511.

Garcia, R. (2011). Boundary and interface conditions for polarized radiation transport in a multilayer medium. *International Conference on Mathematics and Computational Methods Applied to Nuclear Science and Engineering*.

Goldstein, D. H. and Collett, E. (2003). *Polarized light*. Optical engineering (Marcel Dekker, Inc.). Marcel Dekker, New York, 2nd ed., rev. and expanded edition. OCLC: 52596371.

Gu, C. and Yeh, P. (1999). Extended Jones matrix method and its application in the analysis of compensators for liquid crystal displays. *Displays*, 20(5):237–257.

Hecht, E. (2017). *Optics, 5th edition*. Pearson Education India.

Hough, J. (2006). Polarimetry: a powerful diagnostic tool in astronomy. *Astronomy & Geophysics*, 47(3):3.31–3.35.

Iglesias, F. A., Feller, A., Nagaraju, K., and Solanki, S. K. (2016). High-resolution, high-sensitivity, ground-based solar spectropolarimetry with a new fast imaging polarimeter - I. Prototype characterization. *Astronomy & Astrophysics*, 590:A89. Publisher: EDP Sciences.

Kliger, D. S., Lewis, J. W., and Randall, C. E. (1990). CHAPTER 4 - Introduction to the Jones Calculus, Mueller Calculus, and Poincaré Sphere. In Kliger, D. S., Lewis, J. W., and Randall, C. E., editors, *Polarized Light in Optics and Spectroscopy*, pages 59–101. Academic Press, Boston.

Krijger, J., Tanzi, C., Aben, I., and Paul, F. (2005). Validation of GOME polarization measurements by method of limiting atmospheres. *Journal of Geophysical Research: Atmospheres*, 110(D7).

Lindqvist, H., Martikainen, J., Räbinä, J., Penttilä, A., and Muinonen, K. (2018). Ray optics for absorbing particles with application to ice crystals at near-infrared wavelengths. *Journal of Quantitative Spectroscopy and Radiative Transfer*, 217:329–337.

Munro, R., Eisinger, M., Anderson, C., Callies, J., Corpaccioli, E., Lang, R., Lefebvre, A., Livschitz, Y., and Albinana, A. P. (2006). GOME-2 on MetOp. In *Proc. of The 2006 EUMETSAT Meteorological Satellite Conference, Helsinki, Finland*, volume 1216, page 48.

NASA (2024). Chapter 12: Science Instruments - NASA Science. https://science.nasa.gov/learn/basics-of-space-flight/chapter12-1/. Date Accessed: February 2024.

Newport (2024). Introduction to waveplates - Newport. https://www.newport.com/n/introduction-to-waveplates.

Peatross, J. and Ware, M. (2015). *Physics of light and optics, chapter 6*. Brigham Young University, Department of Physics Provo, UT 84602.

Schmidt, N. (2022). Stokes-Mueller Formalism and the Poincaré Sphere for Wave Polarization State.

Shevchenko, A., Roussey, M., Friberg, A. T., and Setälä, T. (2017). Polarization time of unpolarized light. *Optica*, 4(1):64–70.

Sparks, W., Germer, T. A., MacKenty, J. W., and Snik, F. (2012). Compact and robust method for full Stokes spectropolarimetry. *Applied Optics*, 51(22):5495–5511. Publisher: Optica Publishing Group.

Trippe, S. (2014). Polarization and Polarimetry: A Review. arXiv:1401.1911 [astro-ph].

UMBC (2020). Harp cubesat - UMBC Earth and Space Institute. https://esi.umbc.edu/hyper-angular-rainbow-polarimeter/. Date Accessed: February 2024.

Vasilescu, B. (2025). *Development of a high-performing spectropolarimeter for space usage*. PhD thesis, Delft University of Technology.

Vasilescu, B., Nazé, Y., and Loicq, J. (2020a). Development of a space spectropolarimeter for full stokes parameters retrieval. In *Advances in Optical and Mechanical Technologies for Telescopes and Instrumentation IV*, volume 11451, pages 718–724. SPIE.

Vasilescu, B., Nazé, Y., and Loicq, J. (2020b). Solution uniqueness and noise impact in a static spectropolarimeter based on birefringent prisms for full Stokes parameter retrieval. *Journal of Astronomical Telescopes, Instruments, and Systems*, 6(2):028001. Publisher: SPIE.

Vasilescu, B., Piron, P., and Loicq, J. (2023). Performance analysis of a spectropolarimeter employing a continuous phase variation. *Optics Express*, 31(13):21078–21092.

Weidlich, A. and Wilkie, A. (2008). Realistic rendering of birefringency in uniaxial crystals. *ACM Transactions on Graphics*, 27(1).

# A

# Reflection Correction Factor Formulas

When applying correction factors to the reflection Jones vectors, the same general formula is applied for each boundary as was used for the transmission cases. If boundary 2 of the modulator is considered, then the correction factors of both boudnary 1 and boundary 2 must be applied:

$$R_{B2_s} = \left(\frac{n_{2_s}\cos r_{B1_s}}{n_{1_s}\cos i_{B1_s}}\right)\left(\frac{n_{1_s}\cos r_{B2_s}}{n_{1_s}\cos i_{B2_s}}\right)r_s^2 \tag{A.1}$$

$$R_{B2_p} = \left(\frac{n_{2_p}\cos r_{B1_p}}{n_{1_p}\cos i_{B1_p}}\right)\left(\frac{n_{1_p}\cos r_{B2_p}}{n_{1_p}\cos i_{B2_p}}\right)r_p^2 \tag{A.2}$$

However, the correction factors for boundary 2 are not for a transmission case, but rather the reflection case. This means that the refractive index is not changing at this boundary, and that the angle of incidence is equal to the angle of 'refraction' which in this case is actually the angle of reflection. Thus, the correction factor for boundary 2 can be entirely simplified, resulting in a need to only include the factor for a transmission case:

$$R_{B2_s} = \left(\frac{n_{2_s}\cos r_{B1_s}}{n_{1_s}\cos i_{B1_s}}\right)r_s^2 \tag{A.3}$$

$$R_{B2_p} = \left(\frac{n_{2_p}\cos r_{B1_p}}{n_{1_p}\cos i_{B1_p}}\right)r_p^2 \tag{A.4}$$

# B

# Prism POB Files

## Prism 1

```
! Prism 1 Common Origin

! Face 1
V 1 -10 10 0
V 2 10 10 0
V 3 -10 -10 0
V 4 10 -10 0

! Face 2
V 5 -10 10 1
V 6 10 10 1
V 7 -10 -10 1.90819
V 8 10 -10 1.90819

!Vertex Connections
R 1 2 4 3 0 1
R 1 2 6 5 0 2
R 5 6 8 7 0 3
R 3 4 8 7 0 4
R 2 4 8 6 0 5
R 1 3 7 5 0 6
```

## Prism 3

```
! Prism 3 Common Origin

! Face 1
V 1 -10 10 4.53672
V 2 10 10 4.53672
V 3 -10 -10 2.90819
V 4 10 -10 2.90819

! Face 2
V 5 -10 10 5.53672
V 6 10 10 5.53672
V 7 -10 -10 5.53672
V 8 10 -10 5.53672

!Vertex Connections
R 1 2 4 3 0 1
R 1 2 6 5 0 2
R 5 6 8 7 0 3
R 3 4 8 7 0 4
R 2 4 8 6 0 5
R 1 3 7 5 0 6
```

# C

# Trace Mode Comparisons

The graphical comparisons of the preliminary simulations, in which the ray tracing modes were compared, are given in Figure C.1 to Figure C.4. The results are obtained using the ZEMAX output values and a rolling mean to reduce the noise. The rolling mean method is discussed in subsection 6.4.1.

The first plot, Figure C.1, shows the comparison between the Jones Python model and a ZEMAX simulation using waveplate mode prisms and no trace elements. In this plot, the general behaviour of the intensity is consistent with the Jones Python model, albeit the amplitude is clearly reduced when compared to the expected result. In Figure C.2 and Figure C.3, method 1 is compared to both the Python model and the 'no trace element' simulation. The first of these figures showcases a reduced level of noise reduction while the second has a rolling mean performed of a far higher degree. From these figures, it is clear that the simulation intensity pattern does not predict the same Fresnel behaviour as was modelled in the Python code. There are similarities such as the drop in intensity around the height of 10.25mm, but the simulation output is noisy and does not follow a sinusoidal pattern. Finally, in Figure C.4, the comparison with method 2 is included.

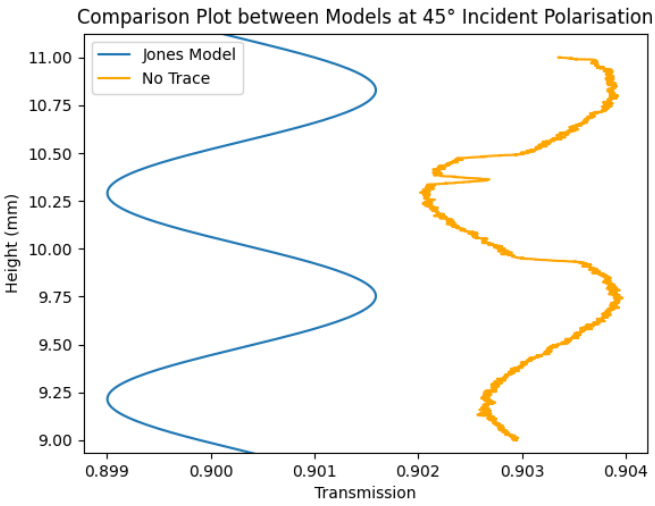


**Figure C.1:** Comparison between the Python model and the original simulation with no trace elements at the boundaries, at 45° incident linear polarisation.

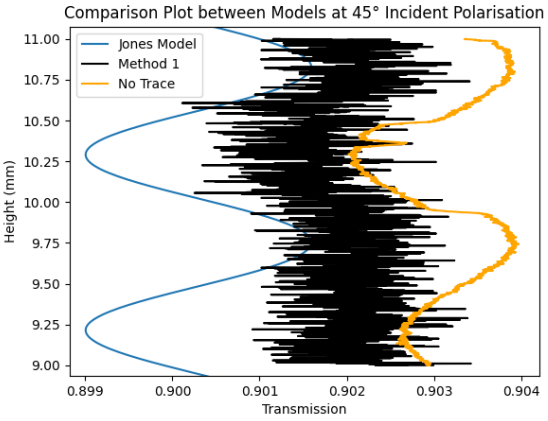


**Figure C.2:** Comparison of method 1 results to the no trace element and Python models for 45° incident polarisation. Limited reduction of the noise is performed with a rolling mean degree of approximation at 20.

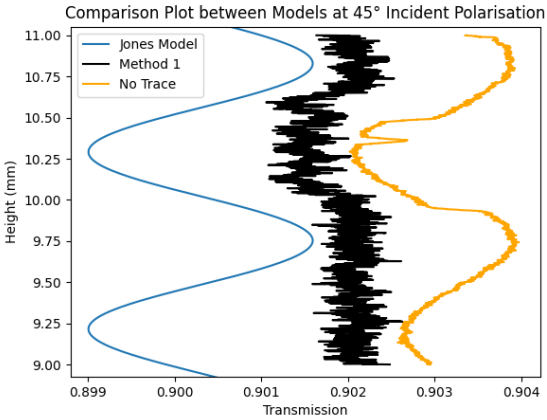


**Figure C.3:** Comparison of method 1 results to the no trace element and Python models for 45° incident polarisation. Rolling mean noise reduction is set to a factor of 50.

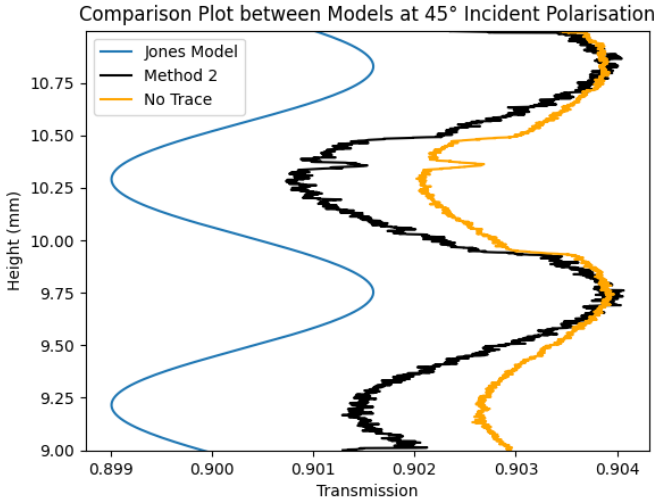


**Figure C.4:** Comparison of Method 2 results to the no trace element and Python models for 45° incident polarisation.

In the plots for the no trace element method and method 2, there is a noticeable difference in the depth of the two valleys. The likely cause of the effect is 'ghosting' and the meaning of the difference is further explained in subsection 6.3.3. It does not affect the decision between the two simulation methods as both have the same behaviour present.

In the end, the first method clearly resulted in a pattern which is inconsistent with any previous models or experimental results. The results are extremely noisy despite a significantly higher degree of approximation using the rolling mean than the double waveplate method requires. Based on the difficulty of analysing the pattern in the results, this method was abandoned for the later simulations.

Between the second method and the original waveplate mode simulation, on the other hand, the results are far less clear as to which should be selected. The second method gave the same form of results as the original waveplate mode simulation, but varied in the average transmission and the amplitude of the fluctuations. When compared to the Jones Python model, the amplitude actually becomes slightly larger than the models own predictions. Compared to the original simulation, this makes the second method appear closer to what Python suggests should be occurring. However, the exact influence of the trace element on the rays and their respective polarisation states is still uncertain as the two modes are not intended for being used together in this way.

# D

# Circular Polarisation Experimental Method

For the incident circular polarisation experimental measurements, the quarter waveplate could not be calibrated independently due to concerns with removing and then re-adding the modulator prisms. As such, an alternative method was conceived which could provide at least a representation of the circular polarisation results.

Initially, measurements for 3 different cases were taken. The first measurements were for the case in which the linear polariser and the quarter waveplate were both oriented along the horizontal axis of the setup. As the linear polariser was calibrated, the linear polariser was set to this angle easily. For the quarter waveplate, the mount was designed to more closely follow the true orientation of the waveplate fast axis itself. With the assumption that this was indeed the case, the mount was set to its horizontal position. To account for slight manufacturing errors which may affect the alignment, measurements were taken for the quarter waveplate mount angles within 10° of this position in steps of 0.1°. The theory was that, when the quarter waveplate fast axis does align with the horizontal direction, it also aligns with the linear polariser orientation. At this point, the light passing through the linear polariser is aligned in its entirety with the fast axis of the waveplate, hence meaning that the quarter waveplate does not change the polarisation state of the light.

Given that the results for linearly polarised incident light at the same orientation are already obtained, it is possible to compare the measurements taken with the quarter waveplate. At the point when these results are as similar as possible, it would be assumed that the true horizontal fast axis orientation has been determined.

To verify that this is the case, the second set of measurements was taken with the quarter waveplate rotated by 90° compared to the previous measurements. The same situation should occur in the case where the linear polariser (still horizontal) is at exactly 90° compared to the quarter waveplate. From these data sets, the offset between the expected horizontal and the true horizontal can be compared to the offset between expected vertical and true vertical. If both offsets were the same, the true orientation of the quarter waveplate could be verified.

Finally, once the true orientation would have been determined, the data set where the quarter waveplate is at 45°, and hence creating circular polarisation, would have been used to find the final resulting fluctuations from this case.